Atomic-level insights into ion conduction and ion selectivity of TMEM16 lipid scramblases

Von der Fakultät für Mathematik, Informatik und Naturwissenschaften der RWTH Aachen University zur Erlangung des akademischen Grades eines Doktors der Naturwissenschaften genehmigte Dissertation

vorgelegt von

Andrei Kostritskii, M.Sc.

aus Perevoz, Russland

Berichter: Jun.-Prof. Dr. Jan-Philipp Machtens
Univ.-Prof. Dr. Paolo Carloni
Univ.-Prof. Dr. Jörg Fitter

Tag der mündlichen Prüfung: 15.06.2022

I hereby declare that I have created this work completely on my own and used no other sources or tools than the ones listed, and that I have marked any citations accordingly.

Hiermit versichere ich, dass ich die vorliegende Arbeit selbständig verfasst und keine anderen als die angegebenen Quellen und Hilfsmittel benutzt sowie Zitate kenntlich gemacht habe.

Andrei Kostritskii
Aachen, June 2022

Contents

List of Publications

In accordance with §5(3) of the doctoral regulations, I state that extracts of the thesis have been published in the following papers:

[A] Kostritskii A. Y. and Machtens J.-P. "Molecular mechanisms of ion conduction and ion selectivity in TMEM16 lipid scramblases" *Nature Communications* **2021** *12*, 2826

[B] Kostritskii A. Y., Alleva C., Cönnen S., and Machtens J.-P. "g_elpot: a tool for quantifying biomolecular electrostatics from molecular dynamics trajectories" *Journal of Chemical Theory and Computation* **2021** *17*(5), 3157-3167

Chapters 3 through 6 correspond to publication [A] and Chapter 7 corresponds to publication [B]. Quotations from these publications are indicated throughout the text. In accordance with §5(3) of the doctoral regulations, I state my contribution to these publications:

[A] I designed the simulations, produced and analyzed the data, and wrote the paper with contributions from all coauthors. The research was done under the supervision of Prof. Jan-Philipp Machtens.

[B] I conceived the project, developed and implemented the method, analyzed the data, and wrote the paper with contributions from all coauthors. The research was done under the supervision of Prof. Jan-Philipp Machtens.

List of Figures

List of Tables

Abstract

Lipid scramblases of the TMEM16 family are Ca^{2+}-activated membrane proteins that provide a pathway for bidirectional transport of lipids between the membrane leaflets. Many TMEM16 lipid scramblases also function as ion channels with implications in various physiological processes, including apoptosis, immune response, and cell volume regulation. Although physiological functions of ion channels heavily rely on their ion selectivity, that of TMEM16 lipid scramblases remains elusive, demonstrating a notable variation among the experimental studies. Despite recent progress in structural characterization of TMEM16 lipid scramblases, the molecular mechanisms of their ion conduction and ion selectivity remain poorly understood. Here, we used atomistic molecular dynamics (MD) simulations, as a means for bridging static structural and macroscopic functional data, to unravel atomic-level details of ion channel functionality of TMEM16 lipid scramblases. We utilized the recently developed computational electrophysiology algorithm, which mimics functionality of patch-clamp experimental setup, to study ion conduction properties of fungal nhTMEM16 and human TMEM16K in various lipid membranes. We found that in the main ion conductive state TMEM16 lipid scramblases conduct ions through a structured but yet dynamic proteolipidic pore, which is partly formed by lipid headgroups. Lining the ion permeation pathway, lipid headgroups directly interact with permeating ions and shape the energetics of the ion permeation process. Notably, due to the dipole moment associated with lipid headgroups, their effect on the ion energetics depends on polarity of the applied voltage, making the headgroups a voltage-sensitive element of the pore. Moreover, our simulations demonstrated that lipid headgroups which flank the neck region of the pore can directly affect its permeability. We also found that positioning and orientation of charged residues in the pore of a TMEM16 lipid scramblase define its basic ion selectivity, which, however, can be prominently altered by membrane lipid composition via changing the pore electrostatics. We identified the regions with changed electrostatic potential by applying a new tool g_elpot, which we developed for quantifying biomolecular electrostatics from MD trajectories. Concluding, in this work we defined the structural basis of ion conduction and selectivity in TMEM16 lipid scramblases and discovered the direct effects of membrane lipids on the ion-conduction properties of these dual function proteins.

Zusammenfassung

Ca^{2+}-aktivierte Lipidskramblasen der TMEM16-Familie sind Membranproteine, welche den bidirektionalen Transport von Lipiden zwischen den beiden Hälften der Zellmembran ermöglichen. TMEM16-Lipidskramblasen fungieren zusätzlich als Ionenkanäle und spielen wichtige Rollen in physiologischen Funktionen wie Zellvolumenregulation, Apoptose und der Immunabwehr. Obwohl die physiologische Funktion von Ionenkanälen maßgeblich von ihrer Ionenselektivität abhängt, zeigt diese im Fall von TMEM16-Lipidskramblasen in verschiedenen experimentellen Studien eine hohe Variabilität und konnte daher bislang nicht eindeutig definiert werden. Trotz vieler Fortschritte in der strukturellen Charakterisierung von TMEM16-Lipidskramblasen, sind die molekularen Mechanismen der Ionenleitung und Ionenselektivität bislang unverstanden. In dieser Arbeit verwendeten wir Molekulardynamik(MD)-Simulationen um die Ionenkanalfunktion von TMEM16-Lipidskramblasen in atomarer Auflösung aufzuklären und eine Verknüpfung zwischen den Proteinstrukturen und makroskopischen/funktionellen Daten herzustellen. Mit Hilfe des kürzlich entwickelten Computational Electrophysiology-Verfahrens zur Simulation elektrochemischer Potentialgradienten, vergleichbar mit Patch-Clamp-Experimenten, untersuchten wir die Ionenleitung durch nhTMEM16, einem Homolog aus dem Reich der Pilze, sowie die humane TMEM16K-Isoform in verschiedenen Lipidmembranen. Mit Hilfe dieser Simulationen konnten wir den hauptsächlichen ionenleitenden Zustand der TMEM16-Lipidskramblasen definieren, in welchem Ionen durch eine dynamische, von Aminosäuren und Lipidkopfgruppen begrenzte, Pore permeieren. Auf Grund dieser komplexen Porenarchitektur, können Lipidkopfgruppen direkt mit permierenden Ionen interagieren und die Energetik der Ionenpermeation regulieren. Interessanterweise hängt die Orientierung der Lipidkopfguppen in der Pore, auf Grund ihres intrinsische Dipolmomentes, von der Richtung der Transmembranspannung ab, woraus sich eine spannungsabhängige Regulation der Ionenpermeation ergibt. Des Weiteren zeigen unsere Simulationen, dass Lipide, welche die Engstelle der Pore begrenzen, auch ihre Permeabilität direkt regulieren. Während die genaue Anordnung und Ladung der Aminosäuren in der TMEM16-Pore die basale Ionenselektivität bestimmen, wird die Selektivität zusätzlich durch die Lipidzusammensetzung der Membran über elektrostatische Einflüsse auf die Pore reguliert. Die Entwicklung des Programms g_elpot zur Berechnung elektrostatischer Potential aus MD-Trajektorien, ermöglichte uns eine genaue Charakterisierung dieser, durch Membranlipide vermittelten, Potentialänderungen in der Pore. Zusammenfassend hat unsere Arbeit die strukturellen Grundlagen der Ionenleitung und Ionenselektivität von TMEM16-Lipidskramblasen und neue regulatorische Effekte der Membranlipide auf die Leitungseigenschaften dieser bifunktionellen Proteine aufgeklärt.

Ignoramus et ignorabimus.
—Emil Du Bois-Reymond

Chapter 1

Introduction

The TMEM16 protein family (also known as anoctamins) comprises Ca^{2+}-activated ion channels and lipid scramblases, which facilitate passive transport of lipids across the membrane. Many of TMEM16 lipid scramblases also operate as ion channels. Such combination of rather distinct functionalities within a single protein family is directly related to unique structural features of TMEM16 proteins. In this chapter, TMEM16 proteins are introduced with the focus on TMEM16 lipid scramblases and their ion conduction. The introduction is done through an overview of various functions of TMEM16 proteins, followed by a description of their molecular structures and discussion of the ion-conduction models that have been proposed so far. At the end of the chapter, the main aims of this work are outlined.

1.1 Functions of TMEM16 proteins

In mammals, the TMEM16 family consists of ten members, labeled with letters from A to K, excluding I. The founding members of the TMEM16 family (TMEM16A and TMEM16B) were first discovered in 2008 as long-sought molecular identities of Ca^{2+}-activated chloride channels [1–3]. TMEM16A and TMEM16B are mainly expressed in epithelial and neuronal tissues, respectively [4]. These channels are engaged in a plethora of physiological functions. In particular, TMEM16A regulates epithelium Cl^- secretion [1], modulates nociception [5, 6], and blocks polyspermia in frog egg membranes [2]. In turn, TMEM16B modulates signal transduction in hippocampus [7] and in olfactory receptor neurons [8]. The channels are activated directly by Ca^{2+} but demonstrate slightly different Ca^{2+} sensitivity, so that EC50 ranges from hundreds of nM in TMEM16A [9] to a few μM in TMEM16B [10]. The channel activation also demonstrates voltage dependence so that membrane depolarization and Ca^{2+} binding synergistically promote opening of the ion conducting pore [11].

Other members of the family had been assumed to be Ca^{2+}-activated anion channels as well, until in 2010 TMEM16F was discovered to facilitate lipid scrambling, that

is the bidirectional transport of lipids between leaflets of the lipid membrane [12]. The main physiological implications of the TMEM16F-mediated scrambling include blood coagulation [12–14], bone mineralization [15], immune response [16], and placenta development [17]. These functions rely on externalization of negatively charged phosphatidylserine (PS) lipids [18], which are normally sequestered to the internal membrane leaflet [19]. Experimental evidence suggests that most of the members of the TMEM16 family can operate as lipid scramblases [20]. Whereas physiological functions of majority of TMEM16 lipid scramblases remain largely elusive, their ubiquitous expression suggests that they may play important roles in cellular physiology [4]. In particular, TMEM16K lipid scramblase, which is localized to the endoplasmic reticulum (ER) membrane [21], was recently shown to regulate endosomal sorting [22]. Finally, fungal homologs of the family were shown to scramble lipids when reconstituted into liposomes [23, 24], unambiguously demonstrating innate scrambling functionality of the TMEM16 family.

Intriguingly, many of TMEM16 lipid scramblases have also been shown to operate as ion channels [25]. These include TMEM16F [13, 26–28], TMEM16K [29], and fungal afTMEM16 from *Aspergillus fumigatus* [23] and nhTMEM16 from *Nectria haematococca* [30]. Various physiological functions of ion currents mediated by scramblases include apoptotic cell shrinkage [26, 31], innate immunity [27, 32], modulation of Ca^{2+} signaling [13, 33], and cell volume regulation [29]. Compared to TMEM16A and TMEM16B, TMEM16 lipid scramblases require higher concentration of Ca^{2+} for their activation, with EC50 for TMEM16F being in a hundred-μM range [34]. Whereas anion selectivity of bona fide channels TMEM16A and TMEM16B is well established, lipid scramblases demonstrate a notable variation in ion selectivity between different studies [25, 35]. In particular, the TMEM16F lipid scramblase has been variously reported to generate nonselective [36, 37], anion selective [26, 34, 38], and cation selective [13, 39, 40] currents. Moreover, ion selectivity of TMEM16F has recently been shown to depend on salt concentration [41, 42]. In addition, a lipid scramblase obtained by a single mutation in TMEM16A demonstrated cation selectivity in contrast to the clear Cl^- selectivity of the wild type channel [43]. Although ion selectivity of the ER-localized lipid scramblase TMEM16K is hard to measure in the cellular experiments due to its intracellular localization, this scramblase was shown to be permeable to both cations and anions, when reconstituted into liposomes [21]. The absence of strong ion selectivity was also shown for the fungal scramblases [23, 30]. Thus, despite high physiological importance, ion selectivity of TMEM16 lipid scramblases remains highly controversial, with its molecular determinants being poorly understood.

1.2 Structures of TMEM16 proteins

The first structural insight into the TMEM16 protein family was obtained from the X-ray structure of nhTMEM16 [24]. In agreement with previous FRET [44] and blue-native gel electrophoresis experiments [45], the scramblase revealed a dimeric structure with a butterfly-like scaffold (Figure 1.1). Interestingly, the TMEM16 proteins are

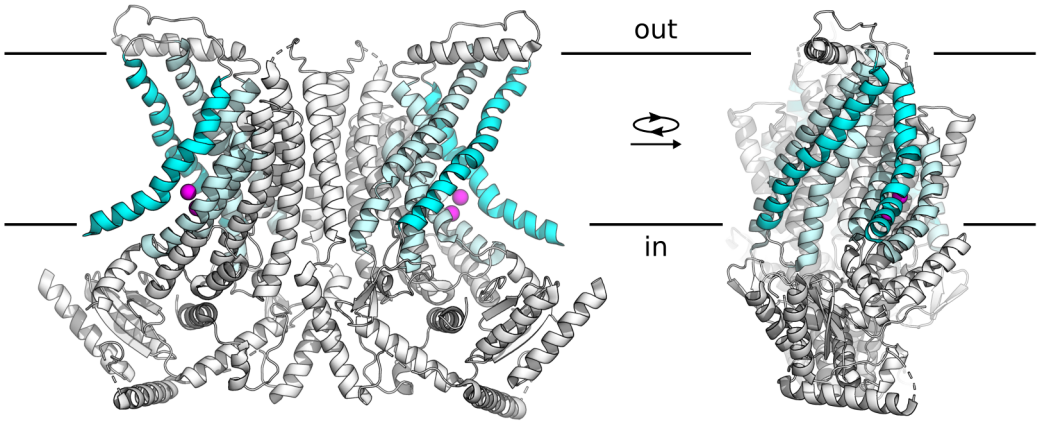

Figure 1.1: Structure of nhTMEM16 in the Ca^{2+}-bound fully open conformation (PDB ID: 4WIS) resolved by the X-ray crystallography. Protomers are colored in gray and white, Ca^{2+} ions are shown as magenta spheres. Transmembrane helices that line and border the subunit cavity are shown in pale and bright cyan, respectively. Membrane borders are schematically depicted.

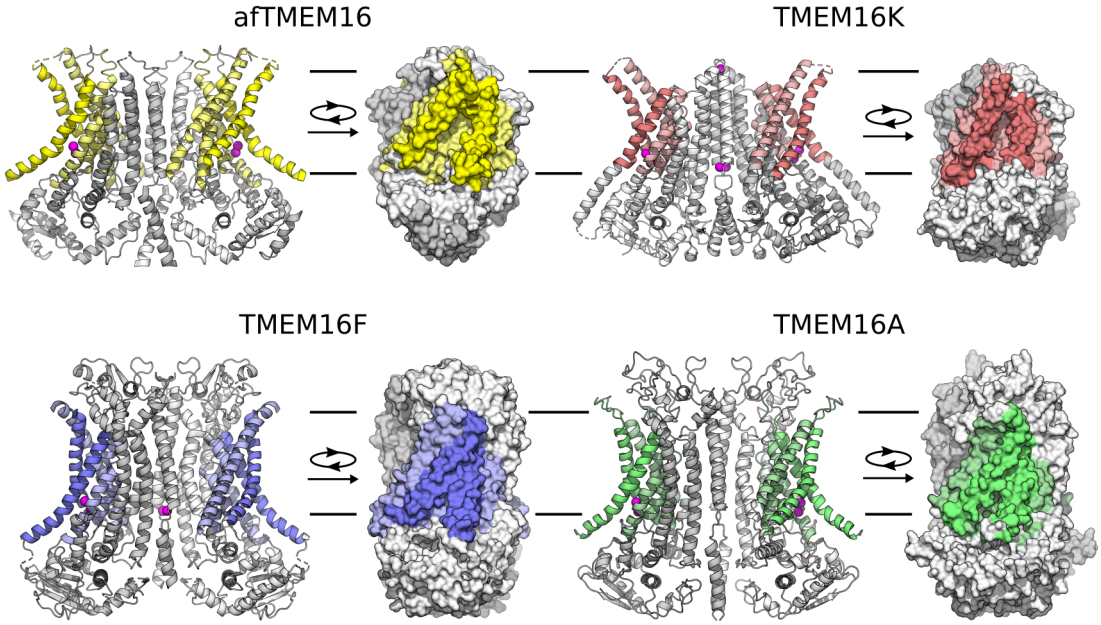

Figure 1.2: **a**, **b** Cryo-EM structure of afTMEM16 (**a**; PDB ID: 6E0H) and X-ray structure of TMEM16K (**b**; PDB ID: 5OC9) in the Ca^{2+}-bound fully open conformations. **c**, **d** Cryo-EM structures of TMEM16F (**c**; PDB ID: 6QP6) and TMEM16A (**d**; PDB ID: 5OYB) in the Ca^{2+}-bound closed conformations. **a**–**d** Protomers are colored in gray and white, with pore-lining and cavity-bordering helices highlighted by pale and bright colors, respectively. Membrane borders are schematically depicted.

also known as anoctamins, reflecting the eight-transmembrane-domain topology suggested by initial hydropathy analysis [3]. However, the nhTMEM16 structure showed that each protomer comprises ten transmembrane (TM) helices, consistent with the revised topology that was inferred from the biochemical assays [46]. The structure also revealed molecular basis for the Ca^{2+} activation: each protomer has an individual Ca^{2+}-binding site, which can be occupied by two Ca^{2+} ions (Figure 1.1). Notably, the Ca^{2+}-binding site is located within the transmembrane region of the protein, explaining a polarization-induced enhancement of Ca^{2+} sensitivity observed in TMEM16 Cl^- channels [11, 47]. The most prominent topological feature of nhTMEM16 uncovered by the structure is a so-called subunit cavity, that is a membrane-spanning groove which is open to the hydrophobic interior of the membrane (Figure 1.1). The subunit cavity is partly lined by hydrophilic residues, thereby providing an energetically favorable pathway for polar lipid headgroups across the membrane. As shown later in a number of MD studies [21, 43, 48–51], lipids retain their hydrophobic tails in a membrane core upon sliding along the subunit cavity with their polar headgroups, consistent with the proposed "credit card" mechanism of lipid scrambling [52].

The structural characterization of fungal nhTMEM16 was followed by a number of cryo-EM studies on other TMEM16 proteins [21, 40, 53–57]. The resolved structures demonstrated similar organization of protomers into dimers (Figure 1.2), which is likely general for the whole family. Interestingly, an additional Ca^{2+}-binding site was found at TM10 in mammalian scramblases TMEM16F [40] and TMEM16K [21]. Although it was first overseen in the TMEM16A structure, this site was later detected by reanalyzing the unassigned density in the original cryo-EM data [40] and was recently shown to affect Ca^{2+} sensitivity of TMEM16A [58]. Notably, the structures of TMEM16 ion channels and lipid scramblases revealed a variation in conformation of the subunit cavity. Similar to nhTMEM16, the cavity was fully open in Ca^{2+}-bound afTMEM16 [57] and TMEM16K [21]. In contrast, the extracellular part of the cavity was sealed from the membrane in the Ca^{2+}-bound TMEM16F [57] and TMEM16A [53, 54] structures (Figure 1.2). Such sealed cavity is structurally similar to the closed conformation observed in absence of Ca^{2+} and, therefore, likely represents an inactive state of TMEM16A and TMEM16F. Inability of the cryo-EM experiments to resolve open conformations of these isoforms might have resulted from a lack of phosphatidylinositol bisphosphate (PIP2) lipids in the sample preparations, since PIP2 was shown to be crucial for the full activation of TMEM16F [39] and TMEM16A [59].

1.3 Conduction models of TMEM16 lipid scramblases

Recent cryo-EM studies demonstrated that nhTMEM16 cavity adopts different conformations when reconstituted in lipid nanodiscs [56]. In particular, the protein was found to be at equilibrium between fully open, intermediate, and closed conformations in the Ca^{2+}-bound state. Similar to the structure of TMEM16F, the subunit cavity of nhTMEM16 in the intermediate conformation is semi-sealed in its extracellular part (Figure 1.3a). However, because of the slightly wider opening of the subunit cavity it was suggested to be permeable to ions. The L302A mutation was found to

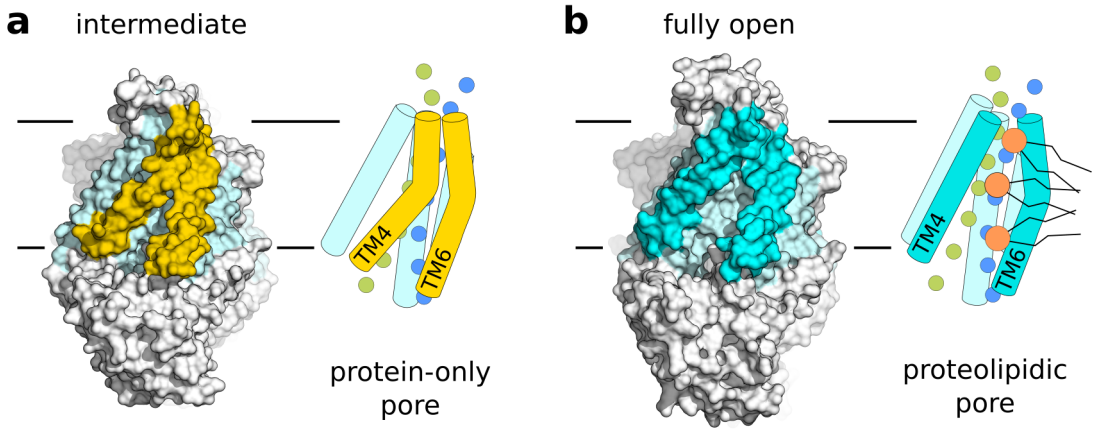

Figure 1.3: a, **b** nhTMEM16 in the intermediate (**a**) and fully open (**b**) conformations together with the proposed models of ion conduction. Transmembrane helices 4 and 6 are highlighted. Lipid headgroups, Cl^- ions, and Na^+ ions are shown as orange, green, and blue spheres, respectively. Membrane borders are schematically depicted.

stabilize nhTMEM16 in the intermediate conformation [49]. Notably, the L302A mutant was permeable to ions, while its scrambling functionality was strongly attenuated in the liposome experiments [49]. As a result, the ion conduction was proposed to take place via the "alternating pore-cavity" model [40], which suggests separation of ion-conduction and scrambling functionalities, so that the intermediate conformation represents the ion conductive state (Figure 1.3a), whereas the fully open conformation corresponds to the lipid-scrambling state. Indirectly, this model is supported by recent functional studies, which demonstrated that some mutations strongly attenuate lipid scrambling but have a much milder effect on ion conduction of nhTMEM16 [49, 56]. In contrast, the proteolipidic-pore model assumes that both ions and lipids are transported via a single protein conformation, in which ions permeate through the open subunit cavity lined by lipid headgroups [18], as illustrated in Figure 1.3b. This model was corroborated by molecular dynamics (MD) simulations, where ion permeation was observed through nhTMEM16 under applied voltage [43]. Summarizing, despite certain progress, results from structural, functional, and computational studies have not yet reached a consensus on the mechanism of ion conduction in TMEM16 lipid scramblases.

1.4 Aims and outline of the thesis

Due to the lack of a detailed mechanistic model for ion conduction, some of the functional properties of TMEM16 lipid scramblases remain controversial and poorly understood. Resolving the molecular mechanism of ion conduction mediated by TMEM16 lipid scramblases would be an essential milestone on the way to the full understanding of their roles in cellular physiology. The main goal of this work was to gain a dynamic atomic-level picture of the ion conduction mechanism of TMEM16 lipid scramblases by means of extensive MD simulations of fungal nhTMEM16 and

human TMEM16K, to fill the gap between static structural and macroscopic functional studies. In particular, the present thesis sheds light on the following aspects of ion conduction in TMEM16 lipid scramblases:

- the main ion conductive state (Chapter 3)
- detailed structure of the proteolipidic pore (Chapter 4)
- molecular details of ion-permeation process (Chapter 5)
- diverse roles of lipids in ion conduction (Chapters 5 and 6)
- molecular determinants of ion selectivity (Chapters 6 and 7)
- electrostatics within the pore (Chapter 7).

The thesis ends with the main conclusions and perspectives of the study.

. . . credibile est, quia ineptum est.
—Tertullian

Chapter 2

Theory and methods

In this study, ion conduction mechanism of TMEM16 lipid scramblases was investigated by means of MD simulations. In particular, the Computational Electrophysiology (CompEL) method was used to apply voltage and induce ion permeation through the pores formed by TMEM16 lipid scramblases. In this chapter, the foundations of the methods are provided together with the simulation and analysis details. Since MD simulations generally rely on a broad range of computational algorithms, here, for the sake of conciseness, we describe the main ideas behind classical MD simulations, putting particular focus only on the algorithms that were utilized in this study.

2.1 Molecular dynamics

Basic principles

MD is a method encompassing various numerical techniques, which allows for computational investigation of atomic and molecular systems. Originally developed for physical investigation of atomic systems, the method soon found its application in molecular biophysics [60–62] and finally became an indispensable tool for studying biomolecular structure and dynamics at atomic resolution [63]. The cornerstone of the method is Newton's equation

$$m_i \ddot{r}_i = -\frac{\partial U}{\partial r_i}, \tag{2.1}$$

where m_i and r_i are the mass and the position of atom i, and U is a potential energy function. Thus, the atoms are described as point particles obeying the laws of classical mechanics. Assuming that positions (r) and velocities (v) of atoms are known at time t, the equation of motion is numerically integrated to obtain $r(t + \Delta t)$ and $v(t + \Delta t)$, so that the direct output of MD simulations is a trajectory of the system in the phase space, that is a time series of atomic positions and velocities. The resulting trajectory can be then analyzed to derive structural and dynamic properties of the system.

Numerical integration

In MD simulations, equations of motion are integrated numerically. To correspond to Hamiltonian dynamics as close as possible, the integration schemes have to be time-reversible and area-preserving. The latter means that application of the integrator does not change the (hyper) volume of phase space corresponding to a particular energy of the system. An important advantage of such algorithms is that they generate a trajectory with minor, if any, long-term energy drift [64]. Among such schemes the Verlet algorithm and its derivatives are the most commonly used. In this study, we used the leap-frog algorithm, a variation of the Verlet scheme, in which the new particle positions r at the time step $t + \Delta t$ are obtained by using the velocities v calculated at half-integer time step $t + \frac{1}{2}\Delta t$ as

$$r(t + \Delta t) = r(t) + \Delta t v(t + \frac{1}{2}\Delta t). \tag{2.2}$$

In turn, the velocity is calculated from the force f acting on the particles at time t and the velocity at the previous half-step

$$v(t + \frac{1}{2}\Delta t) = v(t - \frac{1}{2}\Delta t) + \Delta t \frac{f(t)}{m}. \tag{2.3}$$

Notably, the velocities and positions are not evaluated at the same time, and, therefore, the total energy as a sum of kinetic and potential terms cannot be directly computed at each time step. Although this limitation could be disadvantageous for simulations in the microcanonical NVE ensemble, it is less relevant for the ensembles which are closer related to experimental conditions.

Thermostat

In particular, not the total energy but temperature is kept constant in most biological experiments. Therefore, the first step to a more realistic system description would be simulations in the canonical NVT ensemble. The average temperature $\overline{T}$ is related to the average kinetic energy $\overline{K}$ as

$$\overline{K} = \frac{1}{2} N_f k_B \overline{T}, \tag{2.4}$$

where N_f is the number of degrees of freedom and k_B is the Boltzmann constant. Analogously, in MD simulations, one defines instantaneous temperature T as

$$T = \frac{2K}{N_f k_B}, \tag{2.5}$$

where K is the kinetic energy defined as

$$K = \sum_{i=1}^{N} \frac{1}{2} m_i v_i^2, \tag{2.6}$$

where N is the total number of particles, m_i and v_i are the mass and the velocity of the i-th particle. Therefore, bringing temperature to its target average value is equivalent to bringing the kinetic energy to $\overline{K}$.

This can be achieved by a number of algorithms, which are called thermostats according to their function. In particular, a system can be weakly bound to an external thermal bath with the first order kinetics, so that the kinetic energy is changed according to

$$\frac{dK}{dt} = \frac{\overline{K} - K}{\tau}, \tag{2.7}$$

where τ is a time constant of the kinetic-energy decay. This scheme is used in the Berendsen thermostat [65], which exponentially dampens deviations from the target kinetic energy. In practice, velocities at $t + \frac{1}{2}\Delta t$ are scaled by a factor λ, which is given by

$$\lambda = \left[1 + \frac{\Delta t}{\tau}\left(\frac{\overline{K}}{K(t - \frac{1}{2}\Delta t)} - 1\right)\right]^{\frac{1}{2}}, \tag{2.8}$$

to bring K closer to $\overline{K}$. Although the algorithm generates the proper average value of the kinetic energy, it does not correspond to any standard thermodynamic ensemble.

Recently, the idea of velocity rescaling was further developed, to overcome the limitations of the Berendsen scheme and to generate fluctuations that would correspond to the canonical ensemble [66]. In the suggested scheme, a stochastic term is added to the Berendsen thermostat so that the dynamics of the kinetic energy is described by

$$\frac{dK}{dt} = \frac{\overline{K} - K}{\tau} + 2\sqrt{\frac{\overline{K}}{N_f}}\frac{dW}{\sqrt{t}}, \tag{2.9}$$

where dW is a Wiener noise. In turn, the velocity-rescaling factor λ is obtained according to

$$\lambda^2 = e^{-\Delta t/\tau} + \frac{\overline{K}}{N_f K}(1 - e^{-\Delta t/\tau})(R_1^2 + \sum_{i=2}^{N_f} R_i^2) + 2e^{-\Delta t/\tau}\sqrt{\frac{\overline{K}}{N_f K}(1 - e^{-\Delta t/\tau})}R_1^2, \tag{2.10}$$

where the R_i's are independent random numbers from a Gaussian distribution with unitary variance [66]. The resulting thermostat quickly equilibrates systems, which are far from the equilibrium, and samples the canonical distribution once the equilibrium has been reached. Due to its general applicability, we applied this thermostat to both equilibration and production phases of the simulations with τ of 0.5 ps. To ensure proper heating of every component of our heterogeneous systems, here we applied the thermostat separately to lipid membranes, proteins and water-ion solutions.

Barostat

Since pressure rather than volume is controlled in the majority of biological experiments, simulations have to be conducted in the isotherm-isobaric NPT ensemble to

better match the experimental conditions[1]. The pressure tensor $\mathbf{P}$ in an atomic system is defined as

$$\mathbf{P} = \frac{2}{V}(K + \frac{1}{2}\sum_{i<j}\mathbf{r}_{ij} \otimes \mathbf{F}_{ij}), \tag{2.11}$$

where V is the volume of the simulation box. A number of algorithms exists to ensure a certain value of pressure in a simulated system, i.e. for pressure coupling. Similar to the Berendsen thermostat, the Berendsen barostat relaxes the pressure $\mathbf{P}$ to the target value $\overline{\mathbf{P}}$ with the time constant τ_P through

$$\frac{d\mathbf{P}}{dt} = \frac{\overline{\mathbf{P}} - \mathbf{P}}{\tau_P}. \tag{2.12}$$

In fact, pressure coupling is established by scaling coordinates and box vectors by the scaling matrix μ, which is given by

$$\mu_{ij} = \delta_{ij} - \frac{\Delta t}{3\tau_P}\beta_{ij}(\overline{P}_{ij} - P_{ij}), \tag{2.13}$$

where β defines the isothermal compressibility of the system, which was set to 4.5 $\times 10^{-5}$ bar^{-1} in our simulations. The Berendsen barostat shares both the advantages and disadvantages of the Berendsen thermostat: It efficiently equilibrates the system but does not produce fluctuations in pressure, which would correspond to the NPT ensemble.

The Parrinello-Rahman barostat [67, 68] can be used as an alternative to the weak coupling scheme of Berendsen if fluctuations in pressure and volume are important. In brief, an extended Lagrangian is built with box vectors as additional dynamic variables, and the dynamics of the box matrix $\mathbf{h}$ is described by

$$\ddot{\mathbf{h}} = V\mathbf{W}^{-1}\mathbf{h}^{-1}(\mathbf{P} - \overline{\mathbf{P}}), \tag{2.14}$$

where $\mathbf{W}^{-1}$ is the inverse mass parameter matrix that determines the strength of the coupling. The parameter matrix is defined as

$$\left(\mathbf{W}^{-1}\right)_{ij} = \frac{4\pi^2\beta_{ij}}{3\tau_P^2 L}, \tag{2.15}$$

where L is the largest matrix element of the box.

In this study, the Berendsen barostat was used for equilibration of the systems. For the production runs either the Berendsen or Parrinello-Rahman barostat was used with τ_P of 5 ps. Because of the presence of membranes in our simulations, the pressure was applied semi-isotropically, meaning separate coupling for xy and z dimensions.

[1]Note, however, that due to the low compressibility of biological systems, simulations in the *NVT* ensemble can provide relevant information as well.

Force field

In MD simulations, a term force field is used to describe a potential-energy function, which defines interatomic interactions. Thus the force filed is defined both by the functional form of the potential energy and by the set of the parameters in this potential-energy function. In practice, a particular choice of a force filed depends on the area of application and on the availability of parameters for molecules to be simulated. In this study, the CHARMM force filed was used, due to its ability to properly describe structural and dynamic properties of both proteins [69] and lipids [70]. Therefore, here we discuss the details of the force filed organization for a particular case of the CHARMM force field.

In general, the potential energy function can be divided into two terms, which describe bonded and nonbonded interactions

$$U = U_{bonded} + U_{nonbonded}. \tag{2.16}$$

In turn, the bonded potential can be split into potential energy of interatomic bonds U_{bonds}, valence angles U_{angles}, improper dihedrals $U_{imp.}$, and dihedrals $U_{dih.}$

$$\begin{aligned} U_{bonded} &= U_{bonds} + U_{angles} + U_{imp.} + U_{dih.} \\ &= \sum_{bonds} K_b(b - b_0)^2 \\ &+ \sum_{angles} K_\theta(\theta - \theta_0)^2 \\ &+ \sum_{\substack{improper \\ dihedrals}} K_\phi(\phi - \phi_0)^2 \\ &+ \sum_{dihedrals} \sum_{n} K_{\psi,n}(1 + cos(n\psi - \delta_n)), \end{aligned} \tag{2.17}$$

where b_0, θ_0, and ϕ_0 are equilibrium values of bond lengths b, valence angles θ, and improper dihedral angles ϕ with force constants of K_b, K_θ, and K_ϕ, respectively, and $K_{\psi,n}$ and δ_n are the force constant and the phase for each multiplicity n of the dihedral term. In this form the bonded potential is used in many popular biomolecular force fields such as AMBER [71] and OPLS-AA [72]. In the CHARMM force filed, the bonded potential also includes the Urey-Bradley term, that is a harmonic potential applied to the distance $d_{1,3}$ between end atoms forming a valence angle

$$U_{UB} = \sum_{angles} K_{UB}(d_{1,3} - d_{1,3;0})^2, \tag{2.18}$$

where K_{UB} is the force constant, $d_{1,3}$ is the distance between the first and the third atom forming the angle, and $d_{1,3;0}$ is the equilibrium value of this distance. Finally, the potential energy in the CHARMM force filed contains the protein-specific CMAP term, which is applied to the backbone dihedrals for a better fit of the potential energy surface to the one obtained with quantum mechanical (QM) methods [73]. Parameters for the bonded interactions are derived from QM calculations and experimental data [74].

Stability of the simulation strongly depends on the integration time step, which should be small enough to guarantee proper sampling of the fastest motions in the system. In a classical molecular system, the fastest motion corresponds to bond vibrations. Since macromolecular dynamics is dominated by rotations around the bonds and not by the bond lengths, the latter are often constrained in simulations by algorithms such as SHAKE [75] or LINKS [76]. The latter was used in this study to constrain all the hydrogen-involving bonds, allowing us to use an integration time step of 2 fs.

The nonbonded part of the potential is given by

$$U_{nonbonded} = U_{LJ} + U_{qq} = \sum_{i<j} 4\epsilon_{ij} \left[\left(\frac{\sigma_{ij}}{r_{ij}} \right)^{12} - \left(\frac{\sigma_{ij}}{r_{ij}} \right)^{6} \right] + \sum_{i<j} \frac{q_i q_j}{4\pi\epsilon_0 r_{ij}}, \qquad (2.19)$$

where the sums are over all the nonbonded atom pairs. The first term describes the van der Waals (vdW) interactions and Pauli repulsion in form of the Lennard-Jones (LJ) potential. The well depth of the LJ potential is defined by ϵ_{ij}, and σ_{ij} defines the interatomic distance at which the potential is zero. The second term describes the Coulomb interactions between atoms with partial charges q in vacuum with the permittivity of ϵ_0. In the CHARMM force filed, the parameters for the LJ potential are based on reproducing such experimental properties as density and heat of vaporization of molecular liquids [74]. The atomic charges, in turn, are optimized to reproduce QM interaction energies as well as equilibrium distances between a parameterized compound and a water molecule, which is placed at different sites around the moiety to be parameterized. Notably, in contrast to some other force fields, no scaling factor is applied to the electrostatic interactions between 1-4 atoms forming the dihedrals in the CHARMM force filed. Finally, for the sake of compatibility with the other parameters, water molecules were described by a special TIP3P model, where hydrogen atoms participate in the vdW interactions.

Periodic boundary conditions and nonbonded interactions

Due to high computational costs, a typical simulation box in atomistic MD simulations rarely exceeds tens of nanometers. To approximate the bulk-phase behavior of the system and to avoid artifacts at its boundaries, periodic boundary conditions are usually applied. As a result, the simulation box is virtually surrounded by its periodic copies. Importantly, atoms in the simulation box can interact with those from the copies. To reduce computational costs and to make simulations plausible, the LJ potential is usually cut off at a certain distance, so that the discarded part of the potential does not exceed a predefined tolerance value. In our simulations, the potential was switched to zero between 1 nm and 1.2 nm in a way ensuring smooth transition of the force at the cut-off distance. No dispersion correction was applied.

Whereas the cutting off of the LJ potential is justified by its fast decay, the Coulomb potential is long-ranged and requires special treatment in periodic systems. The total electrostatic energy of a periodic system with unit cell vectors $\mathbf{a}_1$, $\mathbf{a}_2$, $\mathbf{a}_3$ reads

$$U_{qq} = \frac{1}{2}{\sum_{\mathbf{n}}}' \sum_i \sum_i \frac{q_i q_j}{4\pi\epsilon_0 |\mathbf{r}_i - \mathbf{r}_j + \mathbf{n}|}, \tag{2.20}$$

where the outer sum is over the vectors $\mathbf{n} = n_1\mathbf{a}_1 + n_2\mathbf{a}_2 + n_3\mathbf{a}_3$ for all integers n_1, n_2, and n_3, and the prime indicates that terms with $i = j$ and $\mathbf{n} = 0$ are omitted. Convergence of this sum depends on the order of summation [77]. To reach absolute convergence of the electrostatic energy in the periodic system, the Ewald method can be used. In brief, the electrostatic energy is split into direct (U_{qq}^{dir}), reciprocal (U_{qq}^{rec}), and correction (U_{qq}^{corr}) terms. The first two terms are convergent in the real and Fourier spaces, respectively, and the correction term corresponds to the charge self interactions. In particular,

$$U_{qq}^{dir} = \frac{1}{2}{\sum_{\mathbf{n}}}' \sum_i \sum_i \frac{q_i q_j \mathrm{erfc}(\beta|\mathbf{r}_i - \mathbf{r}_j + \mathbf{n}|)}{4\pi\epsilon_0 |\mathbf{r}_i - \mathbf{r}_j + \mathbf{n}|}, \tag{2.21}$$

where β is an inverse width of the Gaussian distributed charge, which underlies the reciprocal part of the energy, and $\mathrm{erfc}(x) = 1 - \mathrm{erf}(x)$ is the complementary error function. The reciprocal part of the potential reads

$$U_{qq}^{rec} = \frac{1}{2V\epsilon_0} \sum_{\mathbf{k}\neq 0} \frac{\exp\left(-\frac{\mathbf{k}^2}{4\beta^2}\right)}{\mathbf{k}^2} S(\mathbf{k})S(-\mathbf{k}), \tag{2.22}$$

where the reciprocal lattice vectors $\mathbf{k}$ are defined by $\mathbf{k} = 2\pi(k_1\mathbf{a}_1^* + k_2\mathbf{a}_2^* + k_3\mathbf{a}_3^*)$, such that $\mathbf{a}_j^*$ are defined by $\mathbf{a}_j^*\mathbf{a}_i = \delta_{ij}$ and k_i are nonnegative integers. In turn, the structure factor $S(\mathbf{k})$ is defined by

$$S(\mathbf{k}) = \sum_{i=1}^{N} q_i \exp(-i\mathbf{k}\mathbf{r}_i). \tag{2.23}$$

Finally,

$$U_{qq}^{corr} = -\frac{\beta}{\sqrt{\pi}} \sum_{i=1}^{N} q_i^2. \tag{2.24}$$

Although the Ewald method provides the convergent result, it requires $\mathcal{O}(N^2)$ operations to calculate U_{qq}^{rec}. More efficient computation can be done by using particle-mesh Ewald methods, which utilize fast Fourier transform on the grid-distributed charge Q to calculate approximate structure factor $\tilde{S}(\mathbf{k}) = F(Q)(k_1, k_2, k_3)$. In this study we used the smooth particle-mesh Ewald (SPME) method [77], so that atomic charges were distributed over the grid using Cardinal B-splines of $n = 4$ order. The grid spacing was initially set to 1.2 Å, but fluctuated during the simulations because of the dynamic adjustment performed by the MD engine. The direct part of the potential was cut off at 1.2 nm.

Limitations

As any other research technique, MD simulations have their limitations. First, any simulation is as good as the model it is based on. While dynamics of an atomic system

is fundamentally described by the Schrödinger equation, classical MD simulations are based on Newton's laws instead. However, the extensive use of MD simulations for a few decades proved that classical dynamics can properly describe time evolution and statistical properties of atomic systems in case of properly adjusted parameters for the interatomic interactions in a force field. In turn, the classical force fields used for MD simulations are themselves based on a rather strong assumption that the interatomic forces are additive. This means that atomic polarization is discarded from the system description. Although the polarization can be effectively taken into account by polarizable force fields [78], their usage requires larger amount of computational resources compared to the simulations based on classic atomistic force fields. As a result, time scales of the simulations based on polarizable force fields are inevitably shorter, precluding direct investigation of many biological phenomena. Finally, in classical MD simulations, all the bonds in the simulation system are fixed, so that no chemical transformations can be taken into account, including any change in the protonation state of amino acids.

The second major limitation is specific to MD simulations of complex biomolecular systems, which include folded proteins. Such simulations require an initial structural model of a protein. Most of the time these models come from X-ray and cryo-EM studies, where they are built based on electron-density and Coulomb-potential maps, respectively [79]. Thus, the resolution of the original maps limit completeness and precision of the models. Due to high computational demands even state-of-the-art atomistic MD simulations of biomolecular systems are conducted on a microsecond time scale, significantly limiting the volume of the phase space sampled in the simulation. In practice, this means that the effectively sampled volume is biased by the point in the phase space that the system occupies at the start of the simulation. As a result, the quality of the initial protein model strongly affects the results of the MD simulations. To guarantee robustness of our conclusions, here we only used protein structures of high resolution (3.2–3.7 Å; Table 2.1) and conducted independent multi-replica simulations, which allowed for proper statistical analysis of the results.

2.2 Computational electrophysiology

"The CompEL method [80] was used to apply voltage to the proteins. Briefly, a CompEL system contains two lipid bilayers separating two compartments as a result of periodic boundary conditions (Figure 2.1). The transmembrane voltage across the membrane can thus be controlled by setting a charge imbalance (dQ in Tables A.1–A.8) between the compartments. Due to the low capacity of the membrane, relatively few ions ($<$ 10 % of the total number) are needed to establish transmembrane voltages of several hundred mV, so there is only a minor difference in the ion concentration between the compartments. Insertion of one copy of a protein into each bilayer thus enabled us to investigate the effects of both positive and negative voltages in a single CompEL system. In practice, each CompEL system was created by stacking two copies of a single bilayer system taken after a certain simulation time (starting time in Tables A.1–A.8). To maintain a constant average transmembrane voltage, the al-

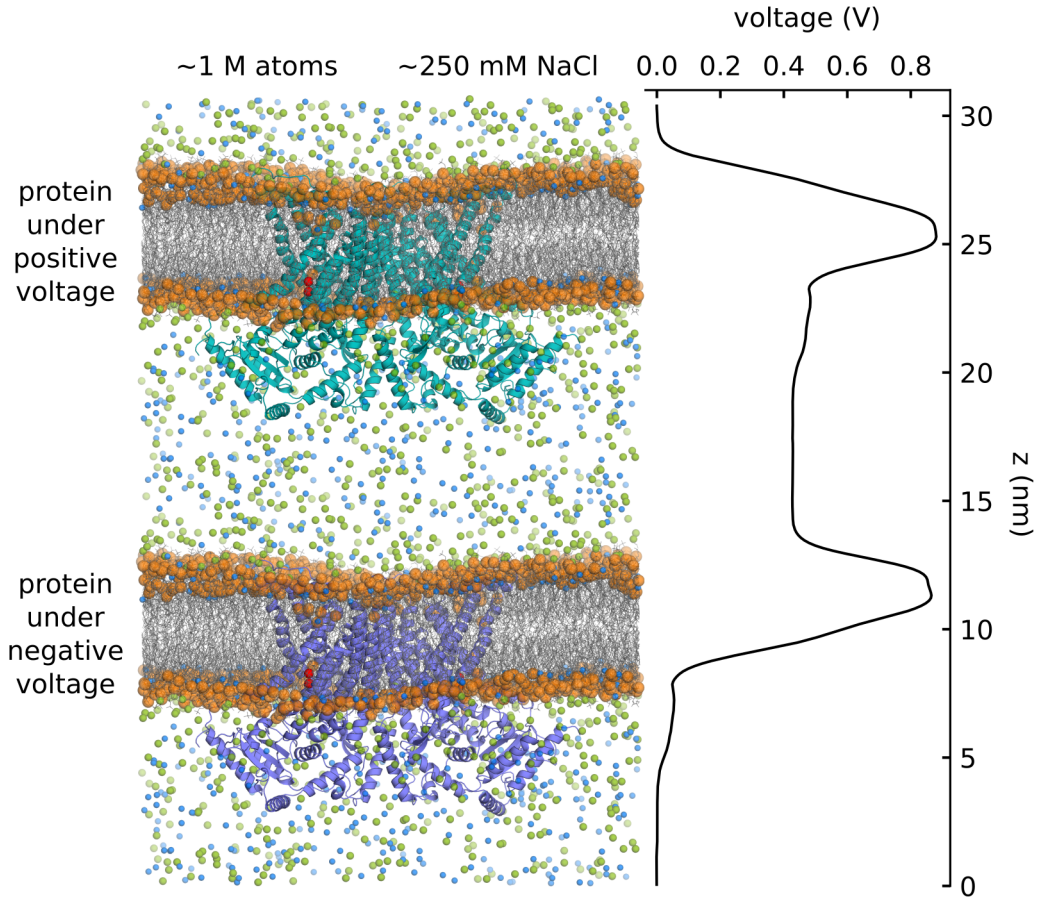

Figure 2.1: "(Left) Setup of a double bilayer simulation used to study ion conduction by the CompEL method. Two copies of nhTMEM16 were embedded into the lipid bilayers in a parallel orientation, with the top protein (teal) subjected to positive voltages and the bottom protein (violet) to negative voltages via the higher number of Na^+ ions in the middle compartment. Phosphorus atoms and lipid tails are shown as orange spheres and gray lines, respectively. Na^+, Cl^-, and Ca^{2+} ions are shown as blue, green, and red spheres, respectively. Water is omitted for clarity."[A] (Right) The voltage profile through the system. A charge imbalance of 20 elementary charges gave rise to a transmembrane voltage of about 400 mV. The figure was partly adapted from [A].

gorithm swaps ions between the compartments once an ion permeation event occurs. Thus, the method is conceptually similar to the experimental setups, where the transmembrane voltage is virtually controlled by adsorbing/releasing Cl^- ions from/to the solution by Ag/AgCl electrodes. The intercompartment charge imbalance was checked every 10 ps and averaged over 100 ps; ions were swapped only when the average value deviated by more than one elementary charge from the reference dQ. Full information on the systems, including simulation times and voltages, can be found in Tables A.1–A.8."[A]

Protein	nhTMEM16		TMEM16K
PDB ID	4WIS [24]	6QMA [56]	5OC9 [21]
Conformation	fully open	intermediate	fully open
Method	X-ray	cryo-EM	X-ray
Resolution	3.3 Å	3.7 Å	3.2 Å

Table 2.1: Structures of TMEM16 lipid scramblases used in this study.

2.3 Simulation and analysis details

Protein models

Models of TMEM16 lipid scramblases in different conformations were built based on the structures listed in Table 2.1. In particular, "the fully open state of nhTMEM16 was modeled based on the X-ray structure (PDB ID: 4WIS) [24] with a final residue range of 18–722 and the cryo-EM structure (PDB ID: 6QMA) [56] was used to build a model of the intermediate state with a final residue range of 13–722. The fully open state of TMEM16K was modeled based on the X-ray structure (PDB ID: 5OC9) [21] with a final residue range of 14–642. In all protein models, the N- and C-termini were capped with acetyl and N-methyl, respectively. All Ca^{2+} ions present in the original structures of nhTMEM16 were preserved, whereas the luminally bound Ca^{2+} ion present in TMEM16K was removed after system equilibration because it almost immediately dissociated when position restraints were removed. Missing residues that were unresolved in the original structures were restored using Modeller version 9.18 [81]. The standard protonation state at neutral pH was assigned to all residues, except for protonated H611 in nhTMEM16, which is located at the dimer interface and forms a salt bridge with residue E610 of the other protomer."[A]

Simulation parameters

"All simulations were conducted using the GROMACS software package [82] versions 2016, 2018, and 2019. CHARMM36 force field parameters were used for lipids [83] and CHARMM36m force field parameters for proteins [69]. Ions were described using default CHARMM parameters and the CHARMM TIP3P model was used for water molecules. Integration time step of 2 fs was used and all hydrogen-involving bonds were constrained with LINCS [76]. Van der Waals interactions were calculated with the Lennard-Jones potential and a cutoff radius of 1.2 nm, with forces smoothly switched to zero in the range of 1.0–1.2 nm and no dispersion correction applied. Electrostatic interactions were calculated by the particle mesh Ewald method [77], with a real-space cutoff distance of 1.2 nm. All simulations were done in isothermal-isobaric ensemble, with the temperature set to 310 K using the v-rescale thermostat [66] and a time constant of 0.5 ps. The thermostat was applied separately to a protein with bound Ca^{2+} ions, a lipid bilayer, and a water solution containing ions. The same groups were used for the removal of center-of-mass linear motion. A pressure of 1 bar was imposed using either the Berendsen [65] or Parrinello-Rahman [67] barostat in a semi-isotropic manner with a time constant of 5 ps."[A]

System preparation

"Protein models were embedded in the equilibrated lipid membranes using the *g_membed* functionality [84] in GROMACS. The initial protein orientation within the membrane was guided by the corresponding structure from the Orientations of Proteins in Membranes database [85]."[A] Membranes of different lipid compositions were used: neutral POPC membrane was composed of 1-palmitoyl-2-oleoyl-phosphatidylcholine (POPC) molecules, negatively charged POPE:POPG membrane was composed of neutral 1-palmitoyl-2-oleoyl-phosphatidylethanolamine (POPE) and anionic 1-palmitoyl-2-oleoyl-phosphatidylglycerol (POPG) in a 3:1 ratio, and negatively charged POPC:POPS membrane contained POPC and anionic 1-palmitoyl-2-oleoyl-phosphatidylserine (POPS) in a 1:1 ratio. "The lipids were symmetrically distributed between the leaflets of the mixed membranes to model the condition of lipid distribution equilibrated by an active lipid scramblase. Chloride and sodium ions were added to reach a bulk salt concentration of 250 mM. All bilayers were equilibrated in the 250 mM NaCl water solution for at least 500 ns prior to protein insertion."[A]

Equilibration

"The system comprising a lipid bilayer and embedded protein was equilibrated in four steps. First, water and ions were equilibrated for 4 ns, with all Ca^{2+} ions and protein and lipid heavy atoms restrained by a harmonic potential with a force constant of 1000 kJ mol^{-1} nm^{-2}. The lipid heavy atoms were restrained only in the z dimension. The water oxygens resolved in the crystal structure of TMEM16K were also restrained. Second, restraints on the lipid heavy atoms (except for phosphorus) were removed and lipids were allowed to equilibrate in the xy plane around the protein for 50–200 ns. Third, restraints on the phosphorus atoms and on protein loops that were missing in the original structures were released so that the latter could relax for another 50 ns. Finally, side chains and Ca^{2+} ions were allowed to equilibrate for 10 ns, with restraints only on the backbone atoms of non-loop protein regions. In TMEM16K systems, restraints on the water oxygens present in the crystal structure were also released."[A]

Analysis

"Prior to analysis, trajectories were translationally and rotationally fitted onto the transmembrane region of the original protein structure and sampled every 100 ps. To calculate the properties of ions and water in the subunit cavity the region of interest was limited to a box of size 25 Å×40 Å×80 Å built around the reference atom of the pore center (Cα of S382 in nhTMEM16 and Cα of C412 in TMEM16K). The box was symmetrical with respect to the reference atom in the y and z dimensions, but was shifted by 7.5 Å toward the protein periphery in the x dimension to exclude the dimer interface from the analysis. The box was large enough to fully accommodate the interior of the subunit cavity as well as the entrances to it."[A]

"GROMACS tools and bespoke python scripts using the MDAnalysis library [86] were used for all analyses. All visualizations were done in PyMOL version 1.8."[A]

Chapter 3

Conductive states of TMEM16 lipid scramblases

The mechanistic models of ion conduction[1] in TMEM16 lipid scramblases, which have been suggested so far, are mainly based on the static protein conformations resolved by the structural studies. The models are mutually exclusive, assuming that only one of the resolved structures is compatible with ion conduction. However, since the models differ only in molecular-level details, they can hardly be tested directly by functional studies. In contrast, state-of-the-art MD simulations provide a means for the model testing that allows for the direct assignment of the functional properties to the structural states of the proteins. In particular, such functional property as ion conductance can be calculated from the simulations individually for a particular conformation of the pore. In this chapter, we describe ion conductance, structural dynamics, and pore hydration of different conformations of nhTMEM16 and TMEM16K, to conclude on the main ion-conductive state of TMEM16 lipid scramblases.

3.1 Ion conductance

nhTMEM16

In the Ca^{2+}-bound state, the subunit cavity of nhTMEM16 has been shown to adopt closed, intermediate and fully open conformations [56]. The structural studies demonstrated incompatibility of the closed conformation with ion conduction, whereas the subunit cavity in the intermediate and fully open conformations was proposed to be wide enough to allow ion permeation [49, 56]. The models suggested so far assume that only one conformation is ion conductive. Therefore, we first tested competence of nhTMEM16 in the intermediate and fully open conformations for ion conduction.

[1] In this work, the term 'ion conduction' refers to the process of ion permeation, whereas the term 'ion conductance' refers to the quantity that characterizes this process.

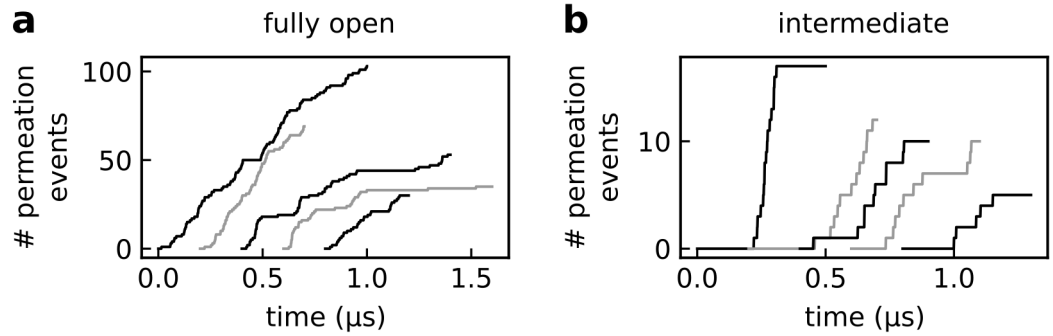

Figure 3.1: a, **b** Time courses of number of ion permeation events through nhTMEM16 protomers in fully open (**a**) and intermediate (**b**) conformations. The data are shown for five protomers in each conformation with the highest total number of events. The time courses are ordered from left to right in the descending order of the total number of ion-permeation events. The starting times of the time courses are separated by 200 ns, for clarity.

In the simulations with applied voltage, both nhTMEM16 conformations were permeable to ions, which were conducted exclusively through the subunit cavity, in accordance with the previously reported MD simulations of nhTMEM16 in the fully open conformation [43]. Therefore, each event could be assigned to a particular protomer of the dimeric nhTMEM16. Number of the ion-permeation events was then counted in time for each simulated protomer. As an example, Figure 3.1 shows such time courses for a number of protomers with the highest total number of ion permeation events. Hundreds of ion permeation events were observed in the fully open conformation, and only tens in the intermediate conformation, indicating higher ion conductance of the former.

To quantify the difference in ion conductance between the intermediate and fully open conformations, we calculated their mean ion conductance from the simulations. "To focus only on the conductive state of the pore and exclude the bias due to the pore priming for ion conduction, we defined the mean conductance as

$$G_m = \frac{N_p \cdot e}{V \cdot (t - t_1)}, \tag{3.1}$$

where N_p is the total number of permeation events, e is the elementary charge, V is the transmembrane voltage, t is the total simulation time, and t_1 is the time of the first permeation event. Thus, the part of the simulation prior to the first permeation event was skipped to exclude from the analysis the phase of the initial transition of the pore to the conductive state."[A] Such transition is related to the delay in ion conduction, which can be seen in Figure 3.1. The mean ion conductance was calculated for each simulated protomer, as shown in Figure 3.2a. The median value of the mean conductance calculated over the protomers in the fully open conformation was roughly doubled compared to that in the intermediate conformation (9.1 pS vs. 4.5 pS; Figure 3.2a).

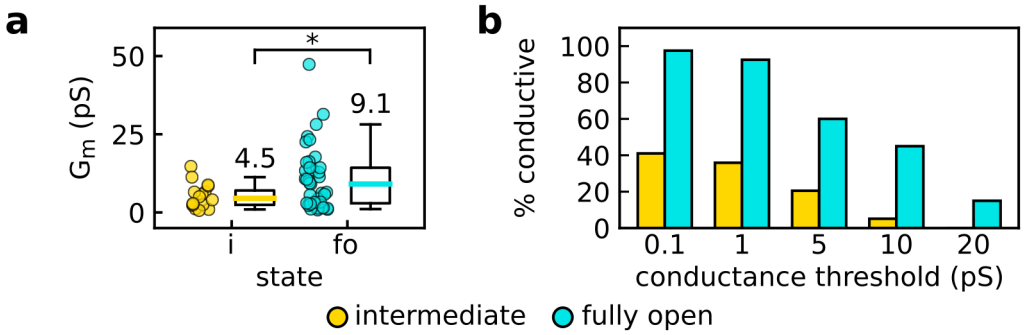

Figure 3.2: **a** Mean conductance of nhTMEM16 in the intermediate and fully open conformations. Each data point represents an independent protomer (n_i=16, n_{fo}=39, p=0.03.). Whiskers show the 5th and 95th percentiles. Significance was evaluated with the Mann-Whitney test, one-sided: $p < 0.05$ (*). **b** Percent of conductive protomers in simulations of nhTMEM16 in the intermediate and fully open conformations. The figure was adapted from [A].

To estimate open-channel probability of nhTMEM16 in different conformations we calculated the fraction of ion-conductive protomers in our simulations. In contrast to experiments, high temporal and spatial resolution of atomistic MD simulations makes it possible to detect a single ion-permeation event, providing for virtually infinite sensitivity of ion-current detection. As a result, open-channel probability depends on a threshold used to distinguish open and closed states of the channel. Figure 3.2b shows a percent of ion-conductive protomers observed in the simulations for different values of the conductance threshold. Regardless of the threshold value, percent of conductive nhTMEM16 protomers (and therefore the open-channel probability) in the fully open conformation was more than two times higher than that in the intermediate conformation (Figure 3.2b). Moreover, none of the simulated protomers in the intermediate conformation demonstrated the mean conductance higher than 20 pS, in contrast to the fully open conformation (Figure 3.2a, b).

By definition, the mean conductance characterizes the channel in a certain macrostate, which is defined by its initial structure. This macrostate can comprise different microstates, which are sampled during a simulation trajectory and are characterized by different levels of ion conductance. Thus, the mean conductance reports on the average ion conductance of all the microstates constituting a single macrostate. Here, we took advantage of the high resolution inherent to MD simulations, to characterize different conformations of nhTMEM16 by the ion conductance of the dominant microstate. To this end, we calculated the median instantaneous ion conductance for each protomer during the simulation trajectory. "Instantaneous conductance was defined as

$$G_i = \frac{e}{V \cdot \Delta t}, \tag{3.2}$$

where e is the elementary charge, V is the transmembrane voltage, and Δt is the time between two consecutive permeation events. Defined in this way, the instantaneous conductance characterizes a particular microstate of the pore. In turn, the median

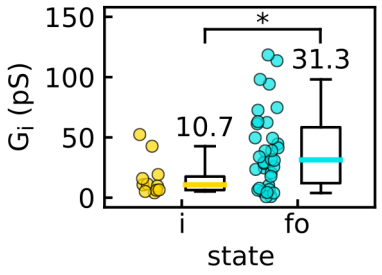

Figure 3.3: Instantaneous conductance of nhTMEM16 protomers in the intermediate (i) and fully open (fo) conformations. Each data point corresponds to a single protomer (n_i=16, n_{fo}=39, p=0.02). Median values are indicated. Whiskers indicate the 5th and 95th percentile. Significance was evaluated with the Mann-Whitney test, one-sided: $p < 0.05$ (*). The figure was adapted from [A].

value of the instantaneous conductance, calculated from a protomer trajectory, reports on the dominant microstate."[A] Because of the signal discretization in experimental single-channel recordings, the dominant microstate would contribute most into the resulting current. Therefore, the median instantaneous conductance should be closer related to the experimental single-channel conductance than the mean conductance. Figure 3.3 shows median instantaneous conductance calculated for each simulated protomer with at least two ion permeation events. "The instantaneous conductance of nhTMEM16 was notably higher in the fully open than in the intermediate conformation of the pore (median values of 31.3 pS and 10.7 pS, respectively; Figure 3.3)."[A]

"The values for instantaneous conductance are in a good agreement with experimentally-observed single-channel conductances for the TMEM16F and fungal TMEM16 scramblases. In particular, the median value of instantaneous conductance for the fully open conformation is remarkably close to the experimentally-determined single-channel conductance reported for TMEM16F as an outwardly rectifying Cl^- channel (50 pS) [26]. On the other hand, the lower ion conductance demonstrated by nhTMEM16 in the intermediate conformation is closer to the single-channel conductance ($\sim$1 pS) reported in another TMEM16F study [13], suggesting that TMEM16F can adopt different ion-conductive states similar to nhTMEM16 and that the experimental conditions might shift equilibrium between these states. Finally, the single-channel conductance reported for afTMEM16 ($\sim$ 300 pS) [23] is of the same order of magnitude as the conductance of a number of the fully open protomers that exhibited instantaneous conductances of above 100 pS, indicating full opening of the afTMEM16 cavity in the experiment."[A]

TMEM16K

In contrast to nhTMEM16, human TMEM16K was resolved only in the closed and fully open conformations [21]. Since TMEM16K does not adopt a stable intermediate conformation in the structural experiments, we could only study ion conduction of the fully open conformation. Figure 3.4a shows the mean and instantaneous conductance of the protomers with at least two ion permeation events. The median values of the mean and instantaneous conductance were 3.9 pS and 11.3 pS, respectively. Thus, although the TMEM16K subunit cavity was fully open, its ion conductance was closer to the intermediate than to the fully open conformation of nhTMEM16. Unfortunately, we could not compare our results with experimental data, since single-channel

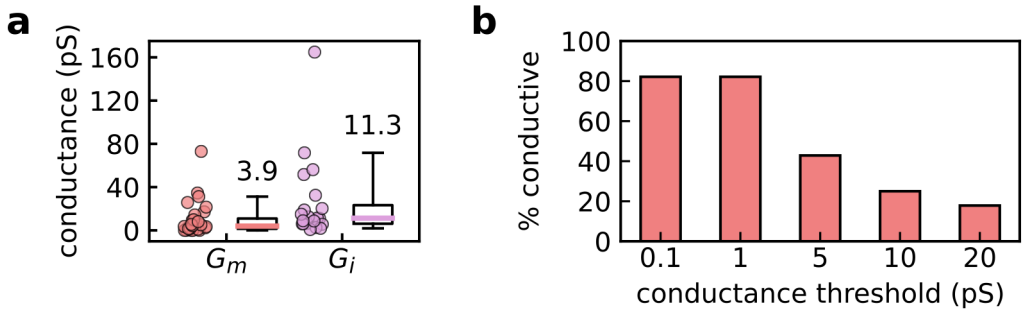

Figure 3.4: **a** Mean conductance (G_m) and median instantaneous conductance (G_i) of TMEM16K protomers. Each data point corresponds to a single protomer. Median values are indicated. Whiskers indicate the 5th and 95th percentile. **b** Percent of conductive TMEM16K protomers depending on the conductance threshold.

conductance has not been yet measured experimentally for TMEM16K, despite recent progress in its relocation to the plasma membrane [87]. In contrast to the ion conductance, overall open-channel probability of TMEM16K (Figure 3.4b) was more similar to the fully open rather than to the intermediate conformation of nhTMEM16 (Figure 3.2b). In particular, the majority of the simulated TMEM16K protomers were conductive at low conductance threshold and some of the protomers demonstrated mean conductance higher than 20 pS (Figure 3.4b). Thus, preserving high open channel probability, TMEM16K in the fully open conformation demonstrates the reduced ion conductance compared to nhTMEM16.

3.2 Width and hydration of the pore

nhTMEM16

Different conformations of TMEM16 lipid scramblases deffer mainly in the width of the subunit cavity. In particular, the extracellular part of the cavity is sealed in the intermediate and closed conformations. Given that the open-channel probability was higher in the fully open conformation, we tested if the cavity width correlated with the ion conduction. The width of the nhTMEM16 cavity was measured as distance between Cα atoms of T333 and Y439, which are located at the opposite sides of the cavity in its central part (Figure 3.5a). In the intermediate conformation, the width of protomers which remained impermeable to ions during the simulation at applied voltage was similar to that of the protomers simulated in the absence of voltage (Figure 3.5b). In contrast, the ion-conductive protomers in the intermediate conformation demonstrated a noticeable widening of the cavity (Figure 3.5b). In the fully open conformation, the subunit cavity was originally wider, so that the relative increase in its width in the ion-conductive protomers was smaller than in the intermediate conformation (Figure 3.5c). Notably, the subunit cavity of ion-conductive protomers in the fully open conformation was still wider than in the intermediate conformation (1.4 nm vs. 1.1 nm), which indicates that the latter remained semi-closed.

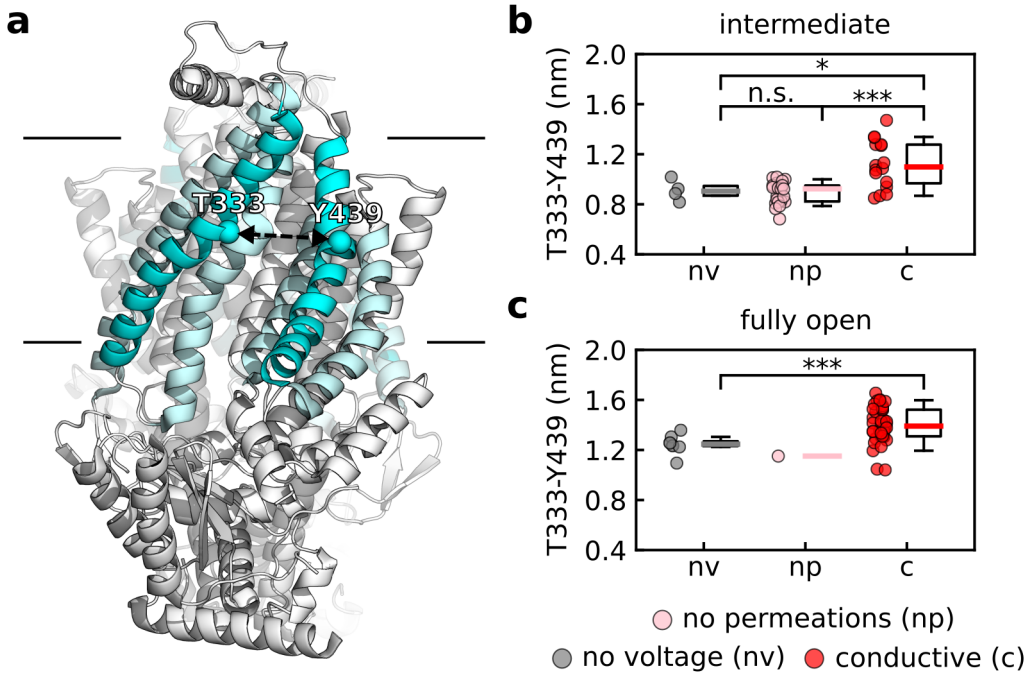

Figure 3.5: **a** Subunit cavity of nhTMEM16 in the fully open conformation is shown in cyan, with the bordering helices highlighted. Atoms used to measure the width are shown as spheres. **b**, **c** Width of the nhTMEM16 pore in the intermediate (**b**) and fully open (**c**) conformations. The width was measured as distance between Cα atoms of T333 and Y439. Each data point corresponds to a single protomer (n_{nv}=4, n_{np}=23, n_c=16, $p_{nv,np}$=0.57, $p_{nv,c}$=0.03, $p_{np,c}$=0.00011 in **b**; n_{nv}=8, n_{np}=1, n_c=39, $p_{nv,c}$=0.0009 in **c**). Whiskers indicate the 5th and 95th percentile. Significance was evaluated with the Mann-Whitney test, one-sided: $p > 0.05$ (n.s.), $p < 0.05$ (*), $p < 0.001$ (***). The figure was partly adapted from [A].

To estimate effect of the widening on the pore hydration, we calculated the number of water molecules accommodated in the narrowest part of the pore in different conformations and states of nhTMEM16 (Figure 3.6a). The pore hydration indirectly reflects free space, which is potentially available for ions, and is, therefore, assumed to be closer linked to the pore permeability than the pore width. In the intermediate conformation, voltage application increased hydration of the nhTMEM16 pore, with the effect being more pronounced in the ion-conducting than in the ion-impermeable protomers (Figure 3.6b). When voltage was applied to nhTMEM16 in the fully open conformation, only a mild increase in the pore hydration was observed (Figure 3.6c). Importantly, the ion-conductive protomers demonstrated similar hydration regardless of their initial conformation, with median values of 16 and 18 water molecules in the intermediate and fully open conformations, respectively. Thus, although the subunit cavity is less open in the intermediate compared to the fully open conformation, in the ion-conductive state it can accommodate a similar number of water molecules, indicating comparable amount of free volume within the pore.

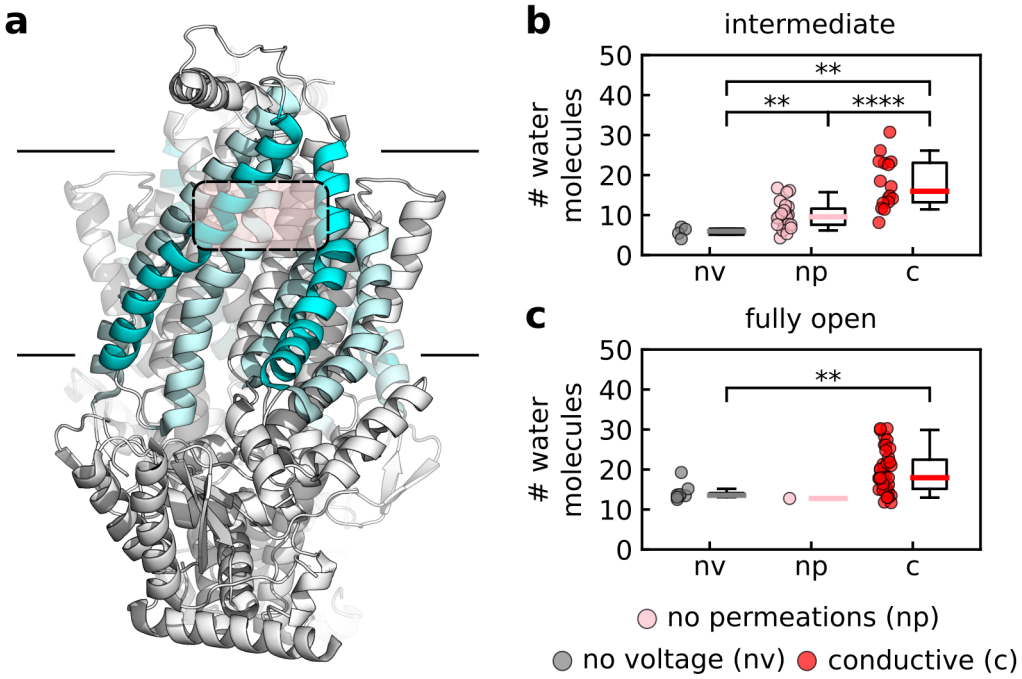

Figure 3.6: **a** Subunit cavity of nhTMEM16 in the fully open conformation is shown in cyan, with the bordering helices highlighted. The region used to measure the hydration is indicated. **b,c** Hydration of the nhTMEM16 pore in the intermediate (**b**) and fully open (**c**) conformations. The hydration was measured as number of water molecules in the extracellular part of the subunit cavity. Each data point corresponds to a single protomer (n_{nv}=4, n_{np}=23, n_c=16, $p_{nv,np}$=0.006, $p_{nv,c}$=0.002, $p_{np,c}$=0.00003 in **b**; n_{nv}=8, n_{np}=1, n_c=39, $p_{nv,c}$=0.002 in **c**). Whiskers indicate the 5th and 95th percentile. Significance was evaluated with the Mann-Whitney test, one-sided: $p < 0.01$ (**), $p < 0.0001$ (****). The figure was partly adapted from [A].

TMEM16K

In TMEM16K, the subunit-cavity width was measured as the distance between Cα atoms of S363 and T435, which are homologous to T333 and Y439 of nhTMEM16 (Figure 3.7a). Width of the subunit cavity of ion-impermeable protomers was unaffected by voltage application (Figure 3.7b). In the ion-conductive protomers, the subunit cavity demonstrated higher variance in width, whose median value, however, was only insignificantly increased compared to the zero-voltage conditions (1.2 nm vs. 1.1 nm). Similar trends were also observed in the pore hydration, which closely reflected the changes in the pore width (Figure 3.7c). In particular, only a minor difference in the pore hydration was observed between the ion-conductive and ion-impermeable protomers. Thus, very similar to nhTMEM16, the fully open conformation of TMEM16K demonstrated only minor changes in width and hydration of the subunit cavity upon voltage application.

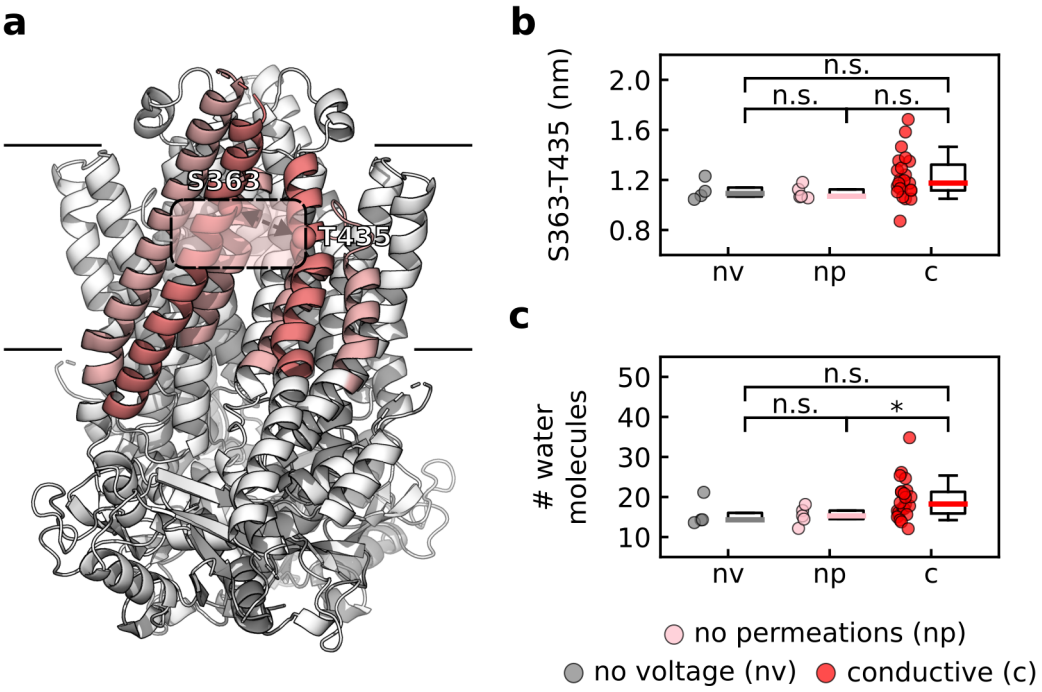

Figure 3.7: a Subunit cavity of TMEM16K in the fully open conformation is shown in red, with the bordering helices highlighted. Atoms used to measure width are shown as spheres and the region used to measure the hydration is indicated. **b** Width of the TMEM16K pore measured as distance between Cα atoms of S363 and T435. **c** Hydration of the TMEM16K pore measured as number of water molecules in the extracellular part of the subunit cavity. **b,c** Each data point corresponds to a single protomer (n_{nv}=4, n_{np}=5, n_c=23, $p_{nv,np}$=0.64, $p_{nv,c}$=0.07, $p_{np,c}$=0.053 in **b**; n_{nv}=4, n_{np}=5, n_c=23, $p_{nv,np}$=0.36, $p_{nv,c}$=0.06, $p_{np,c}$=0.04 in **c**). Whiskers indicate the 5th and 95th percentile. Significance was evaluated with the Mann-Whitney test, one-sided: $p > 0.05$ (n.s.), $p < 0.05$ (*).

3.3 Conclusions

We demonstrated that both the intermediate and fully open conformations of TMEM16 lipid scramblases are ion conductive, refuting the "alternating-pore" model, which assigns lipid scrambling and ion conduction to different conformations. Moreover, we showed that both ion conductance and open-channel probability are higher in the fully open than in the intermediate conformation of nhTMEM16. The fully open subunit cavity does not require a considerable widening to initiate ion conduction in contrast to the cavity in the intermediate conformation. Having compared ion conduction of TMEM16 lipid scramblases in the intermediate and fully open conformations, we conclude that more prominent ion conductance, higher open-channel probability, and the less notable conformational changes to initiate ion conduction make the fully open conformation the main ion-conductive state of TMEM16 lipid scramblases.

Chapter 4

Proteolipidic structure of the fully open pore

The fully open subunit cavity provides a pathway for lipid headgroups across the membrane and thereby underlies the scrambling functionality of TMEM16 lipid scramblases. Therefore, in the main ion conductive state TMEM16 lipid scramblases are assumed to conduct ions through the proteolipidic pore, which is formed by the subunit cavity and lipid headgroups. In this chapter, we scrutinize structural organization of the proteolipidic pore with a particular focus on the lipid headgroups as its dynamic cavity-stabilized element.

4.1 nhTMEM16

Lipid headgroups populated the fully open subunit cavity of nhTMEM16 both at positive and negative voltages, as can be seen from representative snapshots shown in Figure 4.1a. To structurally characterize the headgroup arrangement within the cavity, we calculated local probability density distributions of lipid phosphorus and nitrogen atoms within the pore along the outward membrane normal (Figure 4.1b,c). Locality was ensured by considering only four atoms closest to the pore center defined as Cα of S382. "The distribution peaks indicate the localization sites of POPC choline (nitrogen) and phosphate groups at the extracellular (pe, ne) and central (pc, nc) sections of the cavity (Figure 4.1), consistent with previous reports [43, 48]. In turn, the wide intracellular peaks in the phosphorus and nitrogen distributions correspond to the lipid headgroups forming intracellular border of the membrane. Notably, the height of the central phosphorus peak increased when a voltage was applied (Figure 4.1b), suggesting that transmembrane voltages might affect lipid-scrambling rates by stabilizing headgroups within the cavity."[A]

To better understand molecular underpinnings of the lipid headgroup arrangement, we estimated probability of the headgroup moieties to form contacts with cavity

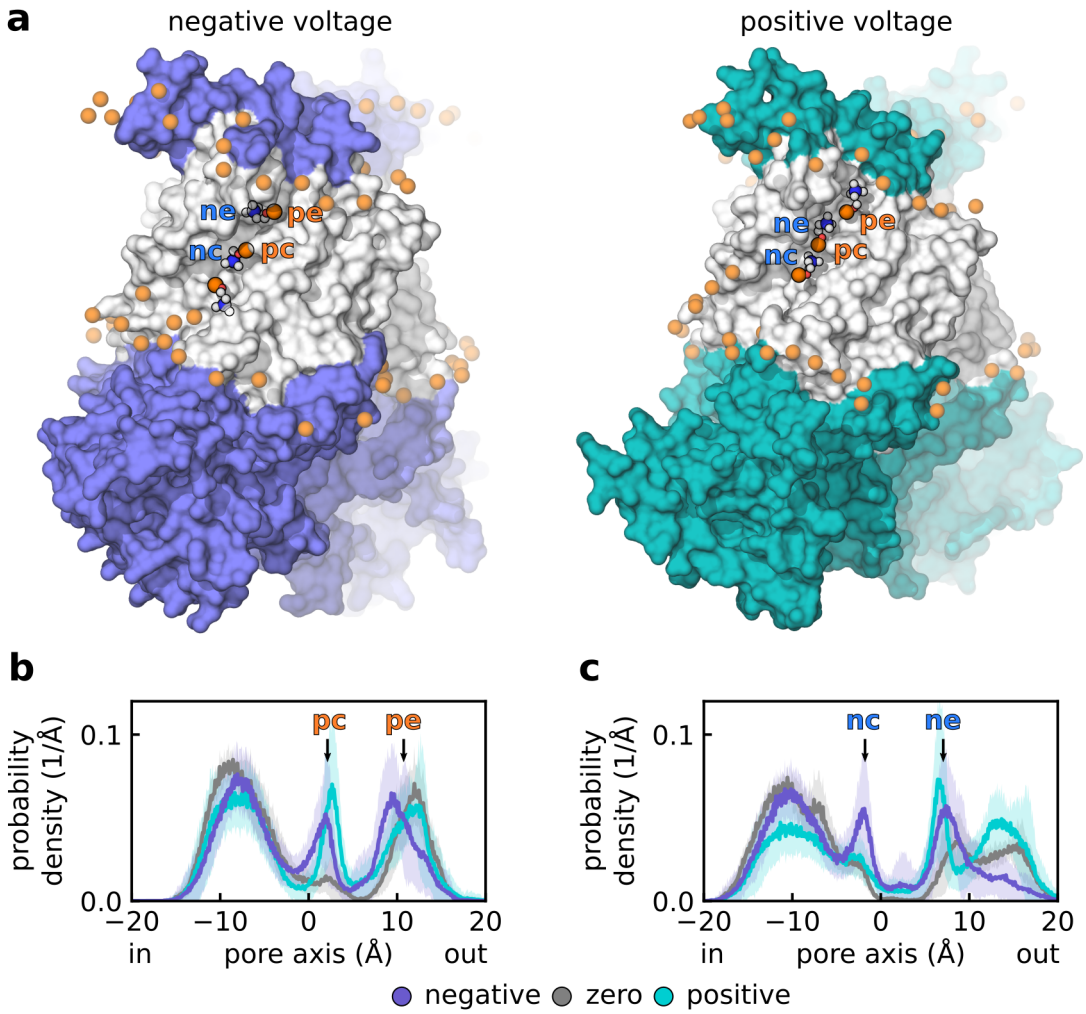

Figure 4.1: a Snapshots illustrating arrangement of POPC lipid headgroups in the subunit cavity of nhTMEM16 at positive and negative voltages. The transmembrane part of the protein is shown in white. Phosphorus, nitrogen, carbon, and oxygen atoms of lipid headgroups are shown as orange, blue, white, and red spheres, respectively. **b**, **c** Local probability density distribution of POPC phosphorus (**b**) and nitrogen (**c**) atoms along the subunit cavity at negative, zero, and positive voltages. Distributions were calculated with respect to the pore center. Average distributions across independent protomer simulations are shown, with shaded areas representing the standard error of mean. The figure was adapted from [A].

residues. "Lipid localization sites used for the analysis were defined based on the phosphorus and nitrogen distributions and covered the following regions along the pore axis (in Å): pc [-3:7], nc [-5:0], pe [7:17], and ne [5:10]."[A] "We found that the pe phosphate and nc choline groups[1] are rather loosely coordinated by the surrounding

[1]The labels of the distribution peaks are also used to specify a particular headgroup moiety that occupies a corresponding site.

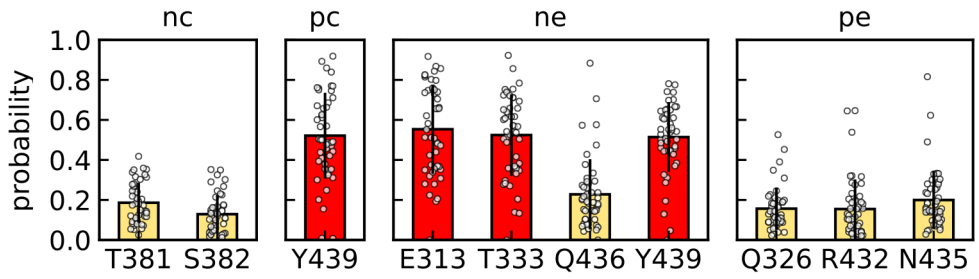

Figure 4.2: Probability that oxygen or nitrogen atoms of hydrophilic residues are in a direct contact (distance of < 5 Å) with either the phosphorus or nitrogen atoms of POPC headgroups at their localization sites within the nhTMEM16 subunit cavity. Only residues with a contact probability of > 10 % are shown (those with a contact probability of > 35 % are highlighted in red). Each data point corresponds to a single protomer. Error bars represent the standard deviation. The figure was adapted from [A].

residues, with no residue demonstrating a greater than 20% probability of making direct contact with headgroup moieties (Figure 4.2). At the same time, groups at the pc and ne sites were notably stabilized by cavity residues (Figure 4.2). In particular, the central lipid headgroup was held in position via a hydrogen bond between its phosphate and Y439 (Figure 4.2 and Figure 4.3a). Of note, a substantial role for this tyrosine in both scrambling and protein activation, has recently been demonstrated [43, 49, 50]. In turn, the ne choline group is coordinated by E313 and T333, and tryptophan substitution of the former residue was previously shown to significantly decrease the ion channel activity of nhTMEM16 [50]. Despite the importance of the E313/E318/R432 triad for the scrambling activity of nhTMEM16 [50], E318 and R432 seem to have less prominent roles in headgroup stabilization compared with E313: R432 has a much lower probability to coordinate the phosphate group at the pe site and E318 scarcely makes any contact with the headgroups (Figure 4.2)."[A]

"Interestingly, due to their inherent dipole moment, lipid headgroups within the cavity are oriented in accordance with the direction of the applied electric field (Figure 4.3). Difference in the orientation of headgroups in the presence of positive and negative voltages can be clearly seen in the central part of the cavity. More precisely, the headgroup located at the central pc site adopts an upward orientation at positive voltages and a downward orientation at negative voltages (Figure 4.3a,b). Consistent with the difference in the headgroup orientation, the distribution peaks of choline nitrogen atoms differ at positive and negative voltages (Figure 4.1c). In particular, the central peak (nc) is prominent only when a negative voltage is applied, corresponding to a downward orientation of the headgroup at the central site. At the same time, an external nitrogen peak (ne) is formed by a choline belonging to the headgroup located at the pc or pe site, respectively, when a negative or positive voltage is applied."[A]

"Notably, in our nhTMEM16 simulations we observed six complete lipid-scrambling events, where lipids were transported along the fully open subunit cavity. While cross-

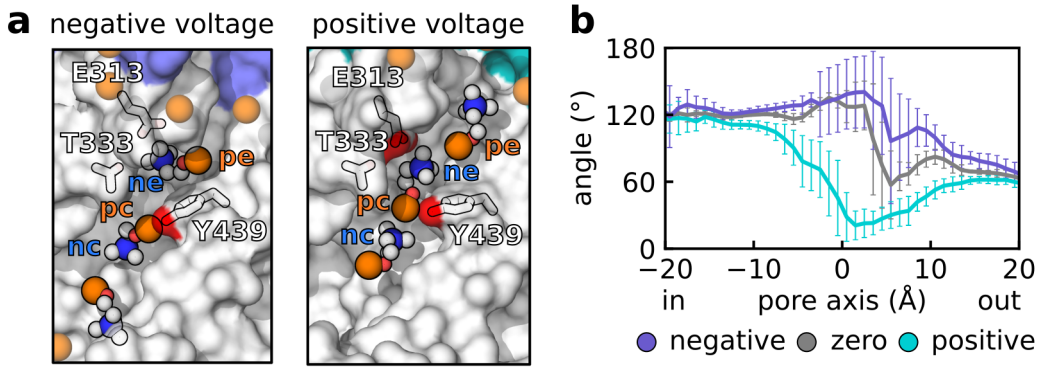

Figure 4.3: a Snapshots illustrating coordination of POPC headgroups by nhTMEM16 residues within the subunit cavity. Phosphorus, nitrogen, carbon, and oxygen atoms of lipid headgroups are shown as orange, blue, white, and red spheres, respectively. The residues coordinating the POPC headgroups are shown as sticks. **b** Distribution of angle between a POPC headgroup and the outward membrane normal in the nhTMEM16 systems at negative, zero, and positive voltages. The upright and downright orientations correspond to 0° and 180°, respectively. The figure was adapted from [A].

voltage polarity	positive			negative		
scrambling direction	down	down	up	up	up	up
orientation angle	28.4	20.7	25.8	140.9	131.4	142.4

Table 4.1: Summary of the POPC scrambling events observed in the nhTMEM16 simulations. The orientation angle was measured for a transported lipid headgroup when its phosphorus atom occupied the central accumulation site.

ing the central site, the headgroup of the translocated lipids were oriented according to the voltage polarity (Table 4.1). At positive voltage two out of three scrambled lipids were translocated from the upper to the inner leaflet of the membrane. Another lipid scrambled at positive voltage as well as all three scrambled lipids at negative voltage were translocated in the opposite direction. Although these data may indicate a possible correlation between the voltage polarity and headgroup orientation with direction of the lipid translocation, a higher number of the scrambling events or usage of enhanced-sampling techniques would be required for a robust conclusion on the effects of voltage on the lipid scrambling mediated by TMEM16 proteins."[A]

4.2 TMEM16K

Similar to nhTMEM16, in the fully open conformation the subunit cavity of TMEME16K is populated by lipid headgroups (Figure 4.4a). However, due to the narrower intracellular part, the subunit cavity of TMEM16K accommodates higher number of structured lipid headgroups compared to nhTMEM16. To take this into account, we used five instead of four lipid headgroups closest to the pore center, which

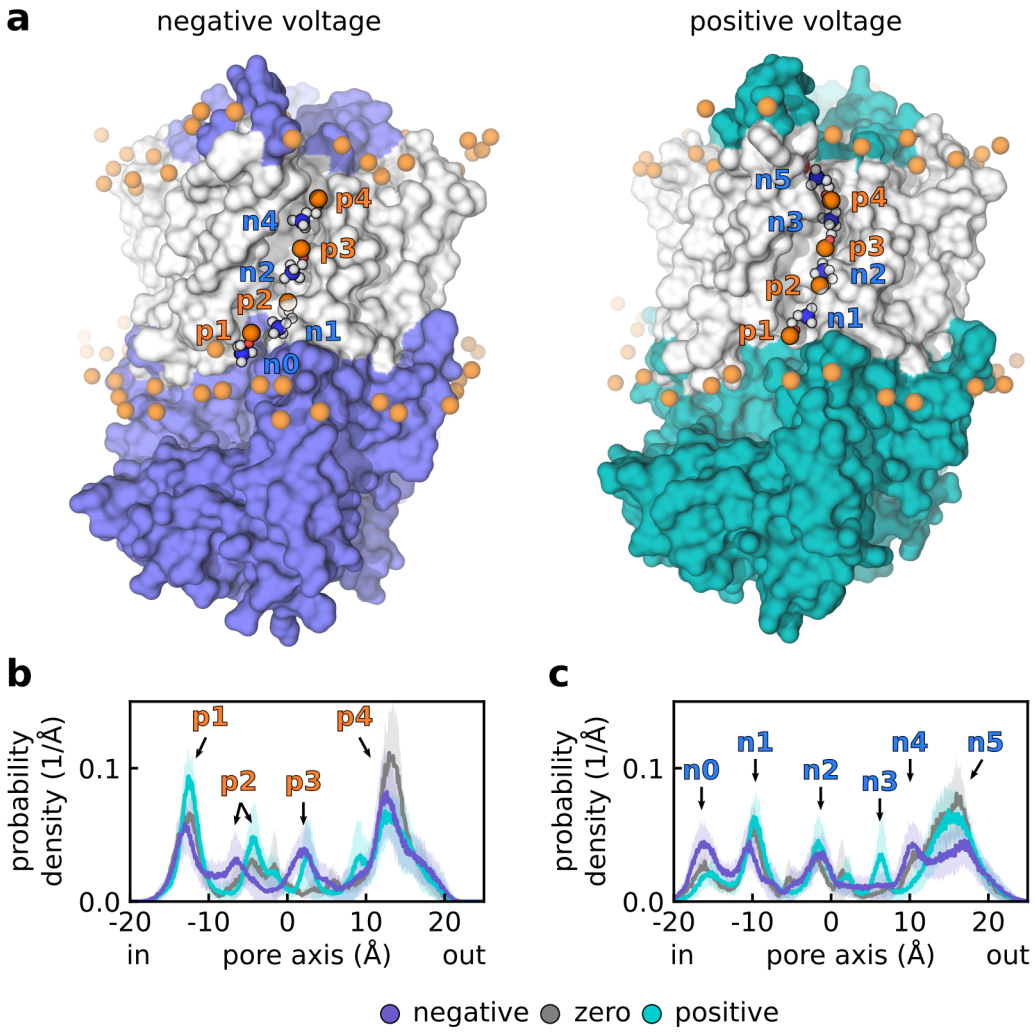

Figure 4.4: a Snapshots illustrating arrangement of lipid headgroups in the TMEM16K subunit cavity at positive and negative voltages. The transmembrane part of the protein is shown in white. Phosphorus, nitrogen, carbon, and oxygen atoms of lipid headgroups are shown as orange, blue, white, and red spheres, respectively. **b**, **c** Local probability density distribution of POPC phosphorus (**b**) and nitrogen (**c**) atoms along the subunit cavity at negative, zero, and positive voltages. Distributions were calculated with respect to the pore center. Average distributions across independent protomer simulations are shown, with shaded areas representing the standard error of mean. The figure was adapted from [A].

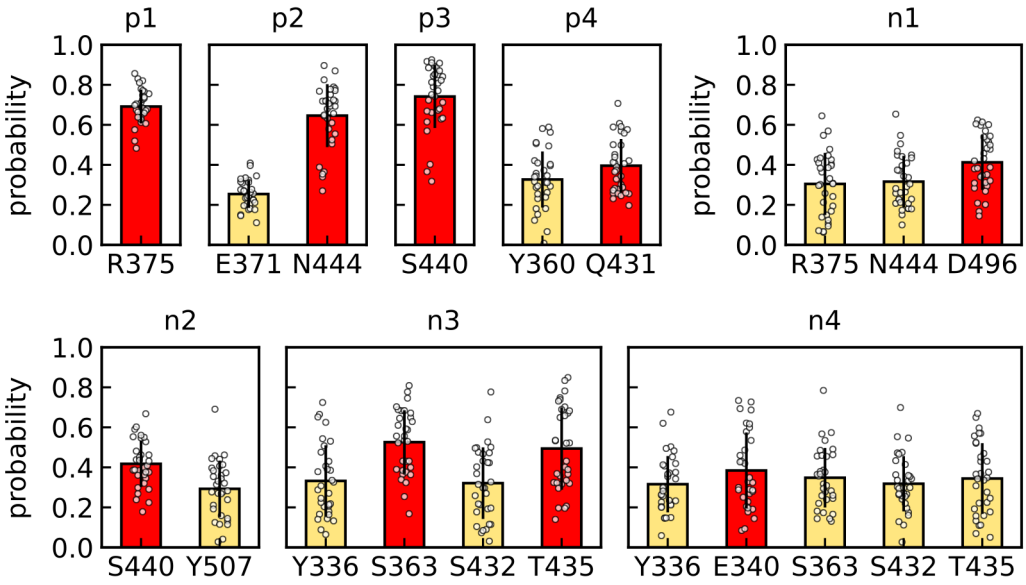

Figure 4.5: Probability that oxygen or nitrogen atoms of hydrophilic residues are in a direct contact (distance of < 5 Å) with either the phosphorus or nitrogen atoms of POPC headgroups at their localization sites within the TMEM16K subunit cavity. Only residues with a contact probability of > 10 % are shown (those with a contact probability of > 35 % are highlighted in red). Each data point corresponds to a single protomer. Error bars represent the standard deviation. The figure was adapted from [A].

was defined as Cα of C412, to calculate the local distribution of their phosphorus and nitrogen atoms along the subunit cavity. In accordance with generally more ordered lipid headgroups, the number of peaks in the phosphorus and nitrogen distributions is higher in TMEM16K (Figure 4.4b, c) compared to nhTMEM16 (Figure 4.1b, c).

In TMEM16K, the localization sites of the phosphorus and nitrogen atoms of the lipid headgroups were defined as the following regions along the pore axis (in Å): $p1$ [-15:-10], $p2$ [-8:-2], $p3$ [0:5], $p4$ [10:15], $n0$ [-18:-13], $n1$ [-12:-7], $n2$ [-4:1], $n3$ [4:9], $n4$ [8:13], and $n5$ [13:18]. Analysis of the contacts between POPC headgroups and residues forming the TMEM16K subunit cavity demonstrated that "the increased headgroup order stems from an extended network of interactions that stabilize the headgroups (Figure 4.5): seven residues coordinate lipid headgroups with a contact probability of > 35 % in TMEM16K (Figure 4.5), compared with three residues in nhTMEM16 (Figure 4.2). In particular, at the extracellular part of the cavity the $n4$ and $p4$ groups are stabilized by Q431 and E340 (Figure 4.5, Figure 4.6a), which are homologs of the N435 and E313 residues that coordinate the pe and ne groups in nhTMEM16."[A] In contrast to nhTMEM16, however, lipid headgroups are also noticeably coordinated by residues at the intracellular part of the cavity, with the $p1$, $p2$, and $n1$ sites being formed by R375, N444, and D496, respectively (Figure 4.5). Notably, the bulky Y439, which coordinates phosphate at the central pc site in nhTMEM16, is substituted by the short T435 in

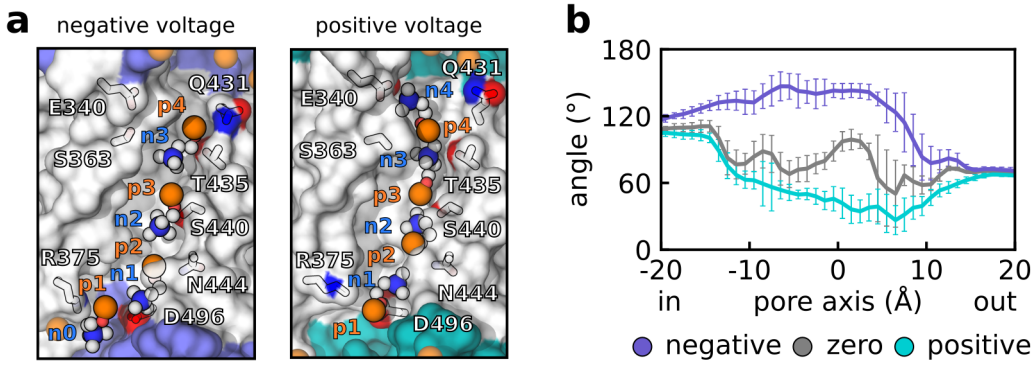

Figure 4.6: a Snapshots illustrating coordination of POPC headgroups by TMEM16K residues within the subunit cavity. Phosphorus, nitrogen, carbon, and oxygen atoms of lipid headgroups are shown as orange, blue, white, and red spheres, respectively. The residues coordinating the POPC headgroups are shown as sticks. **b** Distribution of angle between a POPC headgroup and the outward membrane normal in the TMEM16K systems at negative, zero, and positive voltages. The upright and downright orientations correspond to 0° and 180°, respectively. The figure was adapted from [A].

TMEM16K. Despite this fact, the central phosphate-localization site ($p3$) is preserved in TMEM16K, because of the accompanying substitution of A444 in nhTMEM16 by S440 in TMEM16K, which stabilizes the $p3$ phosphate group and contributes to coordination of the $n2$ choline group (Figure 4.5, Figure 4.6a). "In turn, T435 as well as S363 is involved in coordination of the choline group at the extracellular $n3$ site. Finally, neither the $n0$ nor $n5$ choline groups form stable contacts with any of the cavity-lining residues."[A]

"The orientation of lipid headgroups in the TMEM16K cavity demonstrates the same sensitivity to voltage polarity as in the nhTMEM16 cavity (Figure 4.6)."[A] However, this sensitivity is pronounced in a much longer region of the pore, which roughly corresponds to the region of the ordered lipid headgroups. This suggests that protein stabilization is an important factor for the polarity-induced change in the lipid-headgroup orientation. Due to the higher number of ordered lipid headgroups, more of them are switching orientation upon the voltage-polarity switch. In particular, "the $n0$ peak depends on the headgroup orientation at the $p1$ site and, therefore, on voltage polarity (Figure 4.4c): It is much more prominent at negative voltages similar to the nc peak in nhTMEM16 (Figure 4.1c). Relatedly, at negative voltages the choline groups at the $n1$ and $n2$ sites are part of headgroups whose phosphates localize to the $p2$ and $p3$ sites, respectively, whereas at positive voltages the same choline sites are occupied by headgroups whose phosphates localize to the $p1$ and $p2$ sites (Figure 4.6a)."[A] Finally, occupation of the $n5$ site is more pronounced at positive voltages (Figure 4.4c), when the $n5$ choline group belongs to the headgroup whose phosphate is stabilized at the $p4$ site (Figure 4.6a).

4.3 Conclusions

We demonstrated that in the main ion conductive state the pore of TMEM16 lipid scramblases is lined by lipid headgroups, in consistency with the proteolipidic-pore model. Moreover, we found that the pore-lining headgroups are well ordered within the subunit cavity. While "protein residues provide a general scaffold for energetically favorable lipid interactions with the subunit cavity, the transmembrane voltage significantly influences the specific lipid headgroup arrangement."[A] In particular, choline groups of POPC lipids exchange their localization sites within the subunit cavity upon switching voltage polarity, which defines orientation of lipid headgroups lining the pore. Comparing fungal nhTMEM16 and human TMEM16K lipid scramblases, we also found that it is the cavity-stabilized lipid headgroups that demonstrate the most prominent dependence of their orientation on voltage polarity. Summarizing, in the main ion-conductive state TMEM16 lipid scramblases conduct ions through a structured but still dynamic proteolipidic pore, whose lipidic part constitutes its voltage polarity-sensitive element.

Chapter 5

Permeation and blockage of ions within the proteolipidic pore

The proteolipidic nature of the ion-conducting pore suggests that both the subunit cavity and lipid headgroups lining the pore can directly influence the ion permeation process. In this chapter, we describe atomic-level details of ion-protein and ion-lipid interactions in the pores of nhTMEM16 and TMEM16K, and demonstrate how these interactions shape the energetics of the permeating ions and control the permeability state of the proteolipidic pore.

5.1 Ion accumulation sites

nhTMEM16

To better understand the details of ion permeation in nhTMEM16, we first focused on the ions that crossed the membrane and thereby contributed to the ionic current observed in our simulations. The trajectories of the permeating Cl^- and Na^+ ions through the nhTMEM16 pore are illustrated in Figure 5.1a. These trajectories were used to calculate probability density distributions of the permeating ions, which are shown in Figure 5.1b,c. Based on the distributions, a few ion accumulation sites were identified along the ion permeation pathway. In particular, Na^+ ions dwell at three sites: intracellular Na_i, vestibular Na_v, and extracellular Na_e; and Cl^- ions are accumulated at the vestibular Cl_v and extracellular Cl_e sites. To characterize ions in a site-specific manner, we defined regions along the pore which corresponded to the localization sites. The region bounds along the pore axis (in Å) were: Cl_v [-16:-1], Cl_e [2:17], Na_i [-25:-15], Na_v [-8:2], and Na_e [5:15].

We first evaluated the maximum dwell time of ions at the accumulation sites as the time of the longest visit of an ion to a site during a protomer trajectory. Table 5.1

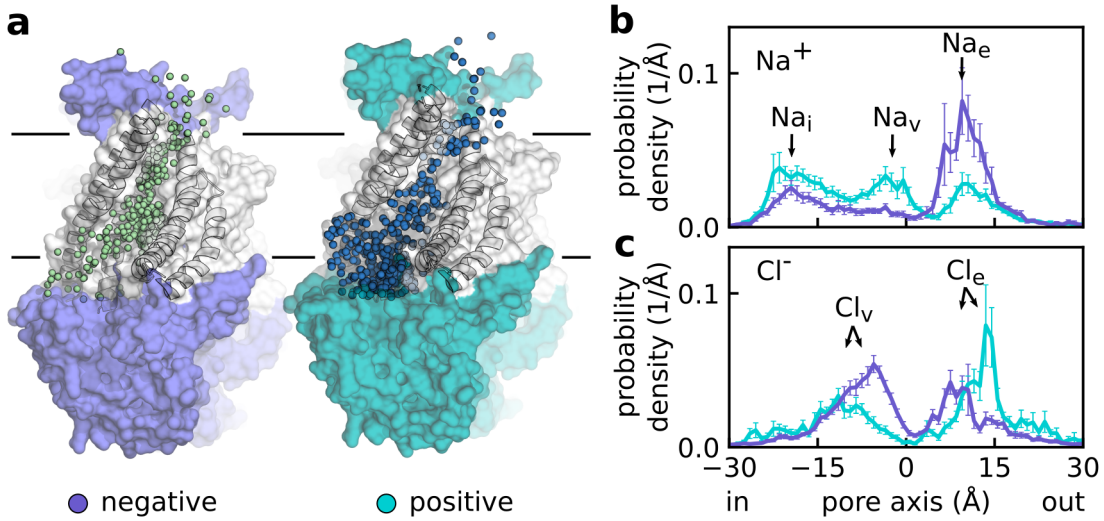

Figure 5.1: a Snapshots illustrating trajectories of permeating Cl^- and Na^+ ions visiting the nhTMEM16 pore region in a representative system with the protein at a negative (left) and positive (right) voltage. Each sphere represents a particular position of a Cl^- (green) or Na^+ (blue) ion in a single frame of the simulation. The transmembrane part of the protein is shown in white, and the membrane borders are schematically depicted. **b**, **c** Probability density distributions of permeating Na^+ (**b**) and Cl^- (**c**) ions along the pore. Ion-localization sites (Na_i, Na_v, Na_e, Cl_v, Cl_e) are indicated. The figure was partly adapted from [A].

site	Cl_v	Cl_e	Na_i	Na_v	Na_e	pc	pe
time (ns)	8.6	8.1	8.6	4.3	5.9	118.5	104.8

Table 5.1: Maximum dwell time of ions and lipid headgroups at the accumulation sites in the nhTMEM16 pore. Presented are median values calculated over all the simulated protomers.

lists the median values that were calculated over all the simulated nhTMEM16 protomers. All the ion accumulation sites were characterized by a maximum dwell time of < 10 ns, indicating fast dynamics of ions within the nhTMEM16 pore. To compare the time scales of ion and lipid presence within the subunit cavity, we also estimated maximum dwell time of phosphate groups at the pc and pe accumulation sites (Table 5.1). Notably, lipid headgroups stayed at their accumulation sites at least one order of magnitude longer than ions, indicating a clear time-scale separation between ion permeation and lipid scrambling.

We then scrutinized the molecular interactions stabilizing ions at their localization sites. Specifically, we calculated frequency of an ion to be in contact (distance of < 5 Å) with oxygen or nitrogen atoms of polar residues or phosphorus or nitrogen atoms of lipid headgroups. When Cl^- ions occupy the extracellular site, they form contacts with all the polar residues lining the narrow extracellular mouth of the pore,

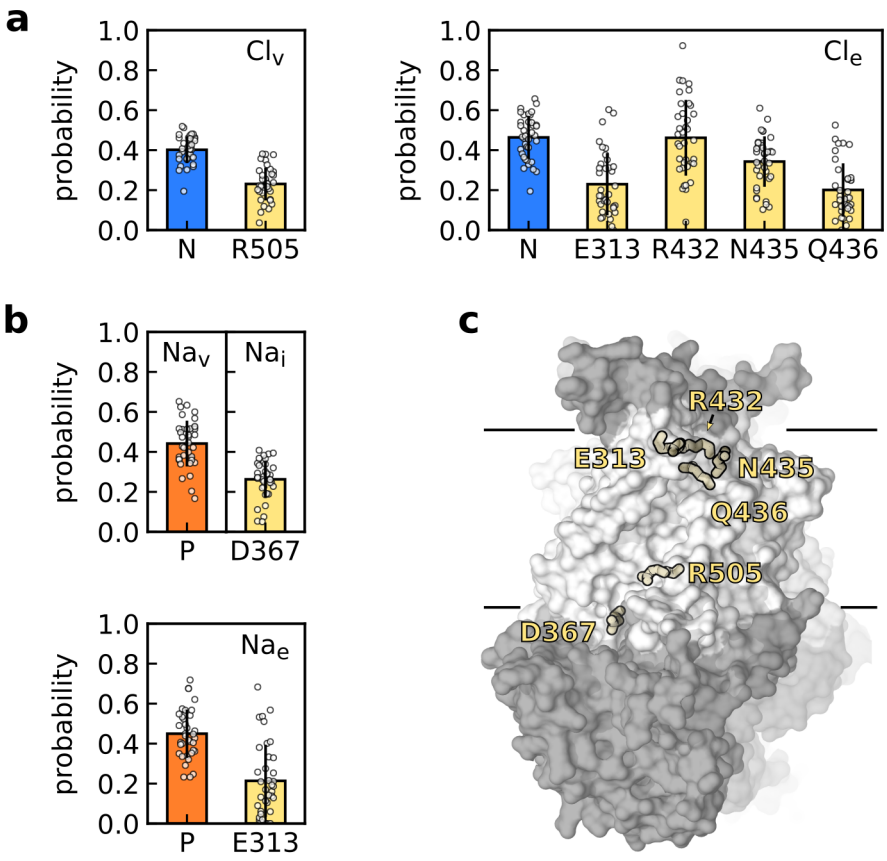

Figure 5.2: "**a**,**b** Probability that oxygen or nitrogen atoms of hydrophilic nhTMEM16 residues or phosphorus or nitrogen atoms of POPC headgroups are in direct contact (distance of < 5 Å) with a permeating Cl^- (**a**) or Na^+ (**b**) ion at a particular localization site (Na_i, Na_v, Na_e, Cl_v, Cl_e) within the pore. Only residues with a contact probability of > 20 % are shown. Each data point corresponds to a single protomer. Error bars represent the standard deviation. **c** Residues indicated in **a** and **b** are mapped onto the nhTMEM16 subunit cavity structure. The transmembrane part of the protein is shown in white, and the membrane borders are schematically depicted."[A] The figure was adapted from [A].

including R432, N435, Q436, and E313 (Figure 5.2a,c). Additionally, the Cl^- ions are stabilized by the positively charged choline group of POPC (Figure 5.2a). Notably, the position of the Cl_e peak in the ion distribution depends on the voltage polarity (Figure 5.1c): "It moves closer to the pore center when a negative voltage is applied. The shift results from a change in permeation direction that causes Cl^- ions to accumulate either below or above R432 and the coordinating choline group."[A] In the Cl_v site, Cl^- ions are stabilized by R505 and choline groups of POPC lipids lining the pore (Figure 5.2a,c). "The position of the vestibular Cl_v peak in the permeating Cl^- distribution also depends on the electric field orientation, such that at negative voltages the effluxing anions are stabilized closer to the pore center (Figure 5.1c)."[A] This peak

shift results from the general asymmetry of the pore and orientation of the central lipid headgroup, which attracts Cl^- ions by its choline moiety at the nc site.

When Na^+ ions occupy the intracellular Na_i site, they mainly interact with D367 (Figure 5.2b,c). In turn, the attraction center at the extracellular Na_e site is formed by POPC phosphate and E313, corroborating the importance of this glutamate for ion conduction shown experimentally [50]. Notably, the vestibular Na_v site is mainly formed by the central phosphate group of POPC (Figure 5.2b), and is only present when a positive voltage is applied (Figure 5.1b). At negative voltages, the nc choline group screens the phosphate group at the pc site and prevents the Na^+ accumulation. "In conclusion, although protein residues (in particular E313 and R432) play the major role in shaping the extracellular part of the ion permeation pathway through the nhTMEM16 pore, lipid headgroups and their voltage polarity-dependent orientation strongly affect ions in the intracellular vestibule of the pore."[A]

TMEM16K

In TMEM16K, ion current is mainly mediated by Na^+ ions, as we shall discuss in more details in Chapter 6. Although we observed a few Cl^- permeation events through the TMEM16K pore, the poor statistics prevented us from quantitative analysis of Cl^- distribution along the pore. The distributions of the permeating Na^+ ions are shown in Figure 5.3a, and their trajectories are illustrated in Figure 5.3b. In total, we identified three Na^+ localization sites within the TMEM16K pore: intracellular Na_i, central Na_c[1] and extracellular Na_e (Figure 5.3a). To quantify maximum dwell time as well as contacts between ions and TMEM16K residues or lipid headgroups, we used the following bounds for the sites along the pore axis (in Å): Na_i [-20:-10], Na_c [-10:0], and Na_e [4:12]. In TMEM16K, Na^+ ions leave their localization sites faster than lipid headgroups (Table 5.2), similar to ions in the nhTMEM16 pore. However, dwelling time of lipid headgroups at their localization sites is about two times shorter in TMEM16K compared to nhTMEM16, suggesting faster exchange of the lipid headgroups between the sites during the translocation.

Analysis of the ion-protein contacts demonstrated that the network of residues stabilizing Na^+ ions within the TMEM16K pore is extended in comparison with nhTMEM16 (Figure 5.3c,d). The residues that coordinate permeating Na^+ ions include E340, D496, and E371. However, similar to nhTMEM16, ions are mainly coordinated at the extracellular mouth of the TMEM16K pore, where Na^+ ions are in contact with Y336, E340, S363, S415, and S432 (Figure 5.3c,d). At the central Na_c site, ions are stabilized by E371, N444, and D496, with the latter also forming the Na_i site (Figure 5.3c,d). "Notably, Na^+ ions are stabilized at their accumulation sites by TM3, TM4, and TM5 residues (Figure 5.3d). In contrast, lipid headgroups are mainly coordinated by TM6 residues (Figure 4.5 and Figure 4.6a)"[A], suggesting a certain level of structural separation between ion-conduction and lipid-scrambling pathways.

[1]The central Na_c in TMEM16K corresponds to the vestibular Na_v site in nhTMEM16, but is named differently due to the absence of a real vestibule in the TMEM16K cavity.

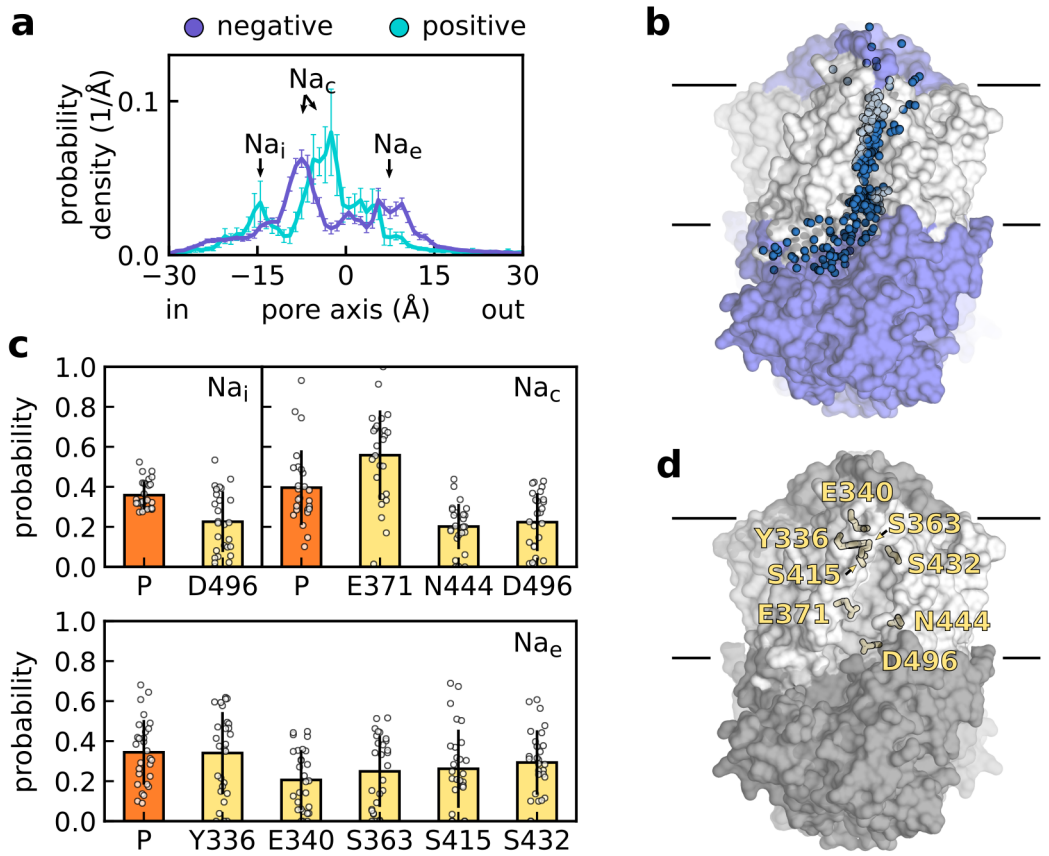

Figure 5.3: **a** Probability density distributions of permeating Na^+ ions along the TMEM16K pore at positive and negative voltages. Ion-localization sites (Na_i, Na_c, Na_e) are indicated. **b** Snapshots illustrating trajectories of permeating Na^+ ions in a representative system with TMEM16K at a negative voltage. Each blue sphere represents a particular position of a Na^+ ion in a single frame of the simulation. **c** Probability that oxygen or nitrogen atoms of hydrophilic TMEM16K residues or phosphorus or nitrogen atoms of POPC headgroups are in direct contact (distance of < 5 Å) with a permeating Na^+ ion at a particular localization site (Na_i, Na_v, Na_e) within the pore. Only residues with a contact probability of > 20 % are shown. Each data point corresponds to a single protomer. Error bars represent the standard deviation. **d** Residues indicated in **c** are mapped onto the TMEM16K subunit cavity structure. **b**, **d** The transmembrane part of the protein is shown in white, and the membrane borders are schematically depicted. The figure was partly adapted from [A].

Interestingly, all three Na^+ localization sites are partly formed by the lipid phosphate groups and demonstrate a dependence on voltage polarity (Figure 5.3c). In particular, the Na_i site is prominent only at positive voltages, when there is no adjacent choline group at the $n0$ site, and the Na_e site is formed only when a negative voltage is applied, so that there is no choline group at the $n5$ site (Figure 5.3a and Figure 4.4c). "Thus, Na^+ ions can be freely coordinated by a corresponding phosphate group at the $p1$ or $p4$ site in the absence of an interfering choline group. In turn, the Na_c site

site	Na_i	Na_c	Na_e	$p1$	$p2$	$p3$	$p4$
time (ns)	7.0	14.9	7.8	59.5	49.9	45.0	40.8

Table 5.2: Maximum dwell time of ions and lipid headgroups at the accumulation sites in the TMEM16K pore. Presented are median values calculated over all the simulated protomers.

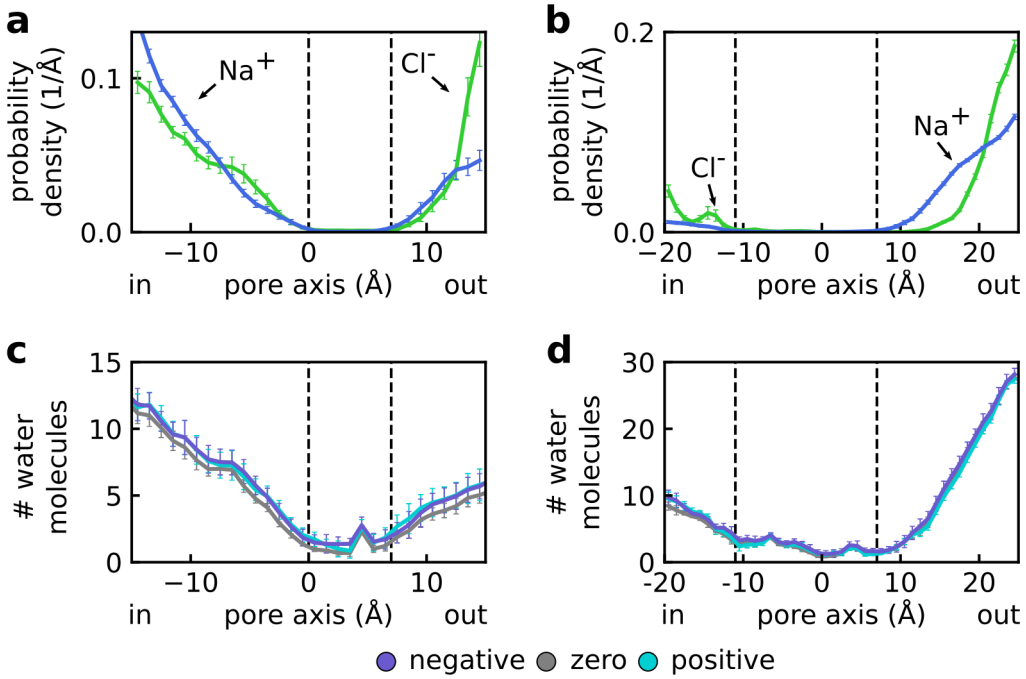

Figure 5.4: **a**,**b** Probability density distributions of blocked Cl^- and Na^+ ions along the nhTMEM16 (**a**) and TMEM16K (**b**) pores. **c**,**d** Hydration profile of the nhTMEM16 (**c**) and TMEM16K (**d**) pores, represented by the number of water molecules in 1 Å sections along the pore axis. **a–d** The neck region is indicated by dashed lines and error bars represent the standard error of mean. The figure was adapted from [A].

demonstrates a voltage polarity-dependent shift, following the location of the phosphate $p2$ site (Figure 5.3a and Figure 4.4b)."[A] Summarizing, the more structured pore of TMEM16K is characterized by a higher number of interactions between permeating ions and the subunit cavity compared to nhTMEM16, but the ion localization sites remain sensitive to the orientation of the lipid headgroups.

5.2 Permeability of the proteolipidic pore

Neck region

In our simulations, not all the ions that visited the subunit cavity eventually permeated through the pore. Figure 5.4a,b demonstrates the distributions of such blocked

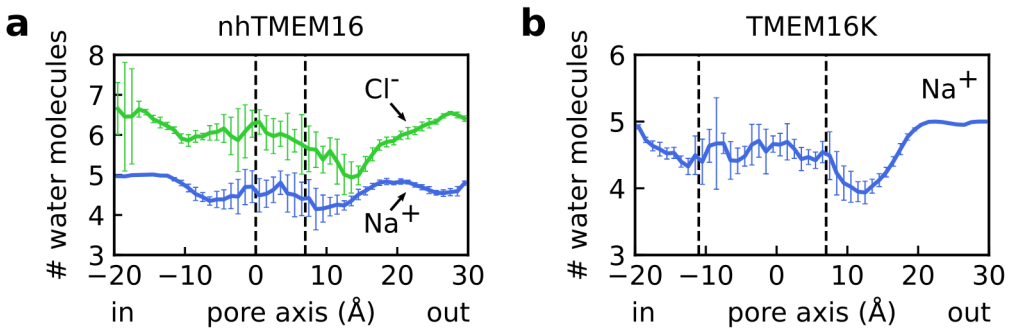

Figure 5.5: a,b Number of water molecules within the first hydration shell of Cl^- or Na^+ ions depending on the position along the nhTMEM16 (**a**) and TMEM16K (**b**) pores. Dashed lines indicate the neck region of the pores and error bars represent the standard error of mean. Average distributions over all simulated protomers are shown. The figure was adapted from [A].

ions along the pores of nhTMEM16 and TMEM16K. "In contrast to permeating ions, blocked ions show clear gaps in the distributions."[A] Therefore, "we defined the neck region as the section of the pore with a negligible probability density of blocked ions."[A] In nhTMEM16, "the neck region extends for a distance of about 7 Å from the pore center to its extracellular entrance (Figure 5.4a)."[A] In TMEM16K, the neck region includes also the intracellular part of the pore (Figure 5.4b), thereby being about 10 Å longer than the neck region of nhTMEM16.

We then calculated the hydration profile of the pore as the distribution of the number of water molecules in 1 Å sections along the pore axis (Figure 5.4c,d). Comparing the hydration profiles and distributions of blocked ions, we found that the neck region corresponds to the least hydrated part of the pore. Notably, this part coincides with the region of high sensitivity of lipid headgroups to voltage polarity in both nhTMEM16 and TMEM16K (Figure 4.3b and Figure 4.6b), indicating that the headgroups are polarity-sensitive mainly in the dehydrated region of the cavity. We then calculated number of water molecules within the first hydration shell of ions in the pore. The radius of the first hydration shell was 3.8 Å for Cl^- and 3 Å for Na^+, as found from the positions of the first minima in the radial distribution functions. Despite low hydration of the neck region, permeating ions retain their first hydration shells upon crossing it, as can be seen from Figure 5.5. This suggests that the ions bind rather loosely to the pore-forming residues and that dehydration penalty is unlikely the reason for the ion blockage.

Ion blockage

As illustrated in Figure 5.6, the ordered headgroups within the cavity line the neck region of the pore, suggesting that accessibility of the neck region to ions and, therefore, the permeability state of the pore could also be affected by lipid headgroups. "To test this, we measured the distances from headgroup moieties to the ion permeation pathway and compared these between the open (ions are permeating) and closed (ions are

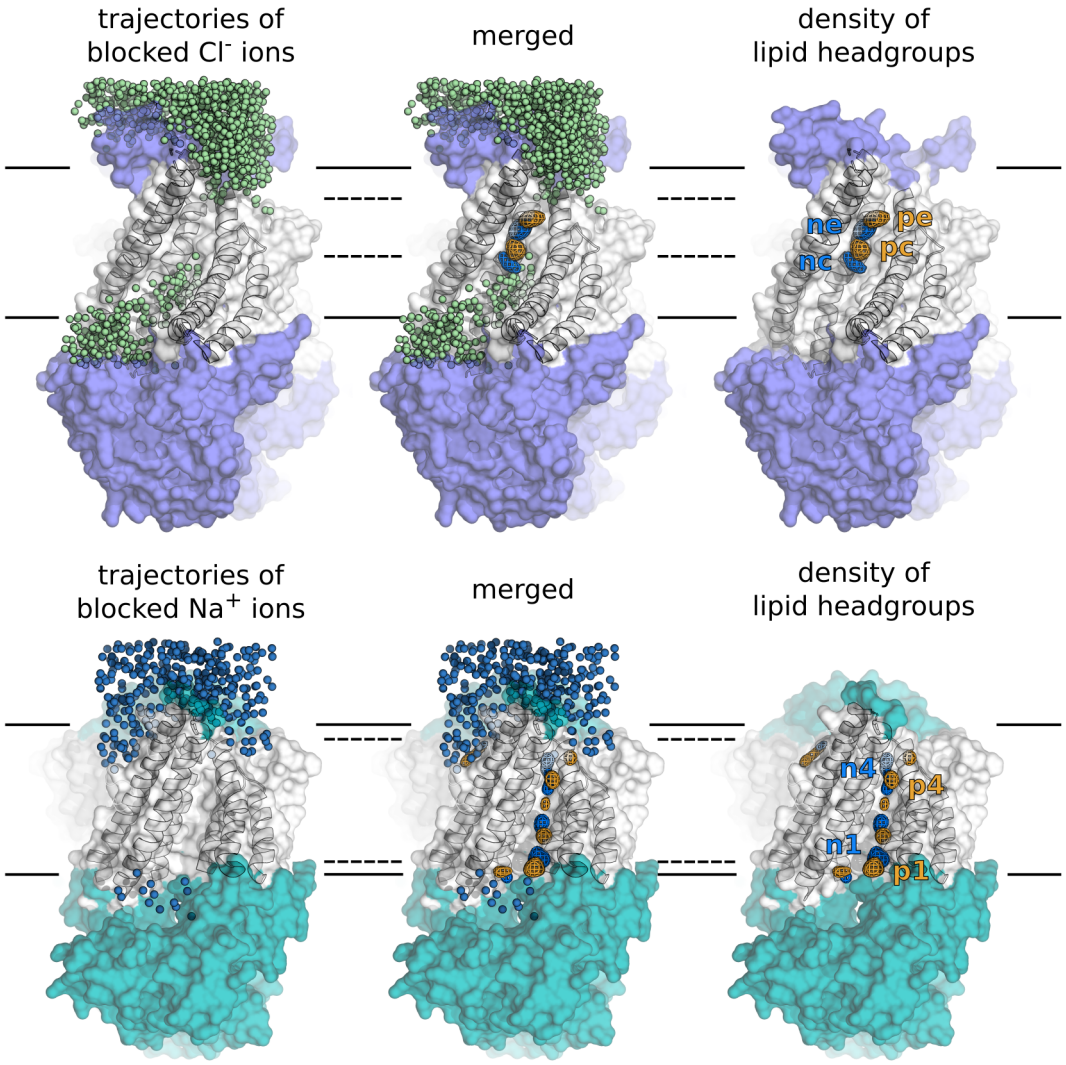

Figure 5.6: Snapshots illustrating the trajectories of blocked ions visiting the pore region together with the density of the lipid headgroups in the subunit cavity. Shown are representative systems of nhTMEM16 (top) at a negative voltage and of TMEM16K (bottom) at a positive voltage. Each sphere represents a particular position of a Cl^- (green) or Na^+ (blue) ion in a single frame of the simulation. The neck region is indicated by dashed lines. Contoured at 20σ, meshes represent the density of the phosphorus (orange) and nitrogen (blue) atoms of POPC located nearest to the pore center. The localization sites of headgroup moieties that were used in the blockage analysis (nc, pc, ne, and pe in nhTMEM16, and $p1$, $n1$, $p4$, and $n4$ in TMEM16K) are indicated. The transmembrane parts of the proteins are shown in white, and the membrane borders are schematically depicted. The figure was partly adapted from [A].

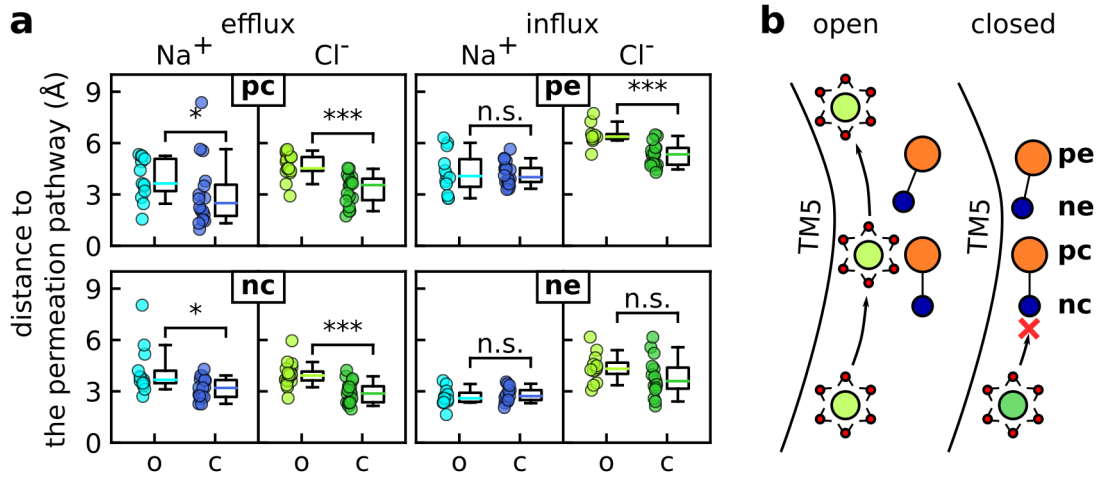

Figure 5.7: ”**a** The minimum in-plane distance between the ion permeation pathway and the nitrogen or phosphorus atoms of POPC headgroups was measured at the indicated headgroup localization sites of the open (o) and closed (c) microstates of the nhTMEM16 pore. The central (pc and nc) and extracellular (pe and ne) sites were used for the analysis of the efflux (left) and influx (right), respectively. Each data point represents a single protomer, whiskers indicate the 5th and 95th percentiles, and p-values were evaluated with the Mann-Whitney test, one-sided: $p > 0.05$ (n.s.), $p < 0.05$ (*), $p < 0.001$ (***). Number of data points and p-values (n_o, n_c, p): top row - (13, 16, 0.034), (17, 18, 0.00003), (12, 18, 0.5), (9, 17, 0.0009); and bottom row - (13, 17, 0.01), (20, 19, 0.00004), (11, 13, 0.3), (12, 15, 0.07). **b** Schematic representation of the efflux of fully hydrated (water oxygens shown in red) Cl^- ions (green) through the nhTMEM16 pore in the open state and of the blockage of permeation by lipid headgroups (orange and blue) in the central part of the pore. TM5: transmembrane domain 5.”[A] The figure was adapted from [A].

blocked) microstates[2] of the pore.”[A] More precisely, the distances were measured as follows. ”When a permeating ion was present in a region corresponding to a specific lipid localization site, its coordinates relative to the reference atom of the pore center were saved. Then the x and y components of the coordinates were averaged over all the visits in all simulations. The distance of a lipid headgroup moiety to the ion permeation pathway in the xy plane was thus defined as the distance from this average ion position. When an ion visited the part either 2.5 Å above (influx) or 2.5 Å below (efflux) the center of the region, the distance from a specific moiety to the permeation pathway was measured if the moiety was present in the region and average distances over the time of the visit were then calculated. Thus, each continuous ion visit to a region that was accompanied by the presence of a headgroup moiety in the same region resulted in one distance value. These distances were then averaged over the whole trajectory to provide a single data point for each independent protomer. This analy-

[2]To avoid confusion, here we use term ’microstate’ to describe open or closed states of the pore in the fully open ’macrostate’.

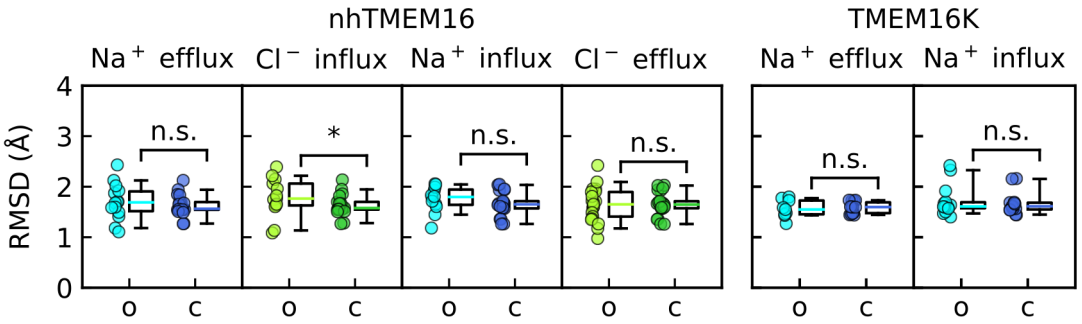

Figure 5.8: RMSD of Cα atoms of the pore-lining residues, calculated separately for the open (o) and closed (c) microstates of the nhTMEM16 and TMEM16K pores. Each data point represents a single protomer, whiskers indicate the 5th and 95th percentiles, and p-values were evaluated with the Mann-Whitney test, one-sided: $p > 0.05$ (n.s.), $p < 0.05$ (*). The number of data points and p-values (n_o, n_c, p) for each panel (left to right) were (14, 18, 0.2), (13, 18, 0.04), (12, 21, 0.1), (21, 21, 0.5), (9, 14, 0.64), and (14, 14, 0.4). The figure was partly adapted from [A].

sis was done separately for permeating and blocked ions to enable an assessment of interference between lipid headgroups and ion permeations."[A]

As entry to the neck region was sufficient for the most ions to permeate through the pore, we measured the blocking effects only of the headgroup moieties, which flanked the neck region and could potentially block ion flux. In nhTMEM16, we separately evaluated the effect of the extracellular pe and ne groups on ion influx, and the effect of the intracellular pc and nc groups on ion efflux. "When the central part of the pore was open and ion efflux was permitted, both the choline and phosphate groups of the central lipid headgroup were significantly further from the ion permeation pathway than when the pore was in the closed microstate (Figure 5.7a). The blockage is likely to be mediated by steric hindrance as, regardless of their polarity, both headgroup moieties interfere with Cl^- and Na^+ efflux."[A] The mechanism of the efflux block is schematically depicted in Figure 5.7b. "Ion influx was less affected by lipid headgroups: only the extracellular phosphate group (pe) significantly affected Cl^- influx through the pore (Figure 5.7a)."[A] The blocking effect of lipids on ion influx is less pronounced, likely because influxing ions lack the vestibule state and enter the pore directly from the bulk solution. To test if ion blockage could correlate with some conformational changes of the cavity, we calculated RMSD of the Cα atoms of the pore region separately for open and closed microstates of the pore (Figure 5.8). Notably, only blockage of Cl^- influx correlates significantly with the changes in the pore structure, whereas Cl^- efflux and Na^+ flux in either direction demonstrate no such correlation. Summarizing, in nhTMEM16 ion efflux is controlled by lipid headgroups that can sterically block access to the neck region and the ion permeation pathway, whereas ion influx is regulated by both lipids and protein conformational dynamics.

In TMEM16K, we found that the conformation of the cavity was also rather stable and did not differ between the open and closed microstates (Figure 5.8). We then measured

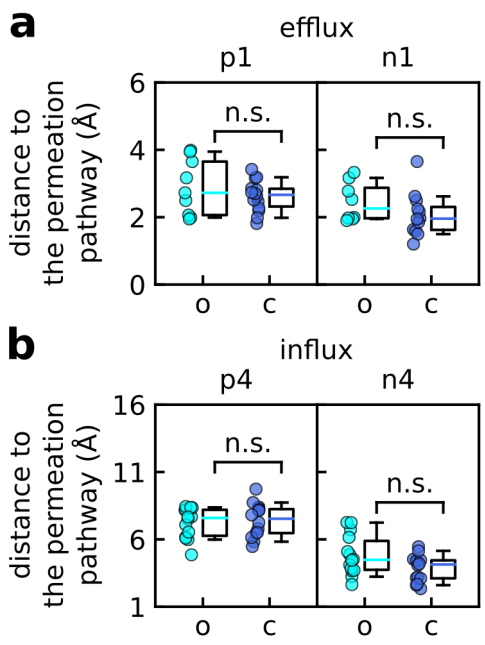

Figure 5.9: a, **b** The minimum in-plane distance between the ion permeation pathway and the nitrogen or phosphorus atoms of POPC headgroups was measured at the indicated headgroup localization sites of the open (o) and closed (c) microstates of the TMEM16K pore. The intracellular ($p1$ and $n1$) and extracellular ($p4$ and $n4$) sites were used for the analysis of the efflux (**a**) and influx (**b**), respectively. **a**,**b** Each data point represents a single protomer, whiskers indicate the 5th and 95th percentiles, and p-values were evaluated with the Mann-Whitney test, one-sided: $p > 0.05$ (n.s.). The number of data points and p-values (n_o, n_c, p) were (9, 14, 0.3), (8, 12, 0.08) in panel **a**, and (14, 14, 0.4), (14, 14, 0.5) in panel **b**. The figure was adapted from [A].

the blockage effect of the intracellular $p1$ and $n1$ groups on ion efflux (Figure 5.9a), and that of the extracellular $p4$ and $n4$ groups on ion influx (Figure 5.9b). Interestingly, we found no significant difference in distances from the headgroup moieties to the ion permeation pathway in open and closed microstates of the TMEM16K pore. Taken together with the clear spatial separation of the residues that coordinate either permeating ions or lipid headgroups, this indicates a looser coupling between lipid scrambling and ion conduction in TMEM16K compared to nhTMEM16.

5.3 Conclusions

MD simulations with atomistic resolution allowed us to analyze separately permeating and blocked ions within the pore region of TMEM16 lipid scramblases. We identified a number of dwelling sites of permeating ions along the permeation pathway and showed that ions occupy these sites for a much shorter time compared to the dwelling time of the lipid headgroups in their localization sites. Permeating ions are stabilized at the dwelling sites by the cavity-lining residues and lipid headgroups, which shape the permeation pathway in a voltage-polarity dependent manner. Notably, the network of protein interactions, which stabilizes permeating ions, is isoform-specific and is extended in TMEM16K compared to nhTMEM16. Based on the analysis of blocked ions we defined the low-hydrated neck region in the nhTMEM16 and TMEM16K pores. The neck region is lined by structured lipid headgroups, which can sterically block the ion access to the pore entrances and thereby control permeability state of the pore. Being isoform-specific, such blockage was not detected in TMEM16K, presumably because of the structural separation between ion- and lipid-coordinating residues, which provide less interdependent pathways for ion conduction and lipid translocation in TMEM16K compared to nhTMEM16.

Chapter 6

Molecular mechanisms of ion selectivity

Ion selectivity is one of the main characteristics that define physiological roles of ion channels. In contrast to bona fide Cl^- channels of the TMEM16 family, ion selectivity of TMEM16 lipid scramblases is still under debate. The existing experimental data are highly controversial, reporting TMEM16 lipid scramblases to generate anion-, cation-, or nonselective ion currents. Yet, the mechanisms behind such variation in ion selectivity are poorly understood. In this chapter, we first describe the molecular determinants of the basic ion selectivity, demonstrated by nhTMEM16 and TMEM16K in neutral POPC membranes. We then show that the ion selectivity can be affected by the arrangement of lipid headgroups within the cavity. Finally, we demonstrate that membrane lipid composition can drastically alter the ion selectivity in salt concentration-dependent manner and thereby suggest a molecular mechanism for the highly variable ion selectivity of TMEM16 lipid scramblases.

6.1 Basic ion selectivity

Structural basis

To quantify ion selectivity of the scramblases from our CompEL simulations, we used Na^+-to-Cl^- permeability ratio (P_{Na}/P_{Cl}), defined as a ratio between Na^+ and Cl^- ion conductances. We first calculated P_{Na}/P_{Cl} globally as

$$P_{Na}/P_{Cl} = \frac{\sum_i^N G_{Na}^i}{\sum_i^N G_{Cl}^i}, \tag{6.1}$$

where G_{Na}^i and G_{Cl}^i are mean Na^+ and Cl^- conductances in the i-th protomer, and the sums are over all the simulated protomers. The global permeability ratios calculated for nhTMEM16 and TMEM16K are shown in Table 6.1. Whereas nhTMEM16 demonstrated in general nonselective current in agreement with previous experimental [30]

protein	P_{Na}/P_{Cl} (global)	P_{Na}/P_{Cl}(V+)	P_{Na}/P_{Cl} (V-)
nhTMEM16	1.3	1	0.1
TMEM16K	4.3	-	4.2

Table 6.1: Ion selectivity of nhTMEM16 and TMEM16K in POPC membranes. P_{Na}/P_{Cl} was calculated globally, and separately for protomers at positive (V+) and negative (V-) voltages.

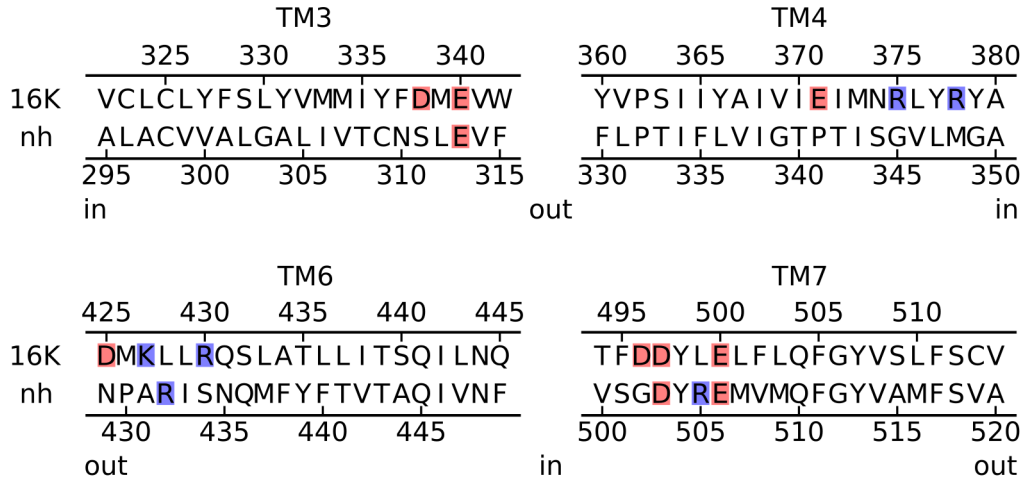

Figure 6.1: Alignment of nhTMEM16 and TMEM16K sequences for the regions forming the intracellular (TM3 and TM6) and extracellular (TM4 and TM7) entrances of the pore that contain negatively and positively charged residues highlighted in red and blue, respectively. TM: transmembrane domain. The figure was partly adapted from [A].

and computational [43] studies, TMEM16K turned out to be about four times more permeable to Na^+ than to Cl^-.

To uncover the molecular basis of the difference in ion selectivity between nhTMEM16 and TMEM16K, we scrutinized the amino acid sequences of their pore-lining regions (Figure 6.1). To this end, we used Jalview [88] and the ClustalW program [89] to do sequence alignment of nhTMEM16, afTMEM16, and all murine and human members of the TMEM16 family, excluding TMEM16H. We found that the extracellular entrance of the cavity was lined by charged residues of TM3 and TM6, whereas TM4 and TM7 adopted charged residues lining the intracellular entrance. In Chapter 5, we showed that "the conserved acidic residues, which form the Ca^{2+}-binding site (D503 and E506 in nhTMEM16, and D497 and E500 in TMEM16K), did not interact directly with permeating ions. Therefore, these residues were discarded from the consideration."[A] Compared to nhTMEM16, TMEM16K has higher number of positively charged residues in TM6 and TM4 and negatively charged residues in TM3 and TM7. Thus, the simple sequence comparison was ineffective in deriving a basis for the

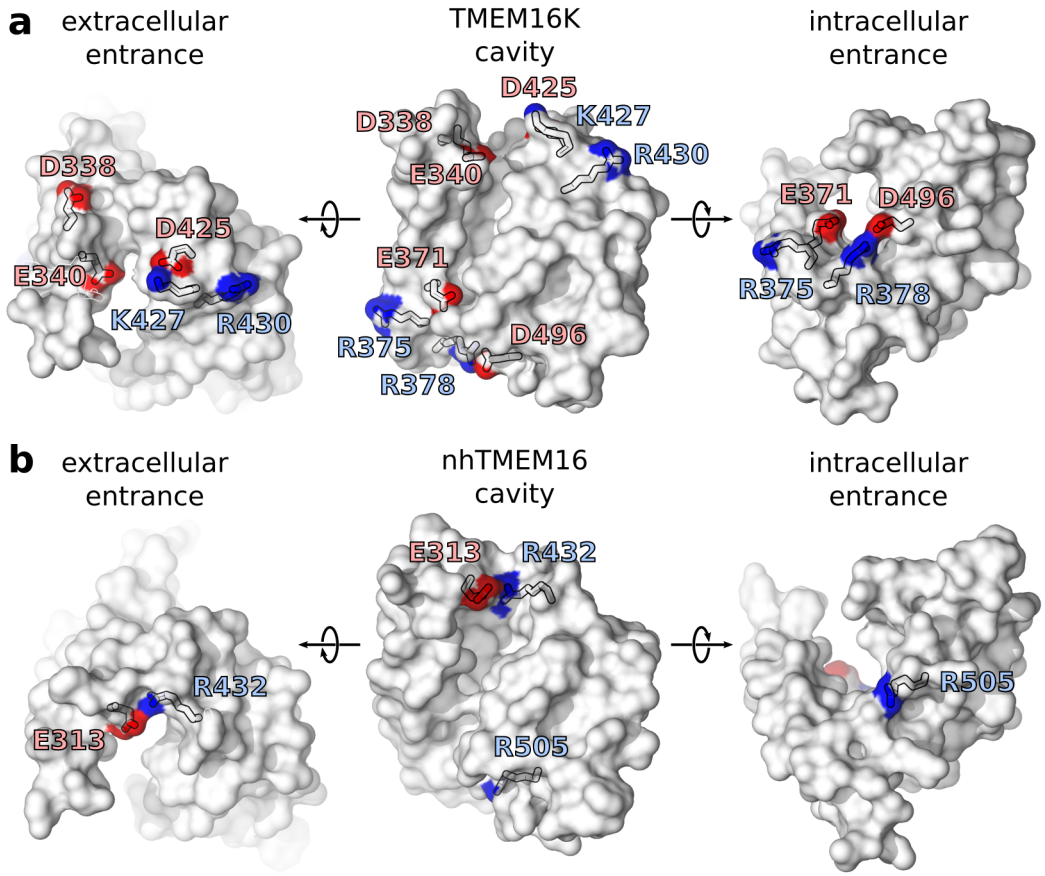

Figure 6.2: **a**, **b** Snapshots showing the distribution of charged residues (labeled) within the subunit cavities of TMEM16K (**a**) and nhTMEM16 (**b**). Oxygen and nitrogen atoms of the side chains are colored red and blue, respectively. The figure was adapted from [A].

higher Na^+ selectivity of TMEM16K. Therefore, we then mapped the charged residues on the nhTMEM16 and TMEM16K structures, to get molecular details of the distribution of the charged residues over the cavity. As can be seen from Figure 6.2, "all three charged residues of the nhTMEM16 cavity point toward the inside of the groove, while some of the TMEM16K residues (especially the basic ones) point toward the outside. In particular, the side chains of both K427 and R430 are oriented such that they cannot neutralize the negative charges of D425 and E340 that are directed toward the extracellular entrance. The same region is effectively neutral in nhTMEM16 due to the close positioning of R432 to E313. At the intracellular entrance, R505 creates an anion-attracting environment in nhTMEM16, whereas its acidic homolog D496 is effectively neutralized by R378 in TMEM16K. The human scramblase has three charged residues (R378, R375, and E371) in the pore-lining stretch of TM4, whereas nhTMEM16 contains only neutral residues in the same region. In the crystal structure, R375 points out of the cavity; however, during the simulations R375 reoriented its side chain toward the cavity interior, where it coordinated the $p1$ phosphate (Figure 4.6a) and thus could

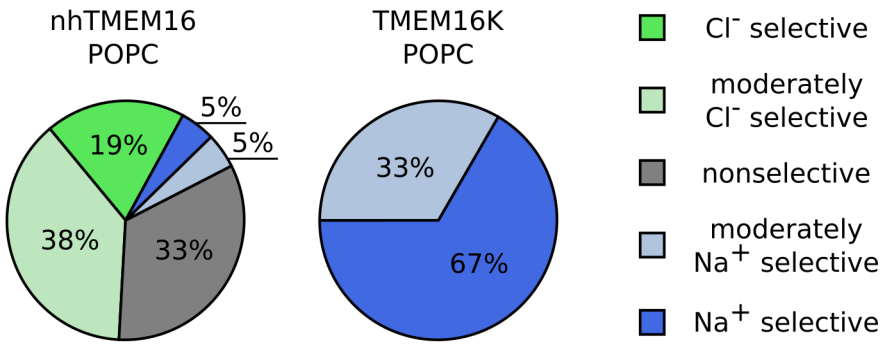

Figure 6.3: Distribution of simulated nhTMEM16 and TMEM16K protomers over the selectivity classes. Shown are the combined data collected from the simulations at positive and negative voltages. The simulations were conducted in POPC membranes. The figure was adapted from [A].

not effectively screen the negatively charged E371. Taken together, the positioning and orientation of the charged residues likely lead to the difference in pore electrostatics, resulting in the different ion selectivities of the homologs."[A]

To gain further insight into variation in ion selectivity, we calculated P_{Na}/P_{Cl} separately for each simulated protomer. To increase the robustness of the analysis, we discarded protomers with less than five ion permeation events. We note that because of the overall stochasticity of the ion permeation process and the submicrosecond time scale of the simulations, a particular protomer could demonstrate zero current mediated by one of the ion types. In particular, we observed no Cl^- permeation events in TMEM16K under negative voltages, so that P_{Na}/P_{Cl} could not be defined (Table 6.1). Therefore, to quantify variation of ion selectivity between the protomers, we sorted the protomers into five selectivity classes. "Selectivity classes were defined as follows: Na^+ selective, $P_{Na}/P_{Cl} \geq 10$; moderately Na^+ selective, $P_{Na}/P_{Cl} \in [2, 10)$; nonselective, $P_{Na}/P_{Cl} \in (0.5, 2)$; moderately Cl^- selective, $P_{Na}/P_{Cl} \in (0.1, 0.5]$, and Cl^- selective, $P_{Na}/P_{Cl} \leq 0.1$."[A] Notably, despite global P_{Na}/P_{Cl} of 1.3 makes nhTMEM16 nonselective, the protomer-wise analysis revealed that the majority of the simulated protomers demonstrated higher permeability to Cl^- than to Na^+ ions (Figure 6.3). In agreement with the overall cation selectivity of TMEM16K (Table 6.1), all simulated TMEM16K protomers were more than twice more permeable to Na^+ than to Cl^- (Figure 6.3).

Effect of voltage polarity

To see if ion selectivity of TMEM16 lipid scramblases could be sensitive to polarity of the applied voltage, we calculated P_{Na}/P_{Cl} as defined by equation 6.1 separately for protomers at positive and negative voltages (Table 6.1). Whereas TMEM16K proved to be Na^+-selective regardless of the voltage polarity, nhTMEM16 was nonselective at positive voltages but demonstrated a certain level of Cl^- selectivity at negative voltages. This was further confirmed by the analysis of ion selectivity of individual

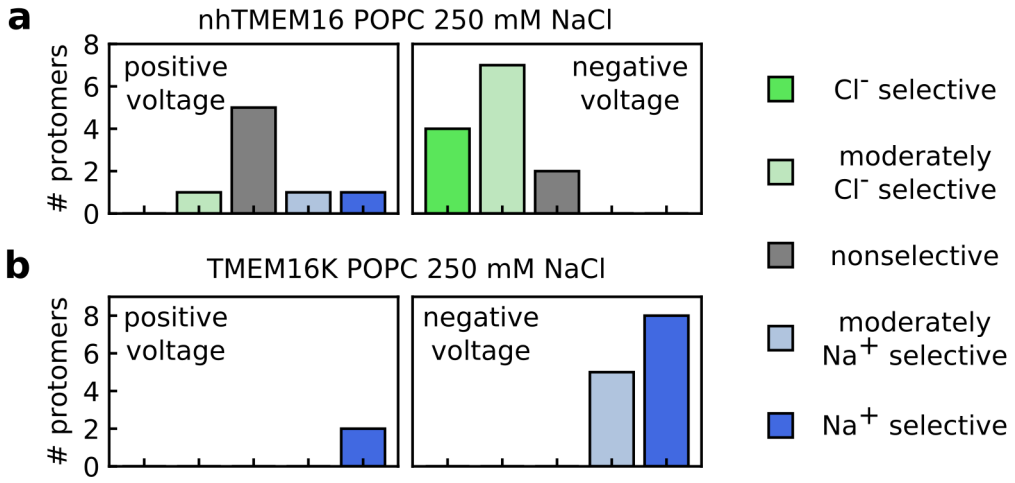

Figure 6.4: a, b Number of nhTMEM16 (**a**) and TMEM16K (**b**) protomers in each selectivity class at positive (left) and negative (right) voltages. The simulations were conducted in POPC membranes. The figure was adapted from [A].

protomers, shown in Figure 6.4. At positive voltages, the majority of nhTMEM16 protomers were nonselective, with no protomer demonstrating solid Cl^- selectivity. In contrast, nhTMEM16 protomers at negative voltages were mainly Cl^- selective. Notably, no such drastic variation in ion selectivity was observed in TMEM16K.

Structurally, the voltage polarity dependence of ion selectivity in nhTMEM16 stems from the asymmetry of its subunit cavity, in which the intracellular vestibule serves as a priming site for effluxing ions. As we have shown in Chapter 5, lipid headgroups interact with permeating ions and shape the energetics of ions along the permeation pathway. "Since differences in the energetics of the different ions define the ion selectivity of the pore, we propose that lipids may have a profound impact on ion selectivity."[A] In particular, the priming site for effluxing ions is partly formed by the central lipid headgroup, which is oriented in accordance with the polarity of the applied voltage. At positive voltages, the central lipid headgroup is upward oriented and exposes its phosphate group to the intracellular vestibule of the pore, thus creating a priming site for Na^+ and destabilizing Cl^- ions at the same time. As a result, the efflux of Na^+ is enhanced, making the nhTMEM16 pore nonselective at positive voltages.

6.2 Effect of anionic lipids

Shift in ion selectivity

All the results discussed above were obtained from the simulations in neutral POPC membranes. Given the aforementioned impact of lipid headgroups on the ion selectivity, we assumed that it could also be affected by membrane lipid composition. To test this, we conducted additional simulations of nhTMEM16 in membranes con-

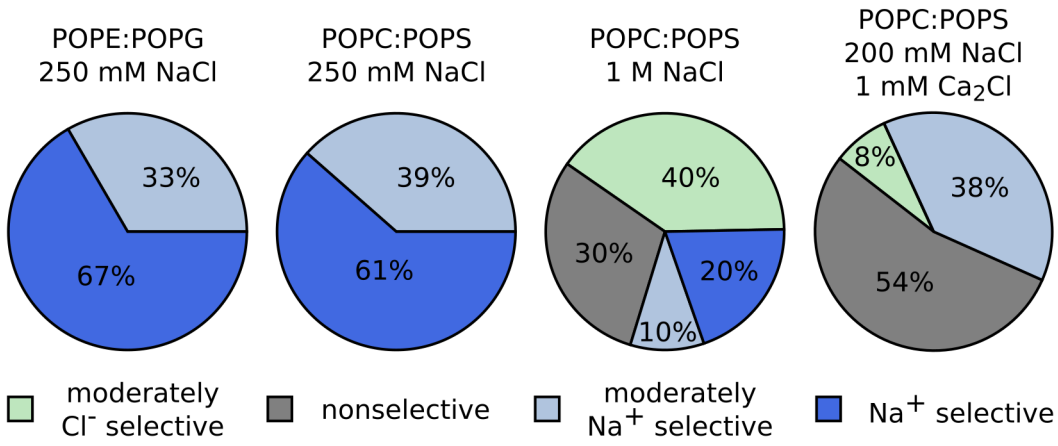

Figure 6.5: Distribution of nhTMEM16 protomers over the selectivity classes, when simulated in POPE:POPG and POPC:POPS membranes at different salt concentrations. Shown are the combined data collected from the simulations at positive and negative voltages.

membrane	[NaCl]	[Ca_2Cl]	P_{Na}/P_{Cl} (global)	P_{Na}/P_{Cl} (V+)	P_{Na}/P_{Cl} (V-)
POPE:POPG	0.25 M	0 mM	8.7	9.6	6.8
POPC:POPS	0.25 M	0 mM	14	41	6
POPC:POPS	1 M	0 mM	0.7	31	0.6
POPC:POPS	0.2 M	1 mM	1.4	1.6	1.3

Table 6.2: Ion selectivity of nhTMEM16 in anionic POPE:POPG and POPC:POPS membranes at different salt concentrations. P_{Na}/P_{Cl} was calculated globally, or separately for protomers at positive (V+) and negative (V-) voltages. Bulk concentrations of NaCl and Ca_2Cl are indicated.

taining POPE, POPG, and POPS lipids. "When we changed the lipid composition of the membrane to a 1:1 mixture of POPC and negatively charged POPS, keeping NaCl concentration of 250 mM, we observed a drastic change in ion selectivity, such that the proteolipidic pore of fully open nhTMEM16 became effectively Na^+ selective (Figure 6.5; Table 6.2). Notably, the same effect was evident in a 3:1 mixture of neutral POPE and negatively charged POPG (Figure 6.5; Table 6.2)."[A] Despite similar distribution of the protomers over the selectivity classes (Figure 6.5), Na^+ selectivity was more prominent for nhTMEM16 in POPC:POPS membrane than in POPE:POPG membrane with P_{Na}/P_{Cl} of 14 and 8.7, respectively (Table 6.2). This indicates that higher concentration of anionic lipids in a membrane leads to a stronger preference for Na^+ in ion conduction by nhTMEM16. Notably, the effect of the voltage polarity is also evident in anionic membranes, so that the nhTMEM16 pore is more Na^+ selective at positive voltages (Table 6.2).

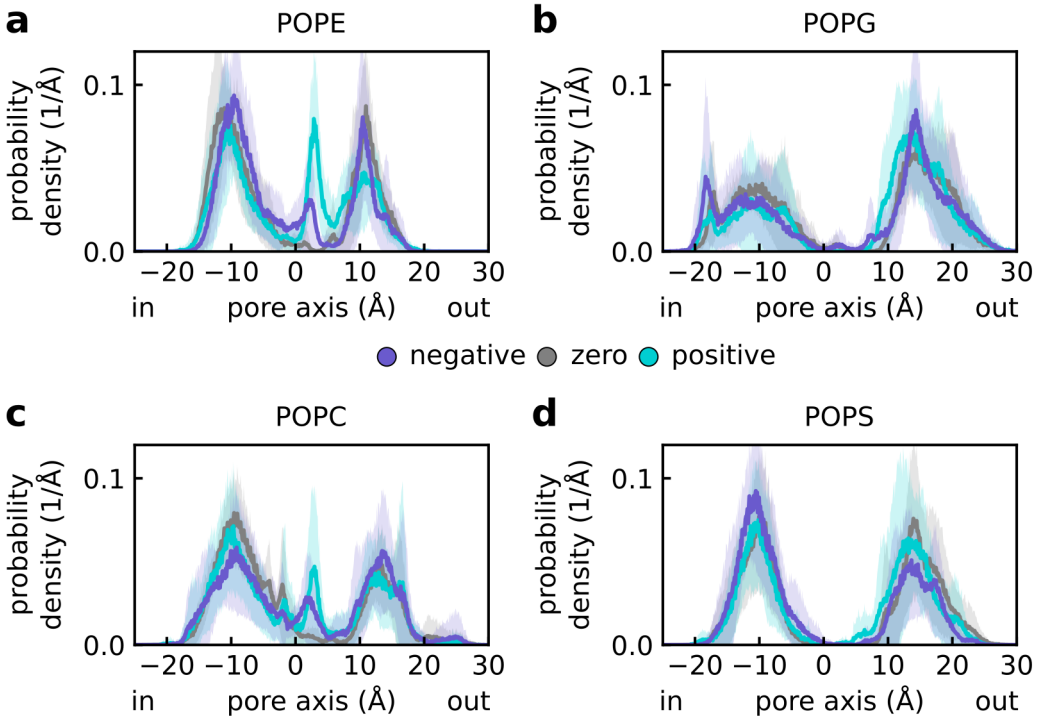

Figure 6.6: a–d Distributions of phosphorus atoms of POPE (**a**), POPG (**b**), POPC (**c**), and POPS (**d**) along the nhTMEM16 subunit cavity in either POPE:POPG or POPC:POPS membrane in 250 mM NaCl at negative, zero, and positive voltages. Distributions were averaged over all simulated protomers and shaded areas represent the standard error of mean. The figure was adapted from [A].

"Despite the drastic change in the ion selectivity, the general ion-conduction mechanism of nhTMEM16 in anionic membranes remained similar to that in the pure POPC membrane."[A] In particular, the ion-permeation pathway was lined by lipid headgroups, as can be seen from distribution of lipid phosphate groups along the nhTMEM16 cavity (Figure 6.6). "Notably, unlike the POPC and POPE headgroups in the mixed membranes, which have a localization pattern similar to that of the pure POPC membrane, the headgroups of anionic lipids rarely visited the central part of the pore (Figure 6.6). Such depletion suggests slower kinetics of scrambling for phosphatidylserine compared with phosphatidylethanolamine lipids, in full agreement with experimental observations [23]."[A] The exclusion of anionic lipids from the central region of the pore indicates that their effect on ion selectivity mainly results from changing the membrane charge at the entrances of the pore.

Salt-induced reversal of the selectivity change

Since high salt concentrations can effectively screen membrane surface charge [90], we then tested if such screening could affect ion selectivity of nhTMEM16 in an anionic membrane. "When we increased the NaCl concentration from 250 mM to 1 M, the ion

selectivity of nhTMEM16 embedded in POPC:POPS membrane reversed to partially restored preference for Cl^- (Figure 6.5, Table 6.2). The increased salt concentration seems to result in ion selectivity that is intermediate between those of neutral and anionic membranes at the lower salt concentration. Thus, as the protein demonstrates nonselective current at positive voltages in the POPC membrane, its ion selectivity is shifted towards Na^+ in the POPC:POPS membrane even at the higher salt concentration (Table 6.2)."[A] We then tested if divalent Ca^{2+} ions reverse the ion-selectivity change as well. Since Ca^{2+} ions screen the surface charge of anionic membranes more efficiently than Na^+ [91], we reduced NaCl concentration to 200 mM and added Ca^{2+} ions to the solution to reach bulk concentration of $\sim$1 mM. At these conditions, the majority of the simulated nhTMEM16 protomers demonstrated nonselective current (Figure 6.5) with overall P_{Na}/P_{Cl} of 1.4 (Table 6.2). Note that nhTMEM16 in the pure POPC membrane and 250 mM NaCl solution had P_{Na}/P_{Cl} of 1.3 (Table 6.1). Interestingly, the screening effect of Ca^{2+} was especially pronounced at positive voltages, making nhTMEM16 as nonselective as at negative voltages (Table 6.2). Recently, similar salt-induced effects on ion selectivity have been shown in experiments on TMEM16F [41]. Various types of cations were used and the prominence of the effect grew with the valency of a cation, so that di- and trivalent cations switched TMEM16F from the cation- to anion-selective state [41].

6.3 Conclusions

In this chapter, we investigated the molecular mechanisms of ion selectivity in nhTMEM16 and TMEM16K. We found that TMEM16K demonstrates clear cation selectivity in contrast to the generally nonselective nhTMEM16. We unraveled the molecular basis for the difference in ion selectivity between the homologs, which relates both to the positioning and to the orientation of charged residues within the subunit cavity. We also demonstrated that ion selectivity depends on voltage polarity. In particular, the scramblases are more Na^+ selective at positive voltages owing to the pore asymmetry and polarity-dependent orientation of lipid headgroups within the cavity. Furthermore, we found that anionic lipids can drastically change ion selectivity of TMEM16 lipid scramblases by bringing negative charge to the cavity entrances. Finally, we showed that this selectivity change is sensitive to the concentration of salt in the solution because of the screening of the membrane charge by mono- and divalent cations. Thus, our results are in full agreement with the recent experimental observations, and augment them with a mechanistic explanation, pointing at lipids as an important modulator of ion selectivity in TMEM16 lipid scramblases.

Chapter 7

Electrostatics within the proteolipidic pore

Electrostatics often plays the main role in ion selectivity of ion channels by shaping the energetics of their interaction with ions. Both the channel and its environment contribute to the charge distribution and, thereby, to the electrostatic potential of a system. However, experimentally resolved structures rarely provide information on the membrane and water solution, which together form the surroundings of ion channels. In particular, no detailed information is available on the arrangement of lipid headgroups within the subunit cavities of TMEM16 lipid scramblases from the structural experiments. As was shown in Chapter 4, such information can be obtained from atomistic MD simulations. However, a tool that could robustly quantify biomolecular electrostatics based on MD trajectories was missing. To fill this gap, we developed g_elpot, a tool that takes advantage of water molecules explicitly present in the simulations to reliably calculate distribution of the electrostatic potential in a simulated system. In this chapter, we first expound the theoretical basis and implementation details of g_elpot, and then demonstrate how our tool can be used to gain high-resolution insights into ion-channel electrostatics. In particular, by applying g_elpot to our simulations of TMEM16 lipid scramblases, we could quantify and compare the effects of membrane lipid composition and protein mutations on the electrostatics within the pores of nhTMEM16 and TMEM16K.

7.1 Computing biomolecular electrostatics

"In the absence of detailed structural information on a biomolecular environment, the distribution of the electrostatic potential around a biomolecule can be evaluated by continuum methods based on the Poisson–Boltzmann (PB) equation [92]. Numerous insights into the biophysical properties of proteins and nucleic acids have been gained using continuum methods [92] implemented in a number of software packages, including the widely used DelPhi [93] and APBS [94, 95]. However, due to

their implicit representation of the biomolecular environment, continuum methods do not take into account a number of molecular-level phenomena (e.g. the orientation of solvent molecules at the interface with biomolecules [96] and the orientation of lipid headgroups around membrane proteins), which can significantly affect the electrostatics of the system [97]. Moreover, PB methods represent the environment in terms of electric permittivity, which is arbitrarily assigned to different parts of the system [98, 99]. Lastly, calculations based on the PB equation ignore the natural dynamics of the studied biomolecules. These features limit the amount of quantitative details on biomolecular electrostatics that can be obtained using PB methods.

Nowadays, MD simulations are commonly used to obtain information on the dynamics and functions of biomolecular systems at atomistic resolution [63, 100]. During an MD simulation, the biomolecule and its environment sample the conformational space, with each trajectory frame containing information on the instantaneous distribution of electrostatic potential, as defined by the atomic positions. Due to the nanoscale size of the systems studied in MD simulations, periodic boundary conditions are commonly used to avoid undesirable edge effects [99, 101]. In a periodic system, the long-range nature of the electrostatics makes the direct sum of contributions from the periodic copies only conditionally convergent [99]. This problem can be tackled by a number of approaches [99, 101], including widely used methods based on the Ewald summation [77, 102]. Briefly, the potential is split into short- and long-range parts that converge in real and Fourier spaces, respectively. Whereas the short-range part has singularities at the atom positions, the long-range part can be used to calculate a smooth distribution of the electrostatic potential over the simulation box.

The idea of using the long-range part of the potential (calculated by the smooth particle mesh Ewald (SPME) method [77]) to characterize electrostatics in biomolecular systems based on the MD trajectories was first realized in the *pmepot* plug-in [103] of the Visual Molecular Dynamics (VMD) package [104]. The plug-in generates a map of the average distribution of the long-range part of the SPME potential and, to the best of our knowledge, has been so far the only tool for extracting electrostatic potentials from MD trajectories. However, the resulting map can be substantially smeared due to the free translation and rotation of a biomolecule during an MD simulation. This smearing cannot be avoided by rotational fitting of the trajectory onto the reference structure prior to the SPME calculation because subsequent application of the periodic boundary conditions results in an artificial electrostatic-potential map. The smearing problem can be solved by using short MD trajectories [105] or simulations with positional restraints applied to the biomolecule [106]. However, the absence of a fitting procedure limits the usage of *pmepot* mainly to the qualitative analysis of electrostatics in long MD simulations of free proteins and nucleic acids. Additionally, although MD trajectories inherently contain time-resolved information on a biomolecular system, *pmepot* can only derive the average distribution of the potential and not its time course. Furthermore, we will demonstrate that direct quantification of electrostatics from the long-range part of the SPME potential should be interpreted with caution due to its slow convergence over the parameters used for the calculations."[B]

7.2 g_elpot

"Here we present the g_elpot tool, which overcomes the aforementioned limitations and enables the efficient quantitative analysis of electrostatic potential in biomolecular systems based on MD trajectories. On-the-fly fitting of trajectory frames enables the generation of high-resolution maps of electrostatic potential around biomolecules. Based on a computational scheme that harnesses the explicit water molecules present in an MD system, g_elpot generates the maps that are easily converted into convergent electrostatic-potential profiles."[B]

Theory

"To decide whether it is electrostatically favorable for a charged solvable substance to locate at particular sites on a biomolecule, we consider the potential (Φ) created at a point ($\mathbf{r}$) of a system with respect to the bulk solution

$$\Phi(\mathbf{r}) = \phi^{local}(\mathbf{r}) - \phi^{bulk}. \tag{7.1}$$

Here we only consider the hydrated regions of the system because, in most biologically relevant processes, a charged soluble substance interacts with a biomolecule at a hydrated site. The local electrostatics at the water-populated regions of the system can be quantified by water-molecule potentials that are calculated at a certain point ($\mathbf{r}_{wm}$) within each water molecule, e.g. its center of geometry. The water-molecule potential can be then split into two parts

$$\phi^{local}(\mathbf{r}_{wm}) = \phi_{wm}(\mathbf{r}_{wm}) + \phi_{sur}(\mathbf{r}_{wm}), \tag{7.2}$$

where $\phi_{wm}(\mathbf{r}_{wm})$ accounts for the contribution of the water molecule itself to the potential and $\phi_{sur}(\mathbf{r}_{wm})$ is the contribution of the rest of the system, i.e. the surroundings of the water molecule. In turn, we define the system bulk potential as

$$\phi^{bulk} =< \phi_{wm} >_{bulk} + < \phi_{sur} >_{bulk}, \tag{7.3}$$

where $< \cdots >_{bulk}$ denotes averaging over all water molecules in the bulk region of the system. Thus,

$$\Phi(\mathbf{r}_{wm}) = \phi_{wm}(\mathbf{r}_{wm}) + \phi_{sur}(\mathbf{r}_{wm}) - < \phi_{wm} >_{bulk} - < \phi_{sur} >_{bulk} . \tag{7.4}$$

Contribution of the water molecule to the potential at $\mathbf{r}_{wm}$ depends on geometry of the water molecule but not on its position or surroundings. Therefore, if water molecules are assumed to have only small geometric fluctuations,

$$\phi_{wm}(\mathbf{r}_{wm}) \approx < \phi_{wm} >_{bulk} \tag{7.5}$$

and

$$\Phi(\mathbf{r}_{wm}) \approx \phi_{sur}(\mathbf{r}_{wm}) - < \phi_{sur} >_{bulk} . \tag{7.6}$$

Notably, in case of absolutely rigid water molecules, the approximations in Eqs. 7.5 and 7.6 become equalities."[B]

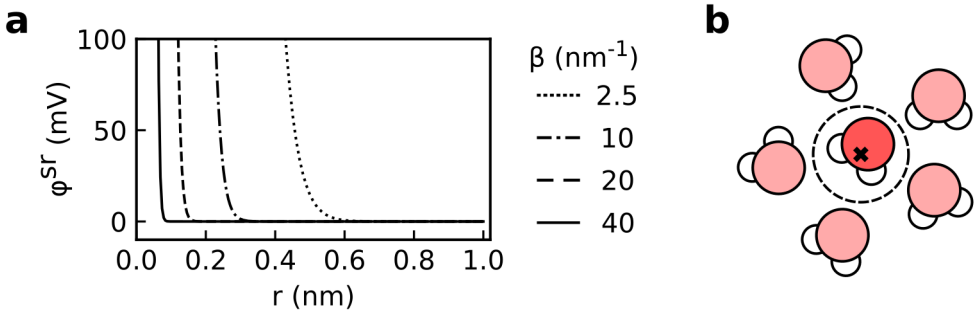

Figure 7.1: **a** "Dependence of the short-range part of the electrostatic potential on the distance from the source atom is shown for different β values."[B] **b** Schematic showing exclusion volume of a water molecule. Because of the interatomic repulsion, each water molecule has an exclusion volume (enclosed by dashed line), where no atoms of other molecules can enter, justifying omission of the short-range part of the potential. The water-molecule center of geometry is indicated by the cross. The figure was partly adapted from [B].

"In a periodic point-charge system where the unit-cell edges are defined by vectors $\mathbf{a}_1$, $\mathbf{a}_2$, and $\mathbf{a}_3$, the distribution of electrostatic potential can be calculated with the SPME method [77] by splitting the potential into the long-range and short-range parts

$$\phi(\mathbf{r}) = \phi^{lr}(\mathbf{r}) + \phi^{sr}(\mathbf{r}), \tag{7.7}$$

where the long-range part is created by Gaussian-distributed charges $\rho(\mathbf{r})$, approximating the original charge distribution

$$\rho(\mathbf{r}) = \sum_{\mathbf{n}} \left(\frac{\beta}{\sqrt{\pi}}\right)^3 \sum_{i=1}^{N} q_i \exp(-\beta^2 |\mathbf{r} - \mathbf{r}_i + \mathbf{n}|^2), \tag{7.8}$$

where N is number of atoms, q_i and $\mathbf{r}_i$ are the charge and position of an atom i, β is the inverse width of a Gaussian, and the outer sum is over $\mathbf{n} = n_1\mathbf{a}_1 + n_2\mathbf{a}_2 + n_3\mathbf{a}_3$, for all integers n_1, n_2, n_3. The long- and short-range parts of the potential converge in Fourier and real space, respectively. The higher the value of β, the faster the short-range part decays (Figure 7.1a); therefore the value of the β parameter can be chosen such that the short-range part of the potential created by an atom is negligible at a predefined distance. In MD simulations, interatomic repulsion at short distances prevents atoms from overlapping and guarantees a nonzero distance between them (Figure 7.1b). Therefore, the short-range part of the potential created at $\mathbf{r}_{wm}$ by the atoms surrounding the water molecule can be made negligible by assigning β a value greater than some critical value β_c, so

$$\phi_{sur}(\mathbf{r}_{wm}) = \phi^{lr}_{sur}(\mathbf{r}_{wm}) + \phi^{sr}_{sur}(\mathbf{r}_{wm}) \approx \phi^{lr}_{sur}(\mathbf{r}_{wm}), \tag{7.9}$$

and Φ can be found as

$$\Phi(\mathbf{r}_{wm}) \approx \phi^{lr}_{sur}(\mathbf{r}_{wm}) - < \phi^{lr}_{sur} >_{bulk} . \tag{7.10}$$

Thus, the proper choice of β ensures that only the long-range part of the potential is enough to obtain a rigorous quantification of local electrostatics in the hydrated regions of the simulation system."[B]

In a periodic system, charges distributed according to Eq. 7.8 "create an electrostatic potential

$$\phi^{lr}(\mathbf{r}) = \frac{1}{V\epsilon_0} \sum_{\mathbf{k}\neq 0} \frac{\exp\left(-\frac{\mathbf{k}^2}{4\beta^2}\right)}{\mathbf{k}^2} \exp(i\mathbf{kr}) \sum_{i=1}^{N} q_i \exp(-i\mathbf{kr}_i), \tag{7.11}$$

where ϵ_0 is the permittivity of vacuum, V is the volume of the unit cell, β is the inverse width of the Gaussian, N is number of atoms, q_i is a charge and $\mathbf{r}_i$ is a position of an atom i. The outer sum is over vectors $\mathbf{k} = 2\pi k_1\mathbf{a}_1^* + 2\pi k_2\mathbf{a}_2^* + 2\pi k_3\mathbf{a}_3^*$ for all integers k_1, k_2, and k_3 excluding $\{0, 0, 0\}$, where $\mathbf{a}_j^*$ is a reciprocal vector defined by $\mathbf{a}_j^*\mathbf{a}_l = \delta_{jl}$, and δ_{jl} is the Kronecker delta. The rightmost sum defines the structure factor of the system. Following the SPME method [77], the structure factor can be approximated by $\tilde{S}$ which is calculated on a grid using cardinal B-spline interpolation of the charge and fast Fourier transform. The long-range part of the SPME potential $\phi^{lr}_{SPME}(\mathbf{r})$ on the grid can be then obtained by inverse Fast Fourier transform:

$$\phi^{lr}_{SPME}(\mathbf{r}) = \frac{1}{\epsilon_0} FFT^{-1}\left(\frac{\exp\left(-\frac{\mathbf{k}^2}{4\beta^2}\right)}{\mathbf{k}^2}\tilde{S}(\mathbf{k})\right). \tag{7.12}$$

It is this potential that is used by g_elpot to calculate and assign a potential value to water molecules."[B]

Implementation

"g_elpot exploits the presence of explicit water molecules in MD simulations to generate detailed information on the electrostatics in a biomolecular system. First, the long-range part of the SPME potential is calculated on a regular grid (Figure 7.2, step 1), and then each water molecule is assigned a potential, referred to as water-molecule potential (Figure 7.2, step 2). This potential is the average of the long-range SPME potentials at the grid nodes within a sphere of 0.15-nm radius around the center of geometry of the water molecule. The averaging smoothens the resulting potentials by suppressing changes in the potential caused by minor changes in the water-molecule geometry. Thus, provided that $\beta \geq \beta_c$, the water-molecule potential reports on the electrostatic potential created by the water-molecule's surroundings. To avoid smearing of the final electrostatic-potential map (which is built around a biomolecule), the trajectory frame is superimposed on the reference structure of the biomolecule (Figure 7.2, step 3). Each water-molecule potential is then added to the map nodes that are within 0.15 nm of the water-molecule's center of geometry. After all water-molecule potentials are added to the final electrostatic-potential map, the potential at each node is normalized by the number of contributing water molecules (Figure 7.2, step 4). This procedure is repeated for each frame of the trajectory, resulting in an average electrostatic-potential map around the biomolecule. g_elpot also generates a map that reports the fraction

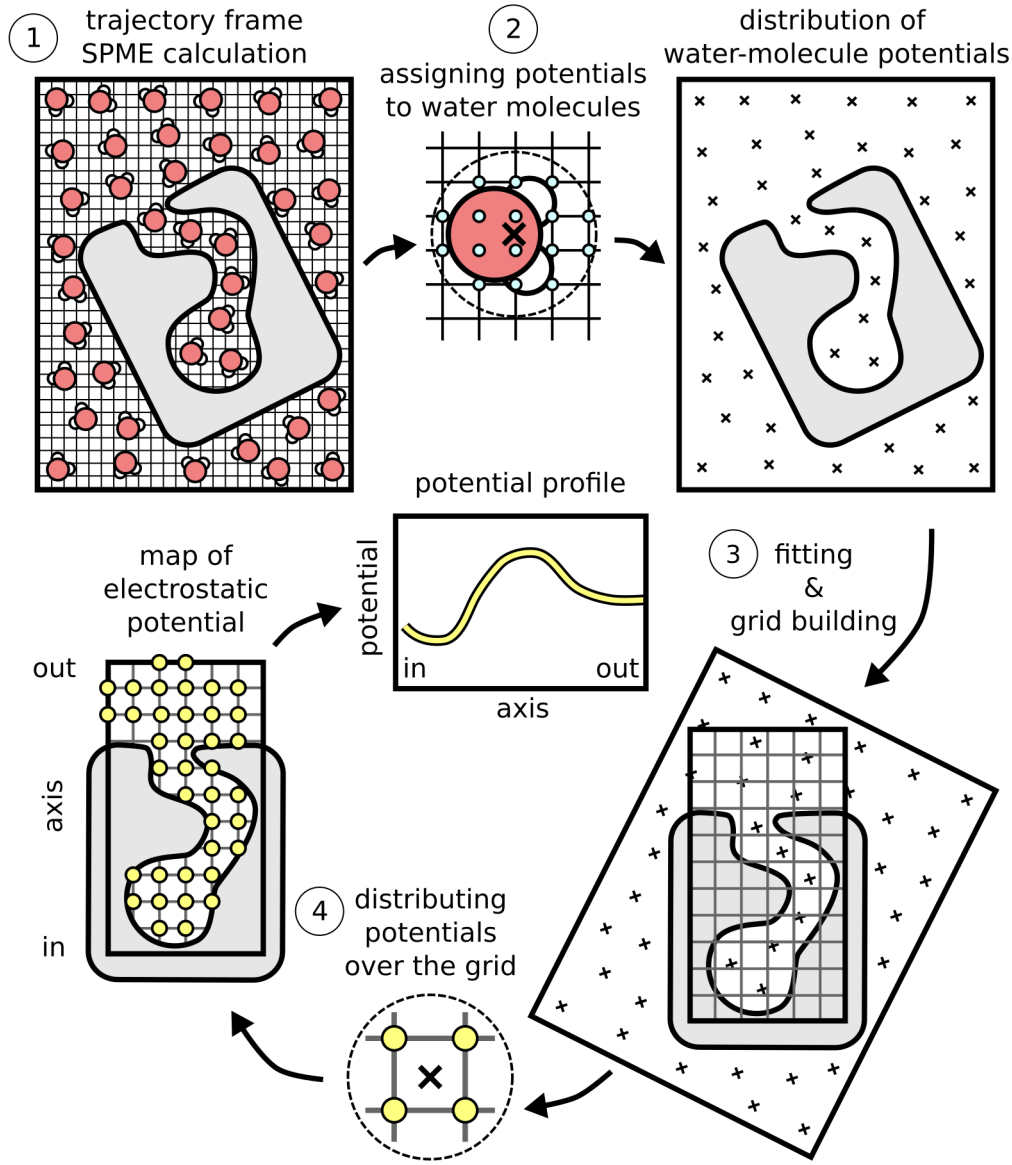

Figure 7.2: "Water-based scheme to calculate the electrostatic potential. First, the long-range part of the potential is calculated by solving the Poisson equation on the grid using the SPME method. Second, each water molecule is assigned a potential averaged over a sphere around its center of geometry, resulting in a distribution of water-molecule potentials. Third, the frame is fitted onto the reference structure and the grid of the final electrostatic-potential map is built around the biomolecule. Fourth, the water-molecule potentials are distributed over the nodes of the electrostatic-potential map, followed by normalization of the node potential based on the number of contributing water molecules. The final map is used for the quantitative analysis of electrostatics, e.g. to generate a potential profile."[B] The figure was adapted from [B].

of trajectory frames in which a particular node has water molecules in its vicinity. Since this map is used to mask the dehydrated regions of a system, it is referred to as water-occupancy map. As the water-occupancy map has the same dimensions as the electrostatic-potential map, combining both maps is a straightforward way to obtain the electrostatic-potential profile along a coordinate of interest, for instance along the pore axis of an ion channel. Optionally, the water-molecule-based scheme can be switched off so that the final map is obtained by linear interpolation of the SPME potential instead of the average water-molecule potential. When calculated in this way, the electrostatic-potential map can be used to qualitatively describe the distribution of the electrostatic potential in nonhydrated regions of the system."[B]

"g_elpot is written in C/C++, with fast Fourier transform as part of the SPME calculation done using FFTW library [107] version 3. OpenMP is used for optional thread parallelization over the trajectory frames. The tool is GROMACS based and, therefore, takes input files in GROMACS formats. In particular, the atomic charges and reference conformation are read from a *tpr* file, and the trajectory can be in any GROMACS-supported format (including *xtc*, *tng*, *trr*, and *pdb*). The atomic groups used for the analysis are defined by the GROMACS-style index file."[B]

The source code of g_elpot is available at:
https://jugit.fz-juelich.de/computational-neurophysiology/g_elpot

7.3 TMEM16 pore electrostatics

TMEM16K

To quantify electrostatics in the subunit cavity of TMEM16 lipid scramblases, we used our single-bilayer simulations in which no transmembrane voltage was applied. We first used g_elpot to analyze the first 100 ns of a TMEM16K trajectory. "We generated electrostatic-potential and water-occupancy maps around the whole protein and then separated the regions corresponding to the different protomers to calculate their electrostatic-potential profiles (Figure 7.3a). In the fully active state, the scramblase cavity is bound to two Ca^{2+} ions, which were partly hydrated in the simulations. Since the activating Ca^{2+} do not directly interact with the permeating ions, we also excluded from the analysis the regions in direct proximity to the Ca^{2+} ions (distance of < 5 Å)."[B] Finally, we masked the regions with a low water presence (< 10 % of frames). Figure 7.3a illustrates the resulting electrostatic-potential and the masked water-occupancy maps. We then calculated the electrostatic-potential profile along the TMEM16K pore by averaging the potential map over the plane perpendicular to the pore axis (Figure 7.3b). The resulting profile was strongly dependent on the value of the β parameter used in the g_elpot calculations. Notably, in case of $\beta < 5$ nm^{-1}, the potential was positive within the pore, contradicting cation selectivity of TMEM16K. However, the higher β values led to more negative potentials, with the profiles converging at $\beta \geq 20$ nm^{-1}. To demonstrate advantage of the water-based scheme to quantify electrostatics in the pore, we also calculated the potential profiles using the

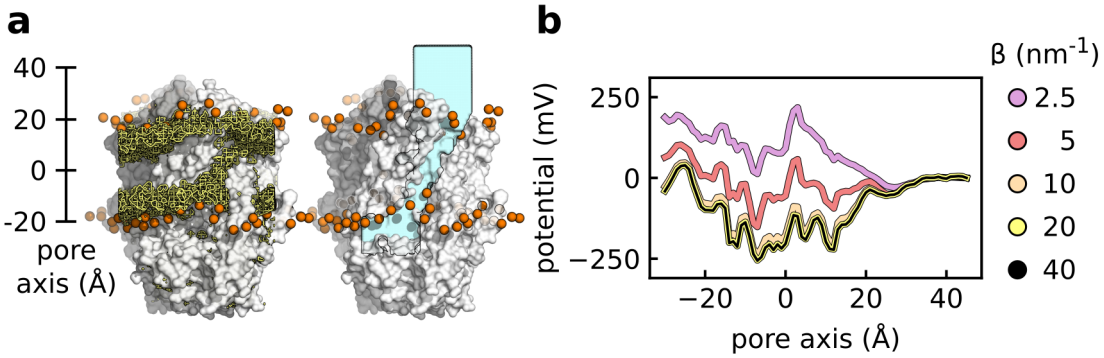

Figure 7.3: **a** Example of the electrostatic-potential map (yellow) and the masked water-occupancy map (cyan) that were used to calculate the electrostatic-potential profiles in TMEM16K. The water-occupancy map was contoured at an occupancy level of 0.1. The electrostatic-potential map was calculated with $\beta = 20$ nm^{-1} and contoured at -200 mV. The protein and phosphorus atoms of POPC are shown in white and orange, respectively. **b** Electrostatic-potential profiles along the TMEM16K pore, calculated by applying g_elpot to the first 100 ns block of the 1 μs long trajectory using different values for the β parameter.

raw long-range SPME potential combined with a water density map produced using GROmaρs [108] (Figure 7.4a). Similar to the g_elpot results, the pore potential was positive at low β values and decreased upon increasing β.

We then tested convergence of each approach over β parameter by comparing the profiles ($\Phi(z)$) at different β values with the reference profile ($\Phi_{ref}(z)$) at $\beta = 40$ nm^{-1}. To quantify the difference between the profiles, we used the root mean square difference ($\mathrm{RMS_{Diff}}$) defined as

$$\mathrm{RMS_{Diff}} = \left(\frac{1}{N} \sum_{i}^{N} (\Phi(z_i) - \Phi_{ref}(z_i))^2 \right)^{\frac{1}{2}}, \tag{7.13}$$

where z_i is the i-th position along the pore axis, and the sum is taken over all the points in the profile. As can be seen from Figure 7.4b, the raw-SPME profiles demonstrated poorer convergence over β compared with those calculated using water-based potentials with g_elpot. "A possible explanation for this is that during the trajectory protein and lipid atoms overlap with the average water-density map and, therefore, contribute to the resulting potential profiles. However, due to difference in the configuration between water and nonwater molecules, the β parameter affects their internal potentials differently, leading to the poorer convergence. Since $\beta = 20$ nm^{-1} provided convergent results, we used this value to calculate the average potential profile along the TMEM16K pore from the whole 1 μs trajectory."[B] Consistent with the cation selectivity of the TMEM16K scramblase, the pore in its whole length was characterized by the negative electrostatic potential (Figure 7.5).

In Chapter 6, we identified charged residues which line the cavity of TMEM16K and

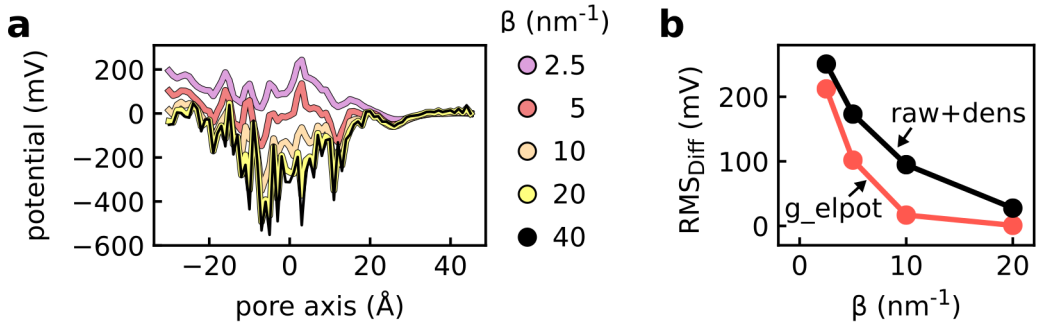

Figure 7.4: a The electrostatic-potential profiles along the TMEM16K pore, calculated based on the raw-SPME potential and the water-density map, are shown for different β values. The water density was normalized to the average and a threshold of 0.5σ was used to define the hydrated region of the pore. The profiles were calculated from the first 100 ns block of the 1 μs TMEM16K trajectory. **b** Root mean square difference ($\mathrm{RMS_{Diff}}$) of the potential profiles along the TMEM16K pore calculated at different β values with respect to the one calculated at $\beta = 40$. The electrostatic potential was calculated by either *g_elpot* (red) or using the raw-SPME potential combined with the water-density map (raw+dens; black).

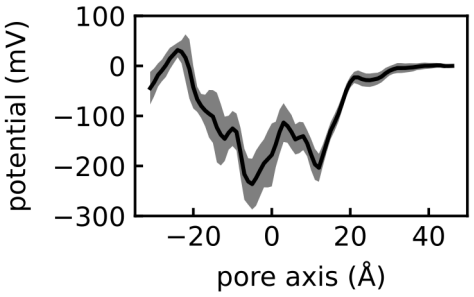

Figure 7.5: Average electrostatic-potential profile along the TMEM16K pore based on the 1 μs trajectory. The profile was calculated based on the electrostatic-potential map produced with *g_elpot* and $\beta = 20\ \mathrm{nm}^{-1}$. Shaded area indicates the standard deviation of the potential, as calculated for 10 separate 100 ns blocks.

suggested their importance for ion selectivity of the TMEM16K pore. Two of these residues, E340 and E371, interact with permeating Na^+ ions, as we have shown in Chapter 5. To quantify the effect of these residues on the pore electrostatics, we conducted a series of simulations on E340K and E371K mutants of TMEM16K (Tables A.7 and A.8) and applied *g_elpot* to the resulting trajectories. In accordance with their positions, the charge-reversing mutations alter the potential either in the intracellular or extracellular part of the pore, leaving the other part unchanged (Figure 7.6a). The E371K mutation locally increases the potential by ∼300 mV, and thereby changes the polarity of the potential in the intracellular part of the pore. As a result, the region that has the lowest potential in the wild type protein acquires the highest potential within the mutant pore (Figure 7.6a). The effect is less prominent in case of the E340K mutation, which increases the potential by ∼200 mV and does not lead to a reverse in the sign of the potential. In agreement with the change in the electrostatic potential, the mutants demonstrated a clear shift in their ion selectivity towards more Cl^- selective currents (Table 7.1). We note that the effect of the mutations on the pore electrostatics would be less prominent in case the glutamates were in the protonated state. How-

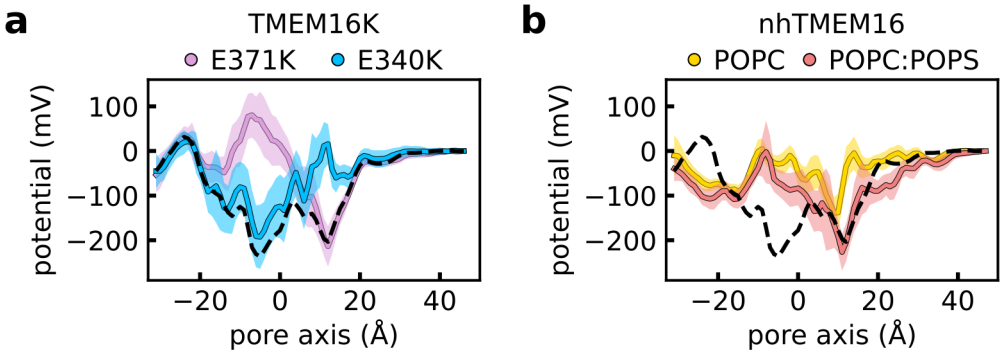

Figure 7.6: **a** Electrostatic-potential profiles along the pores of the E371K and E340K mutants of TMEM16K in POPC membrane. **b** Electrostatic-potential profiles along the nhTMEM16 pore in POPC and POPC:POPS membranes. **a**, **b** Each profile was calculated based on a 1 μs trajectory, with shaded areas representing standard error of mean, as calculated for 100 ns blocks. Average electrostatic-potential along the TMEM16K pore in POPC membrane is shown by dashed line.

mutant	P_{Na}/P_{Cl} (global)	P_{Na}/P_{Cl}(V+)	P_{Na}/P_{Cl} (V-)
E340K	0.25	-	0.25
E371K	0.56	0.2	0.61

Table 7.1: Ion selectivity of the TMEM16K mutants in POPC membranes. P_{Na}/P_{Cl} was calculated globally, and separately for protomers at positive (V+) and negative (V-) voltages.

ever, both E340 and E371 remain well hydrated during the MD trajectories, implying that the pK_a values stay close to the standard ones and therefore justifying usage of their deprotonated state in the simulations.

nhTMEM16

Aiming to quantify the effect of anionic lipids on the electrostatic potential within the nhTMEM16 pore, we applied *g_elpot* to the trajectories of nhTMEM16 in either POPC or POPC:POPS membrane. The profiles calculated from the resulting electrostatic-potential maps are shown in Figure 7.6b. Addition of anionic POPS lipids to the POPC membrane reduced the potential within the nhTMEM16 cavity, making it negative along the whole pore region. "The most notable difference between the POPC and POPC:POPS profiles is seen near the extracellular entrance of the pore (at 10–20 Å along the pore axis), where the potential is about 100 mV more negative in the anionic membrane. Interestingly, the potential in this region of nhTMEM16 in the POPC:POPS mixture is extremely similar to that of TMEM16K (Figure 7.6b)"[B] Thus we conclude that, similar to charged residues, charged lipids can have a prominent impact on the electrostatics in the proteolipidic pore of TMEM16 lipid scramblases.

7.4 Conclusions

In this chapter we described a method for calculating the electrostatic potential in biomolecular systems based on MD trajectories. The method was implemented in the g_elpot tool, which was applied to our MD simulations of TMEM16K and nhTMEM16. "Using g_elpot on μs-long MD trajectories overcame the limitations of static experimental structures related to the complex and dynamic nature of the proteolipidic pores of nhTMEM16 and TMEM16K. This enabled us to identify the regions responsible for the diverse ion selectivities of these lipid scramblases."[B] "In summary, we have demonstrated that g_elpot is well suited to analyze electrostatics in biomolecular cavities with complex structures and identified the relationship between electrostatics and ion selectivity in TMEM16 lipid scramblases."[B]

Ignoramus et ignorabimus.
—Emil Du Bois-Reymond

Chapter 8

Conclusions and perspectives

Ion conduction mediated by TMEM16 lipid scramblases has various physiological implications. Their full understanding is obscured by the lack of a detailed ion-conduction model, which could explain controversial functional properties of TMEM16 lipid scramblases as ion channels. In this thesis, we employed extensive atomistic MD simulations to bridge structural and functional data, thereby providing an atomic-level description of the ion conduction facilitated by lipid scramblases of the TMEM16 family. We demonstrated that in the main ion-conductive state TMEM16 lipid scramblases conduct ions through the proteolipidic pore, which is formed by the subunit cavity and lipid headgroups. The isoform-specific network of interactions provides a scaffold for the headgroup arrangement that additionally depends on polarity of the applied voltage. We identified the localization sites of permeating ions, which are stabilized there by both the cavity residues and lipid headgroups. These lipid headgroups shape energetics of the permeating ions and can control permeability of the scramblase pore by blocking its entrances. Pronounced in nhTMEM16 but not in TMEM16K, this effect suggests existence of the isoform-dependent coupling between lipid scrambling and ion conduction. Circumventing limitations associated with experimental investigation of TMEM16K, we demonstrated that it forms a cation-selective channel, in contrast to the nonselective nhTMEM16. Moreover, we revealed structural basis for the difference in ion selectivity between the two homologs. Finally, we found that membrane lipid composition can have a drastic effect on the observed ion selectivity of TMEM16 lipid scramblases. In particular, addition of anionic lipids rendered a slightly Cl^- selective pore of nhTMEM16 Na^+ selective. We showed that addition of mono- and divalent cations reverses the selectivity change by screening negative charge created by anionic lipids at the pore entrances. By this, we provided the mechanistic explanation for the high variability of ion selectivity observed in experimental studies on TMEM16 lipid scramblases.

Aiming to quantification of electrostatics within the proteolipidic pore, we developed a water-based scheme for calculating electrostatic potential around biomolecules and

implemented this scheme in the g_elpot tool. Applying g_elpot to our simulations, we identified the regions of the nhTMEM16 pore which are mostly affected by anionic lipids. Additionally, we quantified the effect of mutations on the electrostatics of the TMEM16K pore. Although in this thesis we describe applications of g_elpot only to TMEM16 proteins, the tool can be used to study electrostatics of other macromolecules, including, but not limited to, transporters, globular proteins, and DNA [B]. We believe that g_elpot can become a tool of choice for the initial biophysical characterization of newly resolved biomolecular structures in the experimental studies that are now often complemented with MD simulations. All in all, we anticipate that the insights obtained with g_elpot will result in the deeper understanding of the roles of electrostatics in physiological functions of biomolecules.

Lipid species of cellular membranes are well known to play import roles in functioning of a wide range of membrane proteins [109, 110]. However, most of the reported effects that lipids have on ion channels and their ion conduction have been limited to indirect influence via allosteric modulation or via changes in mechanical properties of the membranes [109, 110]. In contrast, here we report the direct modulatory effects of lipids on ion permeation and ion selectivity in TMEM16 lipid scramblases. Intriguingly, the structures of TMEM16 Cl^- channels are compatible with partial presence of lipid headgroups at the vestibules of their pores. Therefore, we propose that lipids might also have direct impact on ion conduction mediated by the bona fide channels of the TMEM16 family. Moreover, close positioning of the Ca^{2+}-binding site to the intracellular vestibule of the subunit cavity suggests that lipids may have direct impact on the Ca^{2+} binding, thus opening another perspective on the mechanism of Ca^{2+} activation of TMEM16 channels and lipid scramblases. Finally, we note that the structural implication of lipids in the ion permeation pathway is not unique to the TMEM16 family. In particular, lipids have been recently shown to line the pore entrances and thereby to guide ion permeation in an ionotropic receptor of the P2X family [111, 112]. Given the ever growing number of structurally characterized membrane proteins, more examples of ion channels that integrate lipids into their pores can be foreseen. We expect that lipids will directly modulate functional properties of such ion channels and we believe that our findings will provide a general foundation for the mechanistic understanding of their functions.

Appendix A

Summary of simulated systems

	no voltage		CompEL				
system	simulation time (ns)	[NaCl] (mM)	replica	[NaCl] (mM)	dQ	V (mV)	simulation time (ns)
s1	2000	250	1	250	14	304 ± 34	1000
			2	250	20	397 ± 29	500
			3	250	28	533 ± 38	1000
			4	250	30	524 ± 36	400
			5	250	22	509 ± 26	500
			6	250	22	478 ± 32	500
s2	1000	250	1	250	24	471 ± 29	500
			2	250	26	488 ± 37	500
s3	1000	250	1	250	16	348 ± 28	500
			2	250	24	460 ± 38	500
s4	1000	250	1	250	20	453 ± 33	500

Table A.1: Summary of simulations of nhTMEM16 in the fully open conformation in POPC membrane. Each system with no voltage gave rise to several CompEL replicas. Values for the charge imbalance (dQ) and resulting transmembrane voltage (V) are indicated.

	no voltage		CompEL				
system	simulation time (ns)	[NaCl] (mM)	replica	[NaCl] (mM)	dQ	V (mV)	simulation time (ns)
s1	1000	250	1	250	14	292 ± 28	500
			2	250	24	502 ± 42	500
			3	250	28	659 ± 36	500
			4	1000	24	559 ± 41	500
			5	1000	28	539 ± 51	500
s2	1000	250	1	250	20	427 ± 32	500
			2	250	22	442 ± 31	500
s3	1000	250	1	250	20	480 ± 32	500
s4	1000	1000	1	1000	22	484 ± 44	500
			2	1000	24	550 ± 25	500

Table A.2: Summary of simulations of nhTMEM16 in the fully open conformation in POPC:POPS membrane. Each system with no voltage gave rise to several CompEL replicas. Values for the charge imbalance (dQ) and resulting transmembrane voltage (V) are indicated.

	no voltage		CompEL				
system	simulation time (ns)	[NaCl] (mM)	replica	[NaCl] (mM)	dQ	V (mV)	simulation time (ns)
s1	1500	250	1	250	22	480 ± 28	500
			2	250	28	568 ± 48	500
s2	1000	250	1	250	20	422 ± 45	500
			2	250	26	596 ± 37	500
s3	1000	250	1	250	24	543 ± 30	500
			2	250	26	589 ± 32	500

Table A.3: Summary of simulations of nhTMEM16 in the fully open conformation in POPE:POPG membrane. Each system with no voltage gave rise to several CompEL replicas. Values for the charge imbalance (dQ) and resulting transmembrane voltage (V) are indicated.

	no voltage		CompEL				
system	simulation time (ns)	[NaCl] (mM)	replica	[NaCl] (mM)	dQ	V (mV)	simulation time (ns)
s1	1000	250	1	250	16	481 ± 30	500
			2	250	18	549 ± 27	500
			3	250	20	518 ± 36	500
			4	250	24	660 ± 35	500
			5	250	28	727 ± 68	500
s2	1000	250	1	250	16	511 ± 24	500
			2	250	18	515 ± 27	500
			3	250	20	585 ± 34	500
			4	250	22	646 ± 27	500
			5	250	24	701 ± 35	500

Table A.4: Summary of simulations of nhTMEM16 in the intermediate conformation in POPC membrane. Each system with no voltage gave rise to several CompEL replicas. Values for the charge imbalance (dQ) and resulting transmembrane voltage (V) are indicated.

	no voltage		CompEL				
system	simulation time (ns)	[NaCl] (mM)	replica	[NaCl] (mM)	dQ	V (mV)	simulation time (ns)
s1	100	200	1	200	22	551 ± 45	500
			2	200	22	629 ± 36	500
			3	200	22	605 ± 44	500
			4	200	22	654 ± 34	500
			5	200	22	654 ± 35	500
			6	200	22	651 ± 36	500

Table A.5: Summary of simulations of nhTMEM16 in the fully open conformation in POPC:POPS membrane at 1 mM $CaCl_2$. One system with no voltage gave rise to several CompEL replicas. Values for the charge imbalance (dQ) and resulting transmembrane voltage (V) are indicated.

	no voltage		CompEL				
system	simulation time (ns)	[NaCl] (mM)	replica	[NaCl] (mM)	dQ	V (mV)	simulation time (ns)
s1	1000	250	1	250	10	250 ± 29	1000
			2	250	14	362 ± 38	500
			3	250	18	470 ± 34	500
			4	250	24	607 ± 41	500
s2	1000	250	1	250	16	426 ± 26	500
			2	250	20	490 ± 34	500
			3	250	24	588 ± 44	500

Table A.6: Summary of simulations of TMEM16K in POPC membrane. Each system with no voltage gave rise to several CompEL replicas. Values for the charge imbalance (dQ) and resulting transmembrane voltage (V) are indicated.

	no voltage		CompEL				
system	simulation time (ns)	[NaCl] (mM)	replica	[NaCl] (mM)	dQ	V (mV)	simulation time (ns)
s1	1000	250	1	250	20	564 ± 28	500
s2	1000	250	1	250	20	530 ± 26	500

Table A.7: Summary of simulations of the E340K mutant of TMEM16K in POPC membrane. Each system with no voltage gave rise to one CompEL replica. Values for the charge imbalance (dQ) and resulting transmembrane voltage (V) are indicated.

	no voltage		CompEL				
system	simulation time (ns)	[NaCl] (mM)	replica	[NaCl] (mM)	dQ	V (mV)	simulation time (ns)
s1	1000	250	1	250	20	471 ± 54	500
s2	1000	250	1	250	20	458 ± 34	500

Table A.8: Summary of simulations of the E371K mutant of TMEM16K in POPC membrane. Each system with no voltage gave rise to one CompEL replica. Values for the charge imbalance (dQ) and resulting transmembrane voltage (V) are indicated.

Bibliography

[1] Caputo, A. et al. TMEM16A, a membrane protein associated with calcium-dependent chloride channel activity. *Science* **2008**, *322*, 590–594.

[2] Schroeder, B. C. et al. Expression cloning of TMEM16A as a calcium-activated chloride channel subunit. *Cell* **2008**, *134*, 1019–1029.

[3] Yang, Y. D. et al. TMEM16A confers receptor-activated calcium-dependent chloride conductance. *Nature* **2008**, *455*, 1210–1215.

[4] Schreiber, R. et al. Expression and function of epithelial anoctamins. *J. Biol. Chem.* **2010**, *285*, 7838–7845.

[5] Liu, B. et al. The acute nociceptive signals induced by bradykinin in rat sensory neurons are mediated by inhibition of M-type K^+ channels and activation of Ca^{2+}-activated Cl- channels. *J. Clin. Investig.* **2010**, *120*, 1240–1252.

[6] Cho, H. et al. The calcium-activated chloride channel anoctamin 1 acts as a heat sensor in nociceptive neurons. *Nat. Neurosci.* **2012**, *15*, 1015–1021.

[7] Huang, W. C. et al. Calcium-activated chloride channels (CaCCs) regulate action potential and synaptic response in hippocampal neurons. *Neuron* **2012**, *74*, 179–192.

[8] Stephan, A. B. et al. ANO2 is the cilial calcium-activated chloride channel that may mediate olfactory amplification. *Proc. Natl. Acad. Sci. U.S.A.* **2009**, *106*, 11776–11781.

[9] Tien, J. et al. A comprehensive search for calcium binding sites critical for TMEM16A calcium-activated chloride channel activity. *eLife* **2014**, *3*.

[10] Pifferi, S., Dibattista, M., and Menini, A. TMEM16B induces chloride currents activated by calcium in mammalian cells. *Pflugers Arch. - Eur. J. Physiol.* **2009**, *458*, 1023–1038.

[11] Xiao, Q. et al. Voltage- and calcium-dependent gating of TMEM16A/Ano1 chloride channels are physically coupled by the first intracellular loop. *Proc. Natl. Acad. Sci. U.S.A.* **2011**, *108*, 8891–8896.

[12] Suzuki, J. et al. Calcium-dependent phospholipid scrambling by TMEM16F. *Nature* **2010**, *468*, 834–838.

[13] Yang, H. et al. TMEM16F forms a Ca^{2+}-activated cation channel required for lipid scrambling in platelets during blood coagulation. *Cell* **2012**, *151*, 111–122.

[14] Brooks, M. B. et al. A TMEM16F point mutation causes an absence of canine platelet TMEM16F and ineffective activation and death-induced phospholipid scrambling. *J. Thromb. Haemost.* **2015**, *13*, 2240–2252.

[15] Ehlen, H. W. A. et al. Inactivation of Anoctamin-6/TMEM16F, a regulator of phosphatidylserine scrambling in osteoblasts, leads to decreased mineral deposition in skeletal tissues. *J. Bone Miner. Res.* **2013**, *28*, 246–259.

[16] Connolly, A. et al. TMEM16F mediates bystander TCR-CD3 membrane dissociation at the immunological synapse and potentiates T cell activation. *Sci. Signal.* **2021**, *14*.

[17] Zhang, Y. et al. TMEM16F phospholipid scramblase mediates trophoblast fusion and placental development. *Sci. Adv.* **2020**, *6*, eaba0310.

[18] Whitlock, J. M. and Hartzell, H. C. A pore idea: The ion conduction pathway of TMEM16/ANO proteins is composed partly of lipid. *Pflugers Arch. - Eur. J. Physiol.* **2016**, *468*, 455–473.

[19] Lorent, J. H. et al. Plasma membranes are asymmetric in lipid unsaturation, packing and protein shape. *Nat. Chem. Biol.* **2020**, *16*, 644–652.

[20] Suzuki, J. et al. Calcium-dependent phospholipid scramblase activity of TMEM16 protein family members. *J. Biol. Chem.* **2013**, *288*, 13305–13316.

[21] Bushell, S. R. et al. The structural basis of lipid scrambling and inactivation in the endoplasmic reticulum scramblase TMEM16K. *Nat. Commun.* **2019**, *10*.1, 1–16.

[22] Petkovic, M. et al. TMEM16K is an interorganelle regulator of endosomal sorting. *Nat. Commun.* **2020**, *11*, 3298.

[23] Malvezzi, M. et al. Ca^{2+}-dependent phospholipid scrambling by a reconstituted TMEM16 ion channel. *Nat. Commun.* **2013**, *4*, 2367.

[24] Brunner, J. D. et al. X-ray structure of a calcium-activated TMEM16 lipid scramblase. *Nature* **2014**, *516*.7530, 207–212.

[25] Pedemonte, N. and Galietta, L. J. V. Structure and function of TMEM16 proteins (anoctamins). *Physiol. Rev.* **2014**, *94*, 419–459.

[26] Martins, J. R. et al. Anoctamin 6 is an essential component of the outwardly rectifying chloride channel. *Proc. Natl. Acad. Sci. U.S.A.* **2011**, *108*, 18168–18172.

[27] Szteyn, K. et al. Expression and functional significance of the Ca^{2+}-activated Cl^- channel ANO6 in dendritic cells. *Cell. Physiol. Biochem.* **2012**, *30*, 1319–1332.

[28] Lin, H. et al. TMEM16F/ANO6, a Ca^{2+}-activated anion channel, is negatively regulated by the actin cytoskeleton and intracellular MgATP. *Biochem. Biophys. Res. Commun.* **2018**, *503*, 2348–2354.

[29] Hammer, C. et al. A coding variant of ANO10, affecting volume regulation of macrophages, is associated with Borrelia seropositivity. *Mol. Med.* **2015**, *21*, 26–37.

[30] Lee, B.-C., Menon, A. K., and Accardi, A. The nhTMEM16 scramblase is also a nonselective ion channel. *Biophys. J.* **2016**, *111*.9, 1919–1924.

[31] Juul, C. A. et al. Anoctamin 6 differs from VRAC and VSOAC but is involved in apoptosis and supports volume regulation in the presence of Ca^{2+}. *Pflugers Arch. - Eur. J. Physiol.* **2014**, *466*, 1899–1910.

[32] Ousingsawat, J. et al. Anoctamin 6 mediates effects essential for innate immunity downstream of P2X7 receptors in macrophages. *Nat. Commun.* **2015**, *6*, 6245.

[33] Cabrita, I. et al. Differential effects of anoctamins on intracellular calcium signals. *The FASEB Journal* **2017**, *31*, 2123–2134.

[34] Grubb, S. et al. TMEM16F (Anoctamin 6), an anion channel of delayed Ca^{2+} activation. *J. Gen. Physiol.* **2013**, *141*.5, 585–600.

[35] Kunzelmann, K. et al. Molecular functions of anoctamin 6 (TMEM16F): a chloride channel, cation channel, or phospholipid scramblase? *Pflugers Arch. - Eur. J. Physiol.* **2014**, *466*, 407–414.

[36] Yu, K. et al. Identification of a lipid scrambling domain in ANO6/TMEM16F. *eLife* **2015**, *4*, e06901.

[37] Taylor, K. A. and Mahaut-Smith, M. P. A major interspecies difference in the ionic selectivity of megakaryocyte Ca^{2+}-activated channels sensitive to the TMEM16F inhibitor CaCCinh-A01. *Platelets* **2019**, *30*, 962–966.

[38] Shimizu, T. et al. TMEM16F is a component of a Ca^{2+}-activated Cl^- channel but not a volume-sensitive outwardly rectifying Cl^- channel. *Am. J. Physiol. Cell Physiol.* **2013**, *304*.8, C748–C759.

[39] Ye, W. et al. Phosphatidylinositol-(4, 5)-bisphosphate regulates calcium gating of small-conductance cation channel TMEM16F. *Proc. Natl. Acad. Sci. U.S.A.* **2018**, *115*, E1667–E1674.

[40] Alvadia, C. et al. Cryo-EM structures and functional characterization of the murine lipid scramblase TMEM16F. *eLife* **2019**, *8*.

[41] Ye, W. et al. Dynamic change of electrostatic field in TMEM16F permeation pathway shifts its ion selectivity. *eLife* **2019**, *8*.

[42] Nguyen, D. M., Kwon, H. C., and Chen, T.-Y. Divalent Cation Modulation of Ion Permeation in TMEM16 Proteins. *Int. J. Mol. Sci.* **2021**, *22*.

[43] Jiang, T. et al. Lipids and ions traverse the membrane by the same physical pathway in the nhTMEM16 scramblase. *Elife* **2017**, *6*, e28671.

[44] Sheridan, J. T. et al. Characterization of the oligomeric structure of the Ca^{2+}-activated Cl^- channel Ano1/TMEM16A. *J. Biol. Chem.* **2011**, *286*, 1381–1388.

[45] Fallah, G. et al. TMEM16A(a)/anoctamin-1 shares a homodimeric architecture with CLC chloride channels. *Mol. Cell. Proteomics* **2011**, *10*, M110.004697.

[46] Yu, K. et al. Explaining calcium-dependent gating of anoctamin-1 chloride channels requires a revised topology. *Circ. Res.* **2012**, *110*, 990–999.

[47] Arreola, J., Melvin, J. E., and Begenisich, T. Activation of calcium-dependent chloride channels in rat parotid acinar cells. *J. Gen. Physiol.* **1996**, *108*, 35–47.

[48] Bethel, N. P. and Grabe, M. Atomistic insight into lipid translocation by a TMEM16 scramblase. *Proc. Natl. Acad. Sci. U.S.A.* **2016**, *113*.49, 14049–14054.

[49] Khelashvili, G. et al. Dynamic modulation of the lipid translocation groove generates a conductive ion channel in Ca^{2+}-bound nhTMEM16. *Nat. Commun.* **2019**, *10*.1, 1–15.

[50] Lee, B.-C. et al. Gating mechanism of the extracellular entry to the lipid pathway in a TMEM16 scramblase. *Nat. Commun.* **2018**, *9*.1.

[51] Le, T. et al. An inner activation gate controls TMEM16F phospholipid scrambling. *Nat. Commun.* **2019**, *10*.1, 1846.

[52] Pomorski, T and Menon, A. K. Lipid flippases and their biological functions. *Cell. Mol. Life Sci.* **2006**, *63*, 2908–2921.

[53] Paulino, C. et al. Activation mechanism of the calcium-activated chloride channel TMEM16A revealed by cryo-EM. *Nature* **2017**, *552*, 421–425.

[54] Dang, S. et al. Cryo-EM structures of the TMEM16A calcium-activated chloride channel. *Nature* **2017**, *552*, 426–429.

[55] Feng, S. et al. Cryo-EM studies of TMEM16F Calcium-Activated ion channel suggest features important for lipid scrambling. *Cell reports* **2019**, *28*.2, 567–579.

[56] Kalienkova, V. et al. Stepwise activation mechanism of the scramblase nhTMEM16 revealed by cryo-EM. *eLife* **2019**, *8*.

[57] Falzone, M. E. et al. Structural basis of Ca^{2+}-dependent activation and lipid transport by a TMEM16 scramblase. *eLife* **2019**, *8*.

[58] Le, S. C. and Yang, H. An Additional Ca^{2+} Binding Site Allosterically Controls TMEM16A Activation. *Cell Rep.* **2020**, *33*, 108570.

[59] De Jesús-Pérez, J. J. et al. Phosphatidylinositol 4,5-bisphosphate, cholesterol, and fatty acids modulate the calcium-activated chloride channel TMEM16A (ANO1). *Biochim. Biophys. Acta Mol. Cell. Biol. Lipids* **2018**, *1863*, 299–312.

[60] Levitt, M. and Warshel, A. Computer simulation of protein folding. *Nature* **1975**, *253*, 694–698.

[61] Warshel, A. Bicycle-pedal model for the first step in the vision process. *Nature* **1976**, *260*, 679–683.

[62] McCammon, J. A., Gelin, B. R., and Karplus, M. Dynamics of folded proteins. *Nature* **1977**, *267*, 585–590.

[63] Hollingsworth, S. A. and Dror, R. O. Molecular dynamics simulation for all. *Neuron* **2018**, *99*, 1129–1143.

[64] Frenkel, D. and Smit, B. Understanding molecular simulation**. 2002**.

[65] Berendsen, H. J. C. et al. Molecular dynamics with coupling to an external bath. *J. Chem. Phys.* **1984**, *81*, 3684–3690.

[66] Bussi, G., Donadio, D., and Parrinello, M. Canonical sampling through velocity rescaling. *J. Chem. Phys.* **2007**, *126*, 014101.

[67] Parrinello, M. and Rahman, A. Polymorphic transitions in single crystals: A new molecular dynamics method. *J. Appl. Phys.* **1981**, *52*, 7182–7190.

[68] Nosé, S. and Klein, M. Constant pressure molecular dynamics for molecular systems. *Mol. Phys.* **1983**, *50*.5, 1055–1076.

[69] Huang, J. et al. CHARMM36m: an improved force field for folded and intrinsically disordered proteins. *Nat. Methods* **2017**, *14*, 71–73.

[70] Antila, H. et al. Headgroup structure and cation binding in phosphatidylserine lipid bilayers. *J. Phys. Chem. B* **2019**, *123*, 9066–9079.

[71] Wang, J. et al. Development and testing of a general amber force field. *J. Comput. Chem.* **2004**, *25*, 1157–1174.

[72] Jorgensen, W. L., Maxwell, D. S., and Tirado-Rives, J. Development and testing of the OPLS all-atom force field on conformational energetics and properties of organic liquids. *J. Am. Chem. Soc.* **1996**, *118*, 11225–11236.

[73] Mackerell, A. D., Feig, M., and Brooks, C. L. Extending the treatment of backbone energetics in protein force fields: limitations of gas-phase quantum mechanics in reproducing protein conformational distributions in molecular dynamics simulations. *J. Comput. Chem.* **2004**, *25*, 1400–1415.

[74] Vanommeslaeghe, K. and MacKerell, A. D. CHARMM additive and polarizable force fields for biophysics and computer-aided drug design. *Biochim. Biophys. Acta* **2015**, *1850*, 861–871.

[75] Ryckaert, J.-P., Ciccotti, G., and Berendsen, H. J. Numerical integration of the cartesian equations of motion of a system with constraints: molecular dynamics of n-alkanes. *J. Comput. Phys.* **1977**, *23*.3, 327–341.

[76] Hess, B. et al. LINCS: a linear constraint solver for molecular simulations. *J. Comput. Chem.* **1997**, *18*.12, 1463–1472.

[77] Essmann, U. et al. A smooth particle mesh Ewald method. *J. Chem. Phys.* **1995**, *103*, 8577–8593.

[78] Jing, Z. et al. Polarizable force fields for biomolecular simulations: Recent advances and applications. *Annu. Rev. Biophys.* **2019**, *48*, 371–394.

[79] Marques, M. A., Purdy, M. D., and Yeager, M. CryoEM maps are full of potential. *Curr. Opin. Struct. Biol.* **2019**, *58*, 214–223.

[80] Kutzner, C. et al. Computational electrophysiology: the molecular dynamics of ion channel permeation and selectivity in atomistic detail. *Biophys. J.* **2011**, *101*, 809–817.

[81] Šali, A. and Blundell, T. L. Comparative protein modelling by satisfaction of spatial restraints. *J. Mol. Biol.* **1993**, *234*.3, 779–815.

[82] Abraham, M. J. et al. GROMACS: High performance molecular simulations through multi-level parallelism from laptops to supercomputers. *SoftwareX* **2015**, *1-2*, 19–25.

[83] Klauda, J. B. et al. Update of the CHARMM all-atom additive force field for lipids: validation on six lipid types. *J. Phys. Chem. B* **2010**, *114*, 7830–7843.

[84] Wolf, M. G. et al. g_membed: Efficient insertion of a membrane protein into an equilibrated lipid bilayer with minimal perturbation. *J. Comput. Chem.* **2010**, *31*, 2169–2174.

[85] Lomize, M. A. et al. OPM database and PPM web server: resources for positioning of proteins in membranes. *Nucleic Acids Res.* **2012**, *40*, D370–D376.

[86] Michaud-Agrawal, N. et al. MDAnalysis: a toolkit for the analysis of molecular dynamics simulations. *J. Comput. Chem.* **2011**, *32*, 2319–2327.

[87] Schreiber, R., Ousingsawat, J., and Kunzelmann, K. Targeting of intracellular TMEM16 proteins to the plasma membrane and activation by purinergic signaling. *Int. J. Mol. Sci.* **2020**, *21*.

[88] Waterhouse, A. M. et al. Jalview Version 2–a multiple sequence alignment editor and analysis workbench. *Bioinformatics* **2009**, *25*, 1189–1191.

[89] Thompson, J. D., Higgins, D. G., and Gibson, T. J. CLUSTAL W: improving the sensitivity of progressive multiple sequence alignment through sequence weighting, position-specific gap penalties and weight matrix choice. *Nucleic Acids Res.* **1994**, *22*, 4673–4680.

[90] Maity, P. et al. Binding of monovalent alkali metal ions with negatively charged phospholipid membranes. *Biochim. Biophys. Acta* **2016**, *1858*, 706–714.

[91] Melcrová, A. et al. The complex nature of calcium cation interactions with phospholipid bilayers. *Sci. Rep.* **2016**, *6*.

[92] Honig, B. and Nicholls, A. Classical electrostatics in biology and chemistry. *Science* **1995**, *268*, 1144–1149.

[93] Li, C. et al. DelPhi suite: New developments and review of functionalities. *J. Comput. Chem.* **2019**, *40*, 2502–2508.

[94] Baker, N. A. et al. Electrostatics of nanosystems: application to microtubules and the ribosome. *Proc. Natl. Acad. Sci. U.S.A.* **2001**, *98*, 10037–10041.

[95] Callenberg, K. M. et al. APBSmem: a graphical interface for electrostatic calculations at the membrane. *PLoS One* **2010**, *5*, e12722.

[96] Dong, F., Olsen, B., and Baker, N. A. Computational methods for biomolecular electrostatics. *Methods Cell. Biol.* **2008**, *84*, 843–870.

[97] Wang, L. Measurements and implications of the membrane dipole potential. *Annu. Rev. Biochem.* **2012**, *81*, 615–635.

[98] Warshel, A. et al. Modeling electrostatic effects in proteins. *Biochim. Biophys. Acta* **2006**, *1764*, 1647–1676.

[99] Cisneros, G. A. et al. Classical electrostatics for biomolecular simulations. *Chem. Rev.* **2014**, *114*, 779–814.

[100] Kutzner, C. et al. Insights into the function of ion channels by computational electrophysiology simulations. *Biochim. Biophys. Acta Biomembr.* **2016**, *1858.7*, 1741–1752.

[101] Lin, Y.-L. et al. An overview of electrostatic free energy computations for solutions and proteins. *J. Chem. Theory Comput.* **2014**, *10*, 2690–2709.

[102] Darden, T., York, D., and Pedersen, L. Particle mesh Ewald: An N·log(N) method for Ewald sums in large systems. *J. Chem. Phys.* **1993**, *98*, 10089–10092.

[103] Aksimentiev, A. and Schulten, K. Imaging alpha-hemolysin with molecular dynamics: ionic conductance, osmotic permeability, and the electrostatic potential map. *Biophys. J.* **2005**, *88*, 3745–3761.

[104] Humphrey, W., Dalke, A., and Schulten, K. VMD: visual molecular dynamics. *J. Mol. Graphics* **1996**, *14*, 33–38.

[105] Enkavi, G. and Tajkhorshid, E. Simulation of spontaneous substrate binding revealing the binding pathway and mechanism and initial conformational response of GlpT. *Biochemistry* **2010**, *49*, 1105–1114.

[106] Arcario, M. J. and Tajkhorshid, E. Membrane-induced structural rearrangement and identification of a novel membrane anchor in talin F2F3. *Biophys. J.* **2014**, *107*, 2059–2069.

[107] Frigo, M. and Johnson, S. G. The design and implementation of FFTW3. *Proc. IEEE* **2005**, *93*, 216–231.

[108] Briones, R. et al. Gromaρs: A GROMACS-based toolset to analyse density maps derived from molecular dynamics simulations. *Biophys. J.* **2019**, *116*.3, 142a–143a.

[109] Muller, M. P. et al. Characterization of lipid-protein interactions and lipid-mediated modulation of membrane protein function through molecular simulation. *Chem. Rev.* **2019**, *119*, 6086–6161.

[110] Corradi, V. et al. Emerging diversity in lipid-protein interactions. *Chem. Rev.* **2019**, *119*, 5775–5848.

[111] Mansoor, S. E. et al. X-ray structures define human P2X(3) receptor gating cycle and antagonist action. *Nature* **2016**, *538*, 66–71.

[112] Scheurer, M. et al. PyContact: Rapid, customizable, and visual analysis of non-covalent interactions in MD simulations. *Biophys. J.* **2018**, *114*, 577–583.

Acknowledgments

First of all, I would like to thank my supervisor Prof. Jan-Philipp Machtens for giving me the opportunity to work on an exciting scientific topic, and to freely explore various directions in my research. I am grateful to him for his help and support throughout these years. I must also thank him for providing me with the enormous amount of computational resources, without which this project would not have been possible.

I would also like to thank Prof. Paolo Carloni and Prof. Jörg Fitter for their willingness to take over positions of the primary and a co-referee for this dissertation.

I wish to thank all former members of the ICS-4 and current members of the IBI-1 of Forschungszentrum Jülich for making the institute an extremely friendly and supportive place where I had great pleasure to work for more than four years.

Lastly, I can hardly find proper words to fully express my deepest gratitude to Diana, Claudia, and Yulia for their support at the main steps of this long trip.